U. PORTO

FEUP FACULDADE DE ENGENHARIA
UNIVERSIDADE DO PORTO

Particle Tracking in Microscopy Sequences for Microrheology Studies

Marina Neves Miranda de Castro

Particle Tracking in Microscopy Sequences for Microrheology Studies

Marina Neves Miranda de Castro

Mestrado Integrado em Bioengenharia

June 23, 2019

Resumo

As técnicas de microreologia são correntemente usadas para avaliar as propriedades viscoelásticas de fluidos complexos quando as técnicas convencionais não o conseguem fazer, devido, por exemplo, aos baixos valores de viscosidade e/ou elasticidade das amostras. Em particular, a técnica de microreologia passiva envolve análise do movimento Browniano de partículas marcadoras através de técnicas de rastreamento aplicadas a sequências de imagens de microscopia em vídeo. Atualmente, a maioria dos trabalhos sobre microreologia usa o mesmo tipo de algoritmo de rastreamento de partículas, cuja robustez só é assegurada quando os vídeos de microscopia adquiridos possuem elevado contraste entre as partículas e um fundo uniforme. A introdução de novas técnicas de rastreamento nesta área pode ser vantajosa para que seja possível usar imagens de microscopia com diferentes condições. Para além disso, a criação de um *framework* intuitivo para rastreamento de partículas em estudos de microreologia poderia beneficiar a comunidade científica que os realiza.

Os objetivos desta dissertação são a exploração de técnicas de rastreamento de partículas, procurando, quer a sua máxima automação, quer a sua incorporação, desde a análise de imagens de microscopia à aquisição de resultados de microreologia, numa interface para o utilizador.

Os métodos de rastreamento de partículas foram testados em vídeos usados em estudos de microreologia, mas também numa base de dados sintética, o que permitiu concluir sobre a exatidão de localização ao nível sub-pixel. Foi confirmado que os métodos usados permitiram que as partículas fossem detectadas com grande exatidão, já que, sendo testados nas imagens sintéticas com o maior nível de ruído considerado neste estudo, produziram um desvio máximo entre centróides verdadeiros e detectados de 0.53 píxeis. Já os resultados adquiridos com vídeos usados em estudos de microreologia mostraram grande variabilidade nos valores de precisão e sensibilidade, denotando que há espaço para melhoramentos futuros na capacidade de generalização dos algoritmos propostos. Mesmo assim, a concordância entre os resultados obtidos através dos métodos propostos nesta dissertação, os resultados de estudos de macroreologia para os mesmos fluídos, e estudos de microreologia que utilizaram os mesmos vídeos, validaram a utilidade do conjunto de algoritmos desenvolvido em estudos de microreologia.

Abstract

Microrheology techniques are broadly used for assessing viscoelastic properties of complex fluids which cannot be analyzed by conventional techniques, due to their low viscosity and/or elasticity values. Particularly, passive microrheology involves analysis of the Brownian motion of tracer particles, through tracking techniques that are applied to microscopy image sequences, in video. Currently, most of the microrheology works use the same particle tracking algorithm, whose robustness relies on the acquisition of microscopy videos in which there is high contrast between the particles and an uniform background. Introducing new tracking techniques in this area may be advantageous for working with different imaging conditions, and creating an intuitive framework for particle tracking in microrheology would highly assist the field's researchers.

The main goals of this dissertation are the exploration of particle tracking algorithms, aiming for their automation, and the incorporation of the microrheology pipeline, from microscopy image analysis to acquisition of complex modulus results, in a guided user interface.

The particle tracking methods were tested in a synthetic database, which allowed to conclude about their accuracy at the sub-pixel level, but also on real microrheology videos. It was confirmed that the final pipeline for particle tracking resulted in a great sub-pixel accuracy, as the offset between real and detected centroids gave rise to a maximum mean total error of 0.53 pixels, for the simulated images with the highest noise level. Moreover, the results in real microrheology setups showed highly variable values for precision and sensitivity, which denotes that there is room for improvement on the generalization capacity of the particle tracking algorithms. Nevertheless, the agreement between complex modulus results, obtained through the proposed methods, and results of macrorheology on the same fluids, or published microrheology data, acquired through the same videos, validated the possibility of use of the proposed pipeline on microrheology studies.

Acknowledgements

Contents

List of Figures

Abbreviations

1D	Unidimensional
2D	Bidimensional
3D	Tridimensional
AB	Adaboost Algorithm
AGCWD	Adaptive Gamma Correction with Weighting Distribution
CCD	Charge-Coupled Device
CRB	Cramér-Rao Bound
DLS	Dynamic Light Scattering
DMSO	Dimethylsulfoxide
DNA	Deoxyribonucleic Acid
DWS	Diffusive Wave Spectroscopy
EDTA	Ethylenediaminetetraacetic Acid
FN	False Negatives
FP	False Positives
FPR	False Positive Rate
FPT	Feature Point Tracking
GIP	Gaussian Intensity Profile
HA	Hyaluronic Acid
IDE	Integrated Development Environment
IPF	Independent Particle Filters
kNN	k Nearest Neighbors
LoG	Laplacian of a Gaussian
MAP	Maximum-a-Posteriori
MLE	Maximum Likelihood Estimator
MMSE	Minimum Mean Squared Error
MPF	Mixture of Particle Filters
MSD	Mean Squared Displacement
MTH	Morphological grayscale opening Top-Hat filter
NN	Nearest Neighbor
PAA	Polyacrylamide
PSF	Point Spread Function
SEF	Spot Enhancing Filter
SNR	Signal to Noise Ratio
TP	True Positives
TPR	True Positive Rate
WGN	White and Gaussian Noise
WMP	Wavelet Multiscale Products
XG	Xanthan Gum

Chapter 1

Introduction

In rheology, the deformation and flow properties of matter are studied using a rheometer, a device that applies forces to the medium. However, fluids having low viscosity and/or elasticity values, cannot be analyzed by this conventional technique, being assessed instead by microrheology. Moreover, macrorheology techniques cannot quantify the dynamics of materials at the microscopic level and work with fluids in large volumes.

Microrheology consists in evaluating the behavior of tracer particles in the fluid via microscopy images, laser tweezers or magnetic tweezers. It can be passive, when the tracer particles move due to inherent thermal energy, or active, if external forces are applied to induce the flow of the tracers. In this work, we consider only the case of passive video particle-tracking microrheology, which involves analyzing the Brownian motion of the tracer particles, through tracking techniques that are applied to microscopy image sequences.

Microrheology through video particle tracking is an interesting technique for quantifying the viscoelastic properties of materials such as polymers, gels or biomaterials inside the linear viscoelastic regime. This behavior is commonly quantified in terms of viscoelastic moduli (G' and G").

Researchers that use microrheology in their studies have been following particle tracking methods that are rarely updated, which is the reason why even the most recent studies (Wehrman et al. (2016), Zia (2017), Garting and Stradner (2018)) still rely on Crocker and Grier's works from 1996 and 2000 (Crocker et al. (2000), Crocker and Grier (1996)) to process microscopy videos for particle tracking. However, introducing new methods for particle tracking (namely detection and linking methods, or even combined approaches), or improving the existing ones, means having to adapt techniques that are tailored to be used in other problems, such as particle tracking in fluorescence microscopy imaging videos or event tracking in scenarios that are distant from biological applications.

To proceed with the development of a new framework and user interface for microrheology studies, one has to take into account that the tracers introduced in the fluids to be studied have Brownian motion. This type of motion is characterized by fast, small and random fluctuations, which have to be carefully analyzed, such that the quantities that are acquired for deriving the

material's viscoelastic properties are not biased. One also needs to consider that the tracers embedded in the fluid are analyzed through their movement in the 2D plane. If these go out of focus during the video acquisition, it may mean that there has been three-dimensional movement, and the motion cannot be characterized without error considering only its two-dimensional component. Therefore, new methods of particle tracking for microrheology studies should detect particle occlusion and reappearance events, such that the tracks formed by these particles can be discarded from the final calculations. Moreover, the tracers are supposed to be inert in the material that is being studied, but this may not happen and these particles may form agglomerates. The grouping of several tracers will alter their motion properties, which gives rise to another necessity: the incorporation of detection of particle agglomerates, to prevent that the trajectories of the particles that form them are included in the calculations of viscoelasticity parameters.

Because even after careful particle detection and linking, some of the formed tracks may be affected by location inaccuracies or natural trajectory aberrations, the user must be in control of what tracks to include in their studies, so they should be able to analyze every track's shape and each particle's appearance, throughout the video, before acquiring final microrheology results. Moreover, to facilitate the particle tracking task, with respect to the user experience, one should prepare the particle tracking pipeline to accept as little inputs as possible, sparing the user from having to fine-tune many parameters.

1.1   Motivation and Objectives

The project HEMOSwimmers, in development by the researchers of the Center for Telecommunications and Multimedia from INESC TEC and CEFT (Transport Phenomena Research Center), aims to analyze the complex fluid flow behavior around microbot prototypes. These microbots are able to circulate inside the main tortuous paths of the human body, like blood vessels. They are designed to actuate on drug delivery, without side-effects, blood-clot removal or high-precision surgeries.

Because this project involves studying the hydrodynamics of fluid flow around microbots, it is necessary to characterize the fluids according to their viscoelastic properties. The project described in this document is developed in the scope of this fluid characterization, through microrheology techniques. Its main objective is to develop a framework that explores the state-of-the-art techniques for particle tracking, for creating a robust solution that can be used, not only in the context of this project, but also for the generality of microrheology studies.

The needs screening, done together with a researcher of the project, with experience in microrheology studies, highlighted the features that should be implemented in a future microrheology framework. First, it should be ready to be used by researchers who do not possess computer programming skills, so it needs to be as intuitive as possible. Moreover, it needs to implement visual inspection tools, for the researchers to control which particle tracks are considered when obtaining final results.

The tracking techniques that will be implemented can be tested on databases, provided by the HEMOSwimmers project researchers. Furthermore, a database of simulated multi-particle images, which form videos of particle movement sequences, with various levels of noise, is created to extend the tests that can be done to validate the proposed methodologies. This is because the microrheology study databases that are available for this work are not annotated and, even if they were, sub-pixel accuracy of particle center detection could not possibly be achieved by the human eye. Knowing the exact location of each particle center is of increased relevance, since Brownian motion is characterized by low magnitude, and needs to be evaluated at the sub-pixel level to be correctly described.

1.2 Main contributions

The development of this dissertation resulted in the following contributions:

- The synthetic database creation methods detailed in Parthasarathy (2012) were extended, both in terms of image properties and particle kinematics. The algorithms developed for this purpose were written in a functional way for future researchers to easily adapt the simulated data to their needs and preferences, through the definition of simple parameters.

- The combination of detection methods, together with data clustering techniques and linking optimization, posed a novel pipeline to address the video particle tracking passive microrheology problem.

- The incorporation of the developed algorithms, together with tools for visual inspection and manual data selection, in a guided user interface, allowed for this dissertation's study to result in a useful utensil for researchers conducting microrheology studies.

- Through the collaboration of the author of this dissertation and her supervisor, Professor Hélder Filipe Oliveira, and co-supervisors, Professor Laura Campo-Deaño and Ricardo Jorge Terroso de Araújo, a publication in the conference IbPRIA 2019[1] was written and selected for poster presentation. This publication is entitled "Towards automatic and robust particle tracking in microrheology studies" and details the pipeline of particle tracking developed in this dissertation.

1.3 Document structure

This document is organized in the following way: in Chapter 2, the background on rheology and the principles of microrheology are explained, together with some applications and a specific case study, hemorheology; Chapter 3 is dedicated to reviewing particle tracking methods in some of their variants, such as splitting the problem into detection and linking or addressing tracking in

---

[1]http://www.ibpria.org/2019

an integrated way; Chapter 4 will focus on the particle tracking algorithms that were explored and on the steps taken towards automatic and robust techniques; Chapter 5 will detail the synthetic database development and the results that could be acquired through it, but also the results obtained with videos of microrheology studies. Chapter 6 presents the attempt of creating a guided user interface for microrheology studies, and, finally, Chapter 7 presents the main conclusions of this work, together with guidelines for further research and improvement of the presented subjects.

Chapter 2

Background

This study aims to create a framework for microrheology studies that is robust and intuitive for the researchers. Therefore, it is fundamental that rheology and microrheology theoretical principles are revised.

A simple review of basic fluid mechanics and rheology is provided in this chapter, starting with why it is important to characterize the viscosity and elasticity of materials, and how it is done. Then, because microrheology comes as a powerful tool for fluid characterization in conditions that are not supported by conventional macrorheology techniques, its essential topics are revised and the hemorheology case study is presented.

2.1 Rheology fundamentals

Rheology is the quantitative study of the manner in which materials deform and flow. It describes the response of materials to force, focusing on isotropic disordered materials. The objects of a rheology study can go from elastic solids to viscous liquids, but also concern the materials with properties in between the two, which are named "soft materials". These can be emulsions, polymers, glassy materials and thermally agitated colloidal structures (with particles ranging from 1 nm to 1 μm) (Sperling (2005)).

The responses of materials to force vary with their constitution and properties: if a material is viscous, the stress-strain relation is different than for an elastic material. While the latter follows Hooke's law of linear elasticity, in which stress is proportional to strain, with Young's Modulus as the proportionality constant, a viscous fluid under shear stress obeys $\sigma = \eta d\varepsilon/dt$, with η, σ and ε denoting viscosity, shear stress and strain, respectively. Viscosity can be defined as the flow resistance caused by internal friction, developed by materials that are put into motion, having their molecules and particles sliding along each other. Larger material components are responsible for higher viscosity values (Mezger (2015)). In reality, all materials deviate from Hooke's law in various ways, for example, exhibiting both viscous-like and elastic characteristics. Viscoelasticity can, then, be defined as a behavior between viscosity and elasticity. The viscous behavior of a

viscoelastic material can be thought of as the component of the deformation that is time-dependent, and its elastic behavior as the instantaneous time-independent response (Sperling (2005)).

Rheometry is the measuring technology used to determine rheological properties. Instruments that measure viscoelastic properties of solids, semi-solids, and fluids are named rheometers, while those which are limited for the measurement of the viscous flow behavior of fluids are viscometers. A rheometer is more versatile and has a wider range of applications than a viscometer (Schramm (2009)).

Figure 2.1 details how solid objects react when subjected to shear stresses. Shear stress is defined as the ratio between force and area ($N/m^2 = Pa$) and strain is the ratio between the deformation of the body in the same direction as shear stress (dL) and the height of the solid body (y). In this case, the proportionality constant between shear stress and strain is the Young's Modulus, G, which relates to the stiffness of the solid. The relation between these variables can be seen in Equation 2.1 (Schramm (2009)).
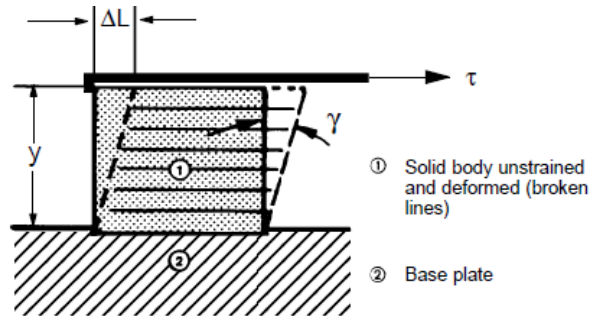
Figure 2.1: Deformation of a solid body under shear stress. Adapted from Schramm (2009).

$$\tau = G \cdot dL/dy = G \cdot tan(\gamma) \approx G \cdot \gamma \tag{2.1}$$

This Young's Modulus for solids is analog to a fluid's viscosity: the resistance against any irreversible positional changes of a fluid's volume elements. This way, the experimental setups for shear-induced flow allow for the measurement of viscosity, in the same way Young's Modulus could be measured in a setup similar to Figure 2.1: using the flow between two plates or the circular flow in the annular gap between two coaxial cylinders, for example.

For measuring the viscosity of liquids, one must know the relation between viscosity, shear stress and shear rate, valid for viscous materials, present in Equation 2.2.

$$\tau = \eta \cdot \dot{\gamma} \tag{2.2}$$

Shear rate, $\dot{\gamma}$, is the speed drop across the gap size, mathematically defined by a differential (dV/dy). Maximum flow speed is found at the upper boundary, and a minimal null value is found at the lower boundary, contacting the stationary plate. Comparing Equations 2.2 and 2.1, we can see a basic difference between solids and liquids: shear stress causes strain in solids, but

in liquids, it causes a rate of strain. This means that solids are elastically deformed, while liquids flow (Schramm (2009)).

Viscosity may depend on six independent parameters: the physical-chemical nature of the substance, the temperature of the substance, the pressure, since it increases intermolecular resistance in fluids, the shear rate (in Non-Newtonian fluids), the duration of continuous shear or of the rest period before being tested, and the electrical field, which applies for electro-viscous fluids (which contain dispersed dielectric particles in electro-conductive liquids) (Schramm (2009)).

Non-Newtonian fluids outnumber ideally viscous fluids by far. These do not show a linear relationship between shear stress and shear rate, which means that their viscosity could be altered by shear stress and rate (Schramm (2009)).

Pseudoplastic liquids show drastic viscosity decrease when the shear rate is highly increased. Examples of this phenomena are the decrease of viscosity in fast pumping of pharmaceutical products through pipe lines or capillaries or in vigorous squeeze of toothpaste tubes. Many substances such as emulsions, suspensions or dispersions belong to this group. The reason for this to happen is that, even though these liquid products seem homogeneous, they are not. Polymer solutions with long entangled molecular chains fall in the same category. At rest, these materials maintain an irregular internal order, being characterized by a great internal resistance against flow (high viscosity), but, as the shear rate increases, planar particles suspended in the liquid will be turned lengthwise in the direction of the flow and chains of molecules will break, stretch and orient themselves parallel to the driving force. This reorientation allows particles to slip past each other easily. The shape of the particles may also change to be more elongated, and aggregates of particles may be broken. For most liquids, this shear-thinning effect is reversible and the liquids regain their original viscosity when shearing is slowed down or terminated (Schramm (2009)).

Shear-thinning of liquids is not uniform over the range of very low to very high rates. In spite of initial effects of shear orientation in low shear rate, the Brownian motion of molecules keeps them from not being randomly moving. This is why pseudoplastic liquids behave similarly to Newtonian ones at low shear rates (below $1 \ s^{-1}$), being their viscosity in these conditions often called "zero shear viscosity" (Mezger (2015)). As shear rate starts to increase, surpassing the randomizing effect of the Brownian motion, the viscosity drops rapidly. In extremely high shear rates, the viscosity approaches, asymptotically, a constant value, since the optimum particle orientation has been reached. This extremely high shear rate range is considered as the second Newtonian range, since increasing shear rate when this level is reached does not affect viscosity. Putting this into numbers, the relevant viscosity changes usually occur only in shear rates between $1 \ s^{-1}$ and $1000.000 \ s^{-1}$ (Schramm (2009)).

The pseudoplastic behavior can be seen in Figure 2.2, in which η_0 is the minimal constant viscosity, in the first Newtonian range, and η_∞ is the maximum asymptotic viscosity, in the second Newtonian range.

On the other hand, liquids may show a dilatant flow behavior, in which viscosity is increased with increasing shear rates. This is found, for example, in highly concentrated suspensions, in
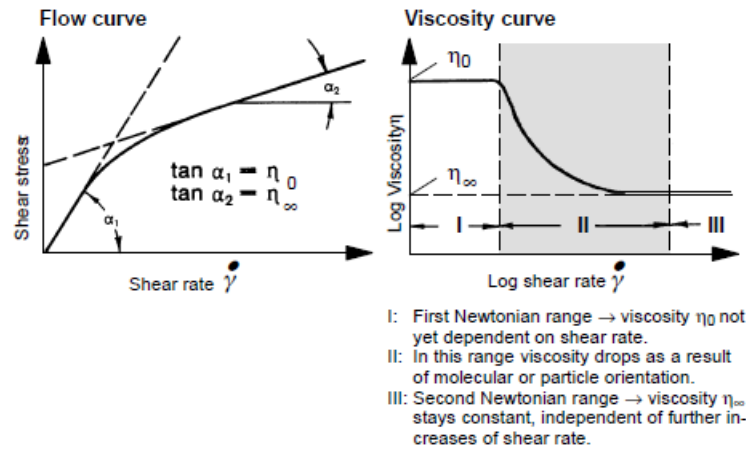
Figure 2.2: The shear rate dependence of pseudoplastic liquids. Adapted from Schramm (2009).

which solid, densely packed, particles such as emulsion-PVC are mixed with liquids such as plasticizers, which are added in just enough quantity to fill the voids between the particles, forming plastisols. At low shear rates, the plasticizer fully lubricates the particle surfaces and allows an easy positional change of particles when forces are applied, making the suspension behave as a liquid. At higher shear rates, particles will wedge others apart causing general volume increase. At this point, the plasticizer is no longer sufficient to fill all the voids between particles, keeping them lubricated, so the plastisol becomes more viscous.

There can also be plastic liquids, which are pseudoplastic liquids that have an additional yield point. This yield point is a shear stress threshold that, when surpassed, makes the network collapse, making volume elements change position irreversibly.

In opposition, some pseudoplastic liquids exhibit a thixotropic property. These gels have network structures with weak hydrogen and ionic bonds. Being thixotropic means that, as the liquid's network is disrupted, the viscosity drops with shear time (but constant shear rate) until it asymptotically reaches the lowest possible value for a given shear rate. This minimum viscosity level describes the sol-status of the liquid, but the structure can be reformed back to the gel form, as long as the substance can rest for an extended period of time. Yoghurts, in this context, are examples of non-thixotropic fluids, since their organic structure can be broken by shear, but not rebuilt with time. On contrary, rheopectic liquids show an anti-thixotropic flow behavior, which means that their viscosity increases with the duration of shear. When these liquids are allowed to rest, they recover a low viscosity level.

Having stated all these possible behaviors of liquids in respect to shear stress and viscosity, we can come to the conclusion that the conditions of rheometry experiments need to be well controlled in terms of the six previously defined parameters. For example, the shear rate or shear rate range must be fixed for all the tested samples, since the substance can show a highly non-Newtonian flow behavior, having its viscosity depending heavily on the shear rate. As for the thixotropic samples, one one may want to test them in sol or gel condition, so the shear history and timing must be kept precisely (Schramm (2009)).

In order to understand time-dependent stress/strain relations that are characteristic of viscoelasticity, one can combine the idea of an ideal solid, expressed in Equation 2.1, which can be modeled as a metal spiral spring, and an ideal Newtonian liquid, expressed in Equation 2.2, which can be modeled as a damper or dashpot (a piston fitting in an cylinder filled with oil). This being said, combinations of springs and dashpots can define viscoelasticity. These combinations lead to a time-dependent response of rheological parameters, which does not exist for ideally elastic solids or viscous Newtonian liquids. There are many models for viscoelastic properties based on springs and dashpots, such as the Maxwell fluid model, in which the spring and the dashpot are placed in series, leading to additive deformations, characteristic of viscoelastic liquids. The Kelvin-Voigt solid model combines a spring and a dashpot in parallel, ensuring that that the forces and strains are equally applied, which represents a viscoelastic solid. The Burger model combines the two preceding ones in series, arriving to a better fit to a general viscoelastic material (Schramm (2009)).

Asides from creep and recovery tests or applying constant strains to viscoelastic materials to obtain their compliance and stress relaxation modulus (Equation 2.1), a very popular test is to subject samples to oscillating stresses or oscillating strains. These are named tests with forced oscillation or dynamic tests. In these tests, the force may be applied as a sinusoidal time function, expressed in Equation 2.3, which generates a time-dependent strain. Some aspects of viscoelasticity are better described by creep and recovery tests and others by dynamic ones. In the latter, one can relate viscosity and elasticity with the frequency of the applied stresses (Schramm (2009)).

$$\tau = \tau_0 \cdot \sin(\omega \cdot t) \tag{2.3}$$

These tests are possible in traditional rotational rheometers because the rotor (upper plate or cone) is made to turn accordingly to the sinusoidal time-function, for a small angle (less than 1º) , to the left and right.

For viscoelastic samples, the resulting stress is measured with stress amplitude, τ_0, angular velocity, ω, and phase angle, δ (time lag between imposed strain and stress response curves (Mezger (2015))), as stated in Equation 2.4, in which the angular velocity is linked to the oscillation frequency by $\omega = 2\pi \cdot f$ (Schramm (2009)).

$$\tau = \tau_0 \cdot \sin(\omega \cdot t + \delta) \tag{2.4}$$

It is common to introduce G^*, the complex modulus, which represents the total resistance of a substance to an applied strain, $|G^*| = \tau_0/\gamma_0$. The complex modulus and the phase angle are frequency dependent, for real viscoelastic materials, forcing the tests to be conducted at an assigned frequency range, plotting G^* and δ as a function of frequency. The data must, then, be transformed into the viscous and elastic components of the viscoelastic behavior of the sample.

The complex modulus can be defined as described in Equation 2.5.

$$G^* = G' + iG'', \text{ in which}$$
$$G' = G^* \cos{(\delta)}, \text{ the elastic or storage modulus, and} \qquad (2.5)$$
$$G'' = G^* \sin{(\delta)}, \text{ the viscous or loss modulus}$$

The term storage modulus indicates storage of energy during the test and its possible recovery after it (elastic behavior), and loss modulus indicates that the energy used to initiate flow is lost by transformation to shear heat (viscous behavior) (Mezger (2015)).

If the substance is purely viscous, $\delta = 90°$ and $G' = 0$. If the substance is purely elastic, $\delta = 0°$ and $G'' = 0$ (Schramm (2009)). A material can identified as a fluid if its phase shift, δ, lies between 45º and 90º. These are self-leveling at rest and have no dimensional stability. On contrary, for the solid, gel-like state, δ is between 0º and 45º. These materials are solid at rest. Also, if a material is more viscous than elastic ($G'' > G'$), it is a viscoelastic fluid. If, on contrary, a material is more elastic than viscous, it is characterized as a viscoelastic solid (Wirtz (2009)).

Within the linear region, it is possible to convert between $G(t)$, $J(t)$ and $G^*(t)$, which makes the experiments equivalent. $G^*(t)$ is proportional to the one-sided Fourier transform of $G(t)$, and the inverse Laplace transform of $J(t)$ is related to $G^*(t)$ (Cicuta and Donald (2007)).

Biological materials, such as cells or tissues, show dependence between their rheological particles and the rate of deformation, in this case, oscillation frequency, ω. Both G' and G'' depend on ω. At low frequencies, the cell cytoplasm has time to reorganize the cytosqueleton polymers between consecutive deformations, being able to flow, just like a viscous liquid. On the other hand, at high frequencies, the cytoplasm cannot reorganize, behaving like an elastic solid, resisting to deformation. This could mean that one has to be extremely cautious when measuring the response of cells and tissues to shear stress, since considering the frequency dependence is crucial. The task would be tedious and create highly inaccurate results if performed with the typical oscillatory methods, but, to solve this and many other problems, microrheology is used. This technique can obtain the viscous and elastic moduli in a matter of seconds, by analyzing the dynamic movements of submicron probe beads embedded, for instance, in a cell's cytoplasm, without external forces or deformations (Wirtz (2009)). Microrheology will be detailed in the next section.

2.2   Microrheology

Microrheology is the study of the stress-strain relation for small material volumes (in the order of a micro-litre), allowing the determination of rheological properties of a complex fluid from the motion of micron-sized colloidal (Cicuta and Donald (2007)) tracer particles embedded in it (Campo-Deaño (2018)). It arises as a way to overcome volume limitations, for example, when trying to probe the rheological properties within cells, to understand biological motility, or when trying to acquire rheological measurements of purified biomaterials available only in small quantities (Mason et al. (1997)). It also overcomes some macroscale rheology limitations, such as

working with soft complex fluids, with low viscosity or low elasticity, and prone to evaporation (Campo-Deaño (2018)).

This technique has been used to investigate about the cystosqueleton scaffold of animal cells, namely coming to the conclusion that mechanical moduli of entangled actin filaments *in vitro* are orders of magnitude smaller than in cells. This way, the importance of crosslinking in this particular scaffold was highlighted. Few systems are as small and spatially heterogeneous as the cell, and a bulk-average technique could never arrive to such precise conclusions. Thanks to microrheology, it was shown that the region near the nucleus has much higher moduli than the periphery of the cell. Another example was the analysis of directional anisotropy in dense sheared solutions of DNA (Cicuta and Donald (2007)). At a larger scale, comes the study of the microrheology of bacterial biofilms *in vitro*, detailed in Rogers et al. (2008), which comes to important conclusions about the communal lifecycles of bacteria that adhere to solid surfaces. For example, it was observed that *Staphylococus aureus* biofilms become less compliant during growth, and more compliant during starvation. More, the rheological homogeneity at the micron scale becomes more patent in matured biofilms. Because particle-tracking microrheology can provide a quantitative measure of the "strength" of a biofilm, it can be useful for the identification of drug targets, or even the characterization of the micron-scale rheology of biofilms, given specific molecular changes. On the latter subject, the work detailed in Ma et al. (2017) uses microrheology to characterize the effect of a *Staphylococcus epidermidis* population, not in a biofilm, but in fibrin clots, highlighting the dangers of medical device infection. These infections can be correlated with thromboembolisms, since bacteria present during clot formation produce a disorganized microstructure, which increases clot stiffness and triggers mechanical instability over time. The embolization of a clot can, then, contribute to the systematic dissemination of the pathogen.

In an early phase, microrheology studies were conducted tracking colloidal magnetic beads driven by a magnetic field gradient, but soon it was concluded that, since many complex fluids and biomaterials are fragile, with yield strains much smaller than unity, magnetic forcing could actually alter the local structure around the sphere. Smaller stresses should be applied when conducting these studies, such as the ones arising from thermal fluctuations (Mason et al. (1997)). This way, microrheology is applied to measure the rheological properties of a medium, such as microviscosity, via the measurement of the trajectory of flow tracers, which are micrometre-sized particles.

Microrheology can be either passive, based on the observation of a thermally excited particle on the micron order, suspended in the solution under investigation, or active, based on the response of a single micro-bead to an external force field, which can be generated by optical or magnetic tweezers. Both techniques directly relate the bead trajectories to the viscoelastic properties (i.e., viscoelastic moduli G' and G") (Campo-Deaño (2016)), inside and outside the linear viscoelastic region (Campo-Deaño (2018)).

The most common experimental methods of microrheology involve video particle tracking, laser tweezers or magnetic tweezers. In the early days of microrheology, dynamic light scattering (DLS) was used for viscosity and viscoelasticity measurements, acquired through the scattered

light's time-correlation function, with or without scattering tracer particles. Measuring at different scattering angles, one could create a spectrum of different modes for the material. Because DLS is limited to transparent samples, which restrains the study of complex fluids, diffusive wave spectroscopy (DWS) was developed. DWS uses the information of the time-correlation function of scattered intensity contained in the limit of multiple scattering, which allows for the extension of DLS to opaque systems, such as colloidal pastes and foams. Both methods are bulk techniques, having the limitations of large (in the order of milliliters) sample sizes and inability to solve spatial heterogeneity (Cicuta and Donald (2007)).

Later on, characterization of the linear viscoelasticity of a matrix started to be done by the video analysis of trajectories of tracer particles. Video particle tracking for microrheology monitors particles through an optical microscope, either in bright-field or fluorescence mode, depending on the nature of the tracers. In order to obtain the mean-square displacement of the particles, videos are recorded with a CCD camera, and each movie frame is analyzed to find particle positions. Spatial resolution of video microscopy is determined by optical magnification and CCD pixel density. In earlier times, the CCD camera would capture at a 30 Hz frame rate, creating an image of 640 x 480 pixels, but as computer speed and memory keep increasing, direct capture of digital video is achieved, with a much higher resolution. The statistics gathered from this analysis are of increased relevance if the videos are long enough, and the number of particles is sufficient, but the frame rate is limited by the used technology (camera and computer) and the acquired data is greatly redundant. Also, the analysis of the data needs to be done after its acquisition (offline method). Alternatively, using an optical tweezer setup, tracking can be done by imaging the light scattered of one or two particles at a time. Using this method, one can assure a sampling frequency that is limited only by the particle inertia, no redundancy in the data (less data storage required) and the possibility of online analysis. With any of the methods, a displacement in the order of the nanometers of a micrometer-sized particle can be measured (Cicuta and Donald (2007)).

This technique is based on Stokes-Einstein equation (Equation 2.6), which relates the diffusion coefficient, D, the bulk viscosity η, and the tracer particle radius, a. In this equation, T is the absolute temperature and $k_B T$ is the thermal energy that drives motion, with k_B as the Boltzmann constant. $6\pi\eta a$ is the friction coefficient of the bead in the liquid (Wirtz (2009)). This equation is valid for a particle undergoing Brownian motion in a quiescent Newtonian viscous fluid, at uniform temperature (Cicuta and Donald (2007)). Brownian motion is defined as the random movement of particles suspended in a fluid, which results from their collision with atoms or molecules, when the particles are smaller than $1\mu m$, allowing for the inertial forces to be negligible (Wirtz (2009)).

$$D(a) = \frac{k_B T}{6\pi\eta a} \tag{2.6}$$

This equation allows for the formulation of the mean squared displacement (MSD) formula, which states that, in a two dimensional plane (as in optical microscopy observations), the displacement of a particle is proportional to the diffusion coefficient and lag time (Equation 2.7) (Cicuta and Donald (2007)). Each time the particle moves in a certain direction, it "loses mem-

ory" of where it just came from and the next step occurs in a random, uncorrelated direction (Wirtz (2009)).

$$< \Delta r^2(t) >= 4Dt \tag{2.7}$$

The combination of the previous expressions explains why one can determine a fluid's viscosity by tracking small beads that are thermally excited, inside the fluid. These beads' random motion is translated in their MSD, which can be correlated to viscosity through Equation 2.8. $<>$ Refers to the time averaging of each of the tracer particles (Wirtz (2009)).

$$\eta = \frac{2k_B T}{3\pi a} \frac{t}{< \Delta r^2(t) >} \tag{2.8}$$

In practice, tens to hundreds of particles would need to be tracked, in order to assure statistical averaging (Wirtz (2009)). In this case, one uses the ensemble-averaged MSD, $<< \Delta r^2(t) >>$, the mean of all measured MSDs. If $\frac{t}{<\Delta r^2(t)>}$ is not constant, it is likely that the suspending fluid is a viscoelastic material, instead of a viscous liquid (Wirtz (2009)).

For the measured coordinates of each bead, $x(t)$ and $y(t)$, the MSD is given by $< \Delta r^2(t) >=< [x(t) - x(0)]^2 + [y(t) - y(0)]^2 >$. If the material is isotropic, which is a condition for these formulations to be true, then $< [x(t) - x(0)]^2 >=< [y(t) - y(0)]^2 >$, and therefore $< \Delta r^2(t) >= 2 < [x(t) - x(0)]^2 >= 2 < [y(t) - y(0)]^2 >= 4Dt$ (Wirtz (2009)).

Because it is known that the properties of viscoelastic fluids are time dependent, one can think that a way of diagnosing the properties of a material is to observe the time dependence of the MSD of beads inside it (Wirtz (2009)). Just by observing the movement of beads in two different materials, one can know which one is more elastic or viscous. One can think of the basic physical principal which states that, in general, the amplitude of the tracer motion is inversely proportional to a material's stiffness (Crocker and Hoffman (2007)). Also, if the MSD of the tracers increases linearly with lag time, the fluid in study behaves as a viscous liquid, and, on the other hand, it is characteristic of an elastic solid that the MSD of the beads is independent of the lag time. Therefore, an elastic component on a viscoelastic fluid can be noted as the MSD increases more slowly than linearly, with lag time (Crocker and Hoffman (2007)).

Combining the behaviour of viscous and elastic fluids, so as to model the movement of particles in complex, viscoelastic fluids, one must consider frequency dependence of the viscous and elastic moduli, as stated in Equation 2.5. Overcoming this dependence, which is essential to formulate the analysis of a tracer movement to the general viscoelastic case, Mason and Weitz proposed the "generalized Stokes-Einstein" equation for movement in two dimensions (Equation 2.9). In this equation, s is the Laplace frequency, $\Delta \tilde{r}^2(s)$ is the Laplace transform of $\Delta r^2(t)$ and $\tilde{G}(s)$ is the Laplace transform of $G(t)$ (Cicuta and Donald (2007)).

$$< \Delta \tilde{r}^2(s) >= \frac{2k_B T}{3\pi a s \tilde{G}(s)} \tag{2.9}$$

When comparing the results of viscoelasticity modules acquired by the theoretical response of

simplistic systems, such as the previously mentioned Maxwell model, and the same values for the analysis of an artificial MSD dataset that simulates the same simplistic model, problems at low frequencies, introduced by the Laplace transform (Equation 2.9), which is ideally evaluated for an infinite set of frequencies, and is approximated with a finite lag time set, are highlighted. Less severe problems are present in high frequencies (Cicuta and Donald (2007)).

The generalized Stokes-Einstein equation can also be written as stated in Equation 2.10. In this equation, G^* is the complex modulus in function of frequency and $< \Delta r(\omega^2) >$ is the Fourier transform of the MSD. From this equation, one can extract $G'(\omega)$, the real part, storage modulus, and $G''(\omega)$, the imaginary part, loss modulus. These represent the solid-like and liquid-like behaviors of the material (Cicuta and Donald (2007)).

$$G^*(\omega) = \frac{k_B T}{i\omega < \Delta r(\omega^2) > \pi a} \qquad (2.10)$$

This equation can also be written using the fluid's compliance, result of a creep experiment (Equation 2.11), which does not require considering frequency dependence.

$$< r^2(t) >= \frac{k_B T}{\pi a} J(t) \qquad (2.11)$$

In case of a viscous liquid, in which $G' = 0$, it can be shown that the viscous modulus is simply $G'' = \eta \omega$, in which ω, the frequency of deformation, is equal to the inverse of lag time, $\omega = 1/t$. This shows how viscous fluids react by increasing the viscous modulus linearly with increase in the deformation frequency (Wirtz (2009)).

As for the mean square displacement of particles in purely elastic media of modulus G_0, one must acknowledge that the particles have a spring-like position fluctuation around their initial position, which is considered in Equation 2.12 (Cicuta and Donald (2007)). This means that, each time a bead is moved by thermal energy in a random direction, the elastic material will push it back, with equal force, in the opposite direction. The MSD of the bead is finite but constant, $< \Delta r^2(t) >= K$, being independent of time (Wirtz (2009)).

$$< \Delta r^2(t) >= \frac{2k_B T}{3\pi a G_0} \qquad (2.12)$$

Because the viscous modulus of an elastic solid is null, the previous equation can be written as in Equation 2.13. Such equation proves that G' is a constant independent of ω, and inversely proportional to the MSD of the beads. This means that one can calculate G' of an elastic solid through particle-tracking measurements of MSD without considering its temporal component (Wirtz (2009)).

$$G'(\omega) = \frac{2k_B T}{3\pi a < \Delta r^2 >} = \frac{2k_B T}{3\pi a K} \qquad (2.13)$$

Because tracer particles solutions may either be surrounded by solution particles or by a depletion layer, it is necessary to eliminate the effects of their interaction from the final calculations and measurements. For this purpose, 2-particle correlations are done, calculating the fluctuations as

function of the distance between pairs of particles. These correlations are not affected by the surroundings of each one of the tracer beads, providing the correct response of the bulk matrix. Because the analysis requires video data for many pairs of particles at many distances, a much more extensive amount of data needs to be acquired in relation to measurements with one single particle (Cicuta and Donald (2007)).

One-point microrheology and two-point microrheology are, in fact, distinct methods, each with advantages and drawbacks. As previously detailed, one-point passive microrheology uses the generalized Stokes-Einstein equation to determine the shear modulus from each measured single-particle mean-squared displacement. Converting between the MSD and the complex shear modulus can be readily done using the Fourier, Laplace and lag time domains, using simple numerical routines. However, the generalized Stokes-Einstein relation can only provide with the shear modulus if the medium is homogeneous on the scale of a. Otherwise, the relation can lead to underestimation of this modulus. Moreover, this relation is only valid in a certain frequency range, whose lower limit (around 1 Hz) is the frequency below which compressional modes become more significant than the shear modes that are excited in a polymeric network (thermally driven probes respond to all the thermally excited modes of the system, including compressional modes of the elastic network), and the upper limit is the frequency at which inertial effects are visible at the length scale of the bead, and the assumption of neglecting inertia, necessary for using the Stokes-Einstein equation, is not valid. For typical soft materials studied with passive microrheology, with densities around 1000 kg/m^3 and tracer beads with radii around 0.5 μm, this occurs around 20 kHz. However, macrorheology is limited by inertial effects at around 50 Hz. Another limitation of one-point passive microrheology is the aforementioned inhomogeneity introduced in the sample by the probe particles. To overcome this last problem comes two-point microrheology, which takes advantage of interparticle coupling to delete the influences of interactions between each particle and its surroundings, such as boundary effects at the particle-material interface. This technique requires the definition of a mobility correlation tensor, $D_{\alpha\beta}$, which represents the degree of correlation between the tracers' motion during lag time τ versus their separation, R. This tensor is represented in Equation 2.14. In this, i and j represent two tracers, α and β represent different coordinates and R^{ij} is the distance between the particles i and j. The tensor can be decomposed into a longitudinal and a transverse component, which are, respectively, drawn along the center-to-center separation vector, and orthogonal to this separation vector (Chen (2010)).

$$D_{\alpha\beta}(r,\tau) = <\Delta r_{\alpha}^i(t,\tau)\Delta r_{\beta}^j(t,\tau)\delta[r - R^{ij}(t)] >_{i \neq j,t}, \qquad (2.14)$$

For an incompressible medium, the longitudinal tensor components' magnitudes are greater than the magnitudes of the transverse components by a factor of two. Because the longitudinal component, now designated D_{rr}, has less dependency on the bulk modulus (relative to bulk deformations that may occur in the fluid) than the transverse component, depending mostly on the shear modulus of the medium, and because D_{rr} is the strongest component, easier to measure from a signal-to-noise perspective, the shear modulus can be determined using only this term. This can

be seen in Equation 2.15 (Chen (2010)).

$$\tilde{D}_{rr}(R,s) = \frac{k_B T}{2\pi R s \tilde{G}(s)} \qquad (2.15)$$

When deriving the previous equation, one arrives to the definition of the two-point MSD (MSD2), as can be seen in Equation 2.16.

$$<\Delta r^2(\tau)>_2 = \frac{2R}{a} D_{rr}(R,\tau) \qquad (2.16)$$

Analyzing this equation, one can figure the conditions that make the calculation of the complex shear modulus with Equation 2.15 valid. The latter is not dependent on a, the radius of the tracer, suggesting that the modulus is calculated independently of the tracer's size, shape and boundary conditions, but only if $R >> a$. Moreover, if the material is homogeneous, isotropic on length scales smaller than the tracer, but also incompressible and connected to the tracers by boundary conditons that are uniform and no-slip over the tracers' surfaces, then the MSDs calculated with one or two points will be equal. If these conditions are not satisfied, then the two-point technique should be used, since the MSD calculated for one particle will report results that arise from the superposition of the bulk rheology of the material and the local rheology at the tracer boundary (Chen (2010)).

Microrheology through video particle tracking, following the one-particle method or the approach that correlates the motion of pairs of particles, has several advantages in comparison to traditional rheology: it allows for a wide movement frequency range; it is a local probe, not a bulk method, being suited for heterogeneous systems; it can be used with samples with low elasticity and viscosity (the signal arising from these is too weak for traditional rheometers); it is an affordable method (a state-of-the art rheometer can cost up to $100.000, and particle tracking through video analysis can be done with a regular optical microscope and a video camera); it requires a sample volume which can be as small as 100 μL, whereas traditional rheometers require samples with a few milliliters; it is applicable to non-conventional geometries, such as lipid bilayers. On the other hand, this set of methods has limitations: its use for non-linear response study is difficult; materials subjected to microrheology techniques must be at least partially transparent to light (unless X-ray scattering is being used); it is computationally intensive, requiring up to ten minutes of video and variable analysis time; and very small motion in very stiff or viscous materials is challenging to observe (depending on the frequency resolution) (Cicuta and Donald (2007)).

2.3 Hemorheology

Blood is a complex fluid, whose behaviour is given by the mixture of components it concerns: red blood cells, platelets, white blood cells and plasma, which contains other elements. The red blood cells are the most abundant components (99.9% of the cellular elements of blood and between 36% and 54% of the blood volume), being responsible for the rheological behaviour of the blood. When the blood is at rest for several seconds (at low shear rates), in the presence of fibrinogen

and other plasma proteins (Crocker et al. (2000)), the red cells begin to agglomerate, leading to the formation of a network, which is successively extended, giving rise to a solid-like behavior. The agglomerates increase the blood's resistance to deformation and diminish its elastic response. This way, agglomerate formation makes the blood's elastic response negligible under certain flow conditions and it is expected that the viscoelasticity of blood increases with hematocrit (volume fraction of red blood cells), but also varies with mechanical properties of blood cells (Sousa et al. (2018)).

Red blood cell agglomerates are broken by imposed shearing (when the shear rate increases), aligning with the flow and imparting a liquid-like behavior to the blood, causing a relative decrease in viscosity. Moreover, red blood cells under high shear stresses tend to deform into ellipsoids, as a consequence of tensile and compressive forces applied to different regions of the cell. This behavior can be seen in Figure 2.3. The viscoelasticity of the blood can be measured by the relaxation time, the time taken by the internal fluid structures to relax internal stresses imposed by the flow (Campo-Deaño (2016),Campo-Deaño et al. (2013)). When shear stress is removed, the blood cells return to a biconcave disc shape, with a relaxation time of around 100-300 milliseconds (Sutera and Mehrjardi (1975)).
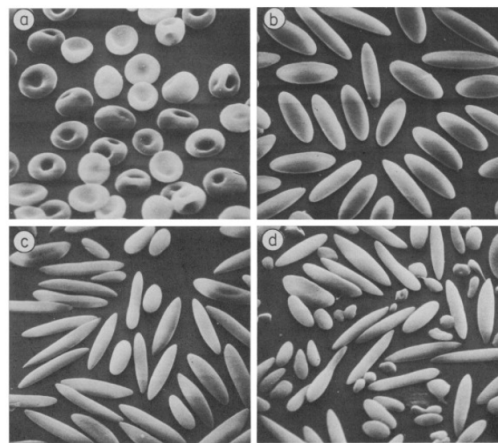
Figure 2.3: Fixed human red blood cells, subjected to shear flow in a concentric cylinder viscometer. In (a),the applied stress was 10 Pa, in (b) was 200 Pa, in (c) was 350 Pa and in (d) was 450 Pa, for 4 minutes, at 37ºC. Adapted from Sutera and Mehrjardi (1975).

The formation and rupture of these networks leads to cyclic storage and release of elastic energy. In most blood vessels, the shear rates are too high for the formation of red blood cell aggregates, but these are likely to be formed in some veins and venules. Some diseases, such as pneumonia, cause a tendency for agglomeration (Sutera and Mehrjardi (1975)).

Therefore, blood shows a shear-thinning behaviour, which can be observed better as the concentration of red blood cells increases. This means that blood becomes less viscous at high shear rates, as already detailed, which happens during physical exercise or in peak-systole. Blood viscosity increases, then, with lower shear rates, which may be caused by increased vessel diameters or low flow, due to obstruction or in diastole. Additionally, it is known that blood is a thixotropic

fluid, which may have a yield stress associated (limit point of elastic behaviour, marking the transition to plastic behavior) (Huang et al. (1987)).

At the micro-scale, flows of viscoelastic fluids such as blood can be different from those of purely viscous ones, being that the elastic effects are enhanced even at low Reynolds number, defined as the ratio between inertial and viscous forces ($Re = \frac{\rho VL}{\eta}$). The Reynolds number is one of the most common dimensionless numbers used to characterize viscoelastic fluid flows, along with the Weissenberg number, defined as the ratio between elastic and viscous forces ($Wi = \frac{\lambda V}{L}$). In these ratios, V represents the average velocity, L represents the characteristic length-scale, ρ represents density, λ is relaxation time and η represents the fluid's viscosity (Campo-Deaño (2016)). In addition, it is known that the non-Newtonian characteristics of blood make the flow properties differ in 40% to 50% from the same properties, calculated for blood considering only Newtonian characteristics. Low length-scales and the pulsatile character of blood emphasize the non-Newtonian characteristics of the fluid, even though one can assume Newtonian properties in its behavior when considering the heart or large vessels. This is because blood behaves as a Newtonian fluid for shear rates roughly above 45 s^{-1}, depending on the hematocrit level. Above this high constant shear rate plateau, the viscosity of the blood goes from 3.5 mPa·s to 5 mPa·s. Nevertheless, this assumption for small vessels is far from accurate, being that, at lower Reynolds numbers (approaching laminar flow), in these vessels, the Weissenberg number is increased, denoting the presence of viscoelastic effects. Besides small vessels, bifurcations, graft anostomoses, stenoses and aneurysms are also low shear rate zones (Campo-Deaño et al. (2015)).

The study of non-Newtonian properties of the blood affects mostly the micro-circulation (small vessels) and is of extreme relevance, given its relation with cardiovascular diseases (Campo-Deaño (2016),Campo-Deaño et al. (2013)). In fact, modeling blood as a viscoelastic non-Newtonian fluid is mandatory for a complete understanding of its rheological properties' role in middle cerebral aneurysms. The growth and rupture of these structures are not well understood yet, although it is known that they depend on the action of flow-induced mechanical stress on vessel walls, which are conditioned by pressure and hemodynamic stress. Blood flow strongly depends on its rheology, along with geometrical features of aneurysms, in this specific case (Campo-Deaño et al. (2015)).

In a study aimed for the development of transparent non-Newtonian blood analogues that a exhibit rheological behavior, under shear and extension, very similar to that of real whole blood, Campo-Deaño and her team (Campo-Deaño et al. (2013)) present the complex moduli for blood, obtained via passive microrheology (together with other rheology studies). This study was motivated by the lack of reliable substitutes for blood in hemodynamics studies. These studies use to be conducted in vitro, given the possibility of a greater flow control. Real blood is not regularly used in in vitro experiments because its manipulation and the study of its flow dynamics are difficult in these conditions, given their cost, safety, and ethical issues involved. Moreover, the erythrocytes could be damaged in vitro, in the absence of oxygen and nutrients, leading to a change of their properties. Also, the rheological properties of blood at room temperature are different from those at body temperature. Because of this, blood analogues which mimetize blood's viscoelastic properties are usually required (Campo-Deaño et al. (2013)).

There are many techniques to study the complex rheological behaviour of the whole blood, which can be subdivided in macrorheological and microrheological techniques. The small blood sample volumes give microrheology some advantage over macrorheology, along with short measurement acquisition times, and the theoretical extension of the accessible frequency range, by shifting the onset of inertial effects to the MHz regime, due to the use of small colloidal particles (Campo-Deaño (2016)). Campo-Deaño et al. used microrheological techniques to measure the viscous and elastic properties of human blood, as the conventional rheology did not offer enough sensibility for the measurement (Campo-Deaño et al. (2013)).

To evaluate the rheological characteristics of blood, the experiments that can be conducted (and were conducted in Campo-Deaño et al. (2013) and Sousa et al. (2013), for example) are the acquisition of shear rheologial properties, with a stress or strain-controlled shear rotational rheometer, rheological extensional flow experiments, with a capillary break-up extensional rheometer, and one-point or two-points passive microrheology, with an inverted microscope and a high precision sample chamber cell.

Oscillatory shear tests can evaluate both elastic and viscous contributions to viscoelastic response. In Sousa et al. (2013), it is verified that the viscous component of blood prevails over the elastic one through such tests.

The work of Sousa et al. (2013) aimed to verify the nonlinear viscoelastic response of blood through the application of large amplitude oscillatory shear under strain control, confirming the influence of oscillatory shear in the modification of the blood microstructure. In this study, the effect of anticoagulant agents on blood's shear viscosity could also be observed, through steady-state shear rheology. The steady-shear viscosity assessment shows the shear-thinning character of blood through the decrease of the viscosity values with an increasing shear rate, at physiological temperature (37ºC). Moreover, the comparison of the viscosity of blood with and without adding EDTA anticoagulant, at the maximum admissible concentration to prevent coagulation, showed that the viscosity-shear rate relations are similar with or without anticoagulant addition, at least during the first 8 minutes after blood collection. 8-9 minutes after blood collection, the viscosity results of the sample without anticoagulant start to deviate to higher values at higher shear rates, probably due to the onset of blood coagulation.

The results of large amplitude oscillatory shear tests showed that, even though the imposed strain waveform is sinusoidal, the shear stress that is measured clearly deviates from the sinusoidal function at a strain amplitude of 10, but approaches it when the deformation is increased to 100, while being out of phase by $\pi/2$ relative to the imposed strain. The changes in the shape of the shear stress waveform are hypothesized to be related to alterations in the microstructure of blood. For instance, at lower strain amplitudes, red blood cells may be aggregated, leading to the formation of weak structures, which are broken at higher deformations. Through the analysis of normalized Lissajous-Bowditch plots, of shear stress as a function of strain, it is verified that intra-cycle strain-stiffening occurs for all strain amplitudes investigated and intra-cycle shear thinning behavior is confirmed.

Moreover, viscosity curves plotted by shear stress tests made by Valant et al. (Zupančič Valant
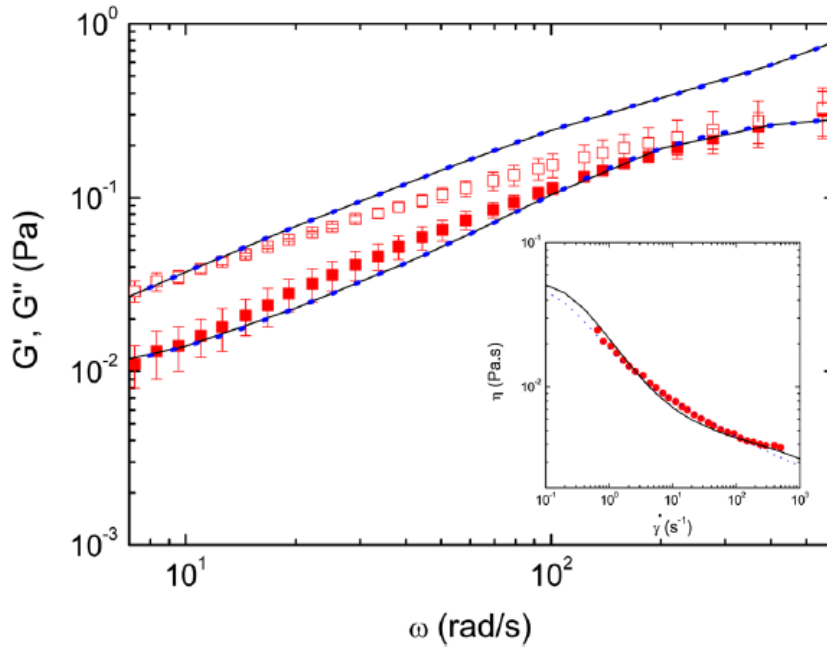
Figure 2.4: Storage (red filled squares) and loss (red empty squares) moduli of blood, rescaled from 27ºC to 37ºC using time-temperature superposition, and fits to multi-move Giesekus (solid line) and sPTT (blue dots) models. The human blood sample used for this curve has an hematocrite of 44%. The inner figure shows comparison between the steady shear viscosity curve (red circles) obtained by Zupančič Valant et al. (2011) and model fits. Adapted from Campo-Deaño et al. (2013).

et al. (2011)) have reported that blood viscosity, for several healthy donors with different hematocrit values, at 37ºC, is clearly marked by shear-thinning behavior, confirming again contributions of viscosity and elasticity in the rheology of whole blood. The high constant shear rate plateau can be observed. To quantify the relative magnitude of these components in viscoelasticity of blood, passive microrheology experiments are carried out. The results of these experiments are shown in Figure 2.4. These were indirectly obtained for the temperature of the human circulatory system (37ºC) by the time-temperature superposition principle (which allows the determination of temperature-dependant properties of linear viscoelastic materials from known properties at a reference temperature). By analyzing these results, one can observe a clear liquid-like behavior, but the difference between the curves for G' and G'' is not significant, especially at high frequencies, which corroborates the elastic component on blood's bulk rheology (Campo-Deaño et al. (2015)). Together with the representation of storage and loss moduli for blood, Figure 2.4 presents the fits to multi-mode Giesekus and sPTT models, which concern constitutive equations for blood rheology. These models provide an approximation to the viscoelastic behavior of blood flow. Nevertheless, a viscoelastic model mimicking perfectly the behavior of real blood flow is still missing. It is very useful to create models for the non-Newtonian behavior of blood, since pathologies such as the referred aneurysms are far from being completely understood and predicted, and in vivo tests are

not practical, and, in some cases, not possible. The previously mentioned models mimetize the rheological behavior in steady and oscillatory flow and are used to predict, numerically, the flow in pathological conditions, since these are valid in high strain and high-strain rate regimes, being capable of predicting shear-thinning and normal stress effects in blood. Ideally, these models should include memory effects and the specific mechanisms that affect blood's rheological properties, such as the formation of agglomerates and their disruption (Campo-Deaño et al. (2015)).

Chapter 3

Literature Review

Particle tracking stands for the process of following particles through time, acquiring and analyzing their trajectory. The particles are usually detected in a digital video sequence, resultant from video microscopy, and these detections are linked over time, to follow the track of each one, via automated computational methods (Sbalzarini and Koumoutsakos (2005)). Particle tracking has been used for multiple applications, such as quantitative analysis of intracellular dynamic processes using time-lapse microscopy image data, since doing manual detection and analysis of the motion of large numbers of individual particles ("multi-particle tracking", in opposition to "single-particle tracking", in which it is simpler to create manual annotations on the particle movements) is not feasible (Chenouard et al. (2014)). Also, if one wants to obtain statistically sound conclusions, the tracking must be performed for a large number of particles (Godinez et al. (2011)).

Particle tracking is gaining importance among biology tools for studying dynamic processes at micrometric and nanometric scales, but there is still a limited number of studies in this area, indicating that the existent solutions are narrow and do not completely satisfy the biologists' needs for automatic, flexible, and reliable methods, capable of analyzing a great variety of biological data. There is considerably more work in tracking algorithms for very specific applications than for generalizing the methods to a great range of conditions that can be met in cellular and molecular biology.

A particle may be anything from a single molecule to a macromolecular complex, organelle, virus, bacteria or microsphere, reason why examples of uses of tracking methods go from the study of biofilms to blood clots, colloids, biological matrices, cell membrane dynamics to cytoskeletal filaments, focal adhesions, viral infection, intracellular transport, gene transcription and genome maintenance (Chenouard et al. (2014)), but also determination of diffusion coefficients and transport velocities (Sbalzarini and Koumoutsakos (2005)). By tracking these particles, we can acquire data for quantitative characterization of the spatial-temporal processes of the structures (Godinez et al. (2011)). We can also find tracking in fields such as fluid mechanics (e.g., particle imaging velocimetry, microrheology), computer vision (e.g., human limb tracking), and navigation (Sbalzarini and Koumoutsakos (2005)).

The most common tools developed for particle tracking can have their base image analysis

methods divided into two steps. The first step to be analyzed is the spatial aspect, which is the particle detection. In particle detection, the particles are identified and separated from the image background according to specific criteria, leading to the estimation of their coordinates. The coordinates are estimated in every frame of the image sequence. Particle linking is the temporal aspect, in which detected particles are connected frame to frame using another set of criteria to define tracks. These steps may be performed once or iteratively (Chenouard et al. (2014)).

The methods that separate particle detection and linking are named point correspondence methods (methods that solve a point correspondence problem). They were the first ones to be used in biology applications in an automated way, since they are simple and widely used in other fields. These methods are quite general, which is favorable if one aims to work with a variety of particle environments. Despite these advantages, point correspondence methods require a high acquisition rate, in comparison with the targets' movements, and the signal-to-noise ratio, SNR, must be as high as possible. Conditions such as the described optimal ones are rarely found in images that show nanometric particles, for example. To use these methods out of the scale for which they were conceived implies being out of the range where the movement assumptions are valid, which can result in false tracks. However, point correspondence methods have acceptable results with bright particles (Chenouard (2010)), when the processed image sequence does not show too many objects, and these are easily identifiable (differentiated from the background) and move slowly, in comparison to the acquisition speed.

However, one-step methods are also possible. These consider tracking as a global optimization problem and do not use a frame-to-frame detection. They perform simultaneously detection and linking of particles, so as to exploit temporal information and trajectory smoothness. These methods aim to overcome false and missing detections and to compensate for poor quality of images.

Smoothness of motion is a concept exploited in many tracking approaches, that states that, due to inertia, instant changes in an object's motion are not possible. Therefore, if a frame sequence is acquired at the appropriate frame rate, at which no dramatic changes take place between two consecutive frames, there will be no abrupt changes in an object's motion (Sethi and Jain (1987)). This is a reasonable assumption when one is analyzing real world dynamic scenes, but one must be careful when adjusting frame rate to a target's speed, so that smoothness of trajectories is assured and the tracking methods remain valid.

Probabilistic methods for particle tracking can also be designed (Godinez et al. (2009), Arulampalam et al. (2002)), which aim to the definition of tracking score functions that correspond to a statistical behavior of particles. These methods may account for different motion types, intensity fluctuations and appearance and disappearance of particles. Even though these techniques offer numerous advantages comparatively to the previously mentioned, they are still limited by the apparent unpredictability of some movement types.

If the tracking algorithms are developed to be application-specific, they can incorporate *a priori* knowledge about the imaging conditions and physics of the problem, to increase robustness. The incorporated knowledge may be limited in, for example, biological applications, in which the

tracking of objects whose type of movement may not be known in advance is needed. There may be no explicit mathematical model because of the possible stochastic movement or because the trajectories include several modes of motion. Motion types may include free diffusion, confinement of objects to a very small volume, movement on a very long distance radius with a high or low velocity, movement confined to interactions with the cytosqueleton, and movement with smooth and non-smooth parts (there may be transitions between different motion types for a given object) (Chenouard (2010)). On the other hand, biological applications often only require analysis in two dimensions, since the motion is either two dimensional (such as in the plasma membrane) or is observed using "two-dimensional" microscopy techniques, such as confocal microscopy.

When the target objects are fluorescent particles, from fluorescence microscopy imaging techniques, one needs to consider that the labeling is often spread, not specific to the targets. This spreading of the fluorescence creates a dynamic background in images, which can be wrongly considered as a set of particle candidates. An example of a frame with associated difficult processing is present in Figure 3.1. For these cases, methods should be developed to create tracks containing less false detections, while missing detections need to be compensated for. This problem could be addressed by enhancing detection in each frame, improving the linking methods, or by creating effective one-step methods that could deal with dynamic backgrounds.
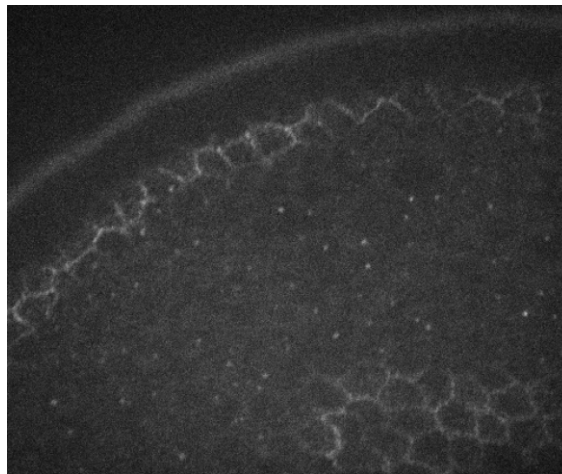
Figure 3.1: Slice of the 3D stack of an example of fluorescence microscopy image of labeled notch protein in a Drosophila melanogaster oocyte. Adapted from Chenouard (2010).

In this section, some tracking tools, algorithms and their applications will be presented and discussed with more detail.

3.1   Particle detection

Separating tracking in its two sub-problems, we can generate specific algorithms for each one and combine them.

Particle detection may be done by model fitting, a technique which finds the particle locations by varying parameters of a model to acquire the best fit. This technique uses a least squares

method or maximum likelihood estimation (MLE) to determine the mathematical model that better adapts to the particle image. The mathematical model that is more common in this problem is the Gaussian one. Modeling asymmetric or out-of-focus particles through model fitting is a complex problem. Methods that do not use model fitting are well-suited for experiments in which the particle image is distorted. An example is the Centroid Technique, which tested against Gaussian fitting and the Radial Symmetry method in Parthasarathy (2012). The latter is another non-fitting method, which draws lines orthogonal to contours of constant intensity in the image, considering the particle center as the point closer to the line intersections.

The aforementioned methods will be presented in this section, along with detection through top-hat filtering and learning methods. Some recurrent techniques that appear in many of the approaches are thresholding, local-maxima finding, morphological processing and centroid estimation.

It is known that detecting particles in images is intrinsically connected to the acquisition protocol of said images. The properties of the signals vary for different imaging modalities, and, for each modality, additional variability is introduced by different sample types (Chenouard (2010)). In this section, particle detection methods for several imaging modalities are detailed. However, most of the methods that address particle tracking problems are applied to fluorescence microscopy, which leads to the presentation of several alternatives in this topic.

3.1.1   Particle detection in fluorescence microscopy images

Fluorescence microscopy is an imaging technique in which the light emitted from activated fluorophore targets is collected and measured, to get information about the objects' presence, number, distribution and localization. Fluorescent staining is used to highlight the objects of interest, and unstained objects emit no signal or a very low quantity of it, being totally or nearly invisible. Fluorophores are activated by illumination by a lamp or laser beam mounted in the microscope. To activate a type of fluorophore when several are present, one must only control the emitted wavelength (Chenouard (2010)).

A popular use of fluorescence microscopy is immunostaining, in which an antigen (the protein of interest) is labeled with a fluorochrome-labeled antibody, which is specific to that antigen, so as to purify the protein. Furthermore, cloning the green fluorescent protein gene from jellyfish, it was possible to develop fluorescent proteins as molecular tags, which can be fused with proteins of interest. These molecular tags can be incorporated in other proteins, through genetic modification, and allow for *in vivo* immunostaining. Because, nowadays, several other colors asides from green are available, distinguishing different proteins and studying their interactions is possible. Moreover, synthetic fluorescent objects can be introduced in cells, to obtain information on the cellular mechanisms. There are many uses for fluorescent beads, which are polystyrene microspheres available in several sizes and colors. However, some cell proteins are naturally fluorescent, producing undesirable light during observations, in a phenomenon called cell autofluorescence (Chenouard (2010)).

3.1.1.1   Detection of particles knowing the particle template - Point Spread Function

The fluorescence microscopy imaging result can be considered modeled by a system that is linear and shift invariant, characterized by a transfer function whose inverse Fourier transform is the Point Spread Function (PSF) (Chenouard (2010)). In simpler words, the PSF of an imaging system describes the shape of the blur that is formed when a point is imaged through the system (Small and Stahlheber (2014)). This function already includes the occurrence of imperfections in the optical system, which create, due to diffraction, blurred spots instead of well defined points (Chenouard (2010)). The PSF is calculated through numerous factors, such as the numerical aperture of the lens, interfaces between the sample and the lens and the dipole moment of the source of light (Small and Stahlheber (2014)). However, in most cases, the theoretical PSF can be approximated by a multidimensional Gaussian function (Chenouard (2010)), even though it can differ if the image is out of focus (Small and Stahlheber (2014)).

The base of a detection method for fluorescent particles is considering that a particle can be seen as a local increase in the image's intensity. Because this type of image is characterized by low particle signal and low signal-to-noise ratio (SNR) conditions (high level of noise), this intensity increase is not detectable by pixel-wise methods. However, considering the neighbor pixels at a given position can provide additional information. Given the Gaussian shape of the PSF, previously detailed, a logical approach to follow is to exploit a filtering based detector using Gaussian models. The fundamental principle behind this technique is to design the filter that best correlates with the particles' representation shape.

In Daniel Sage and Unser (2005), it was found that the spectral density function of fluorescence microscopy images, $S_n(\omega)$, is isotropic and proportional to $||\omega||^{-s}$, with the fractal exponent $s = 1.8$, and ω as the radial spatial frequency. This function is indicative of the presence of colored noise, W, which can be converted to uncorrelated noise (whitened) by pre-filtering with the filter $H(\vec{\omega}) = ||\omega||^{s/2}$. After pre-filtering, a standard correlation detector (matched filter) is applied to enhance the spots that correspond to particles. Being P the intensity profile of a particle, the matched filter is the complex conjugate of the Fourier transform of P, and the result of applying the pre-filter and the matched filter is given by $||\omega||^{s/2}\hat{P}^*(\vec{\omega})$. It is also shown in Daniel Sage and Unser (2005) that these filters can be approximated to a Laplacian of a Gaussian (LoG) or "Mexican hat" filter, considering the approximation $s = 2$. The formula for this detector in the space domain is given by equation 3.1.

$$LoG = \Delta P(x,y,z) = \frac{1}{\sqrt{(2\pi)^3 \sigma_{xy}^4 \sigma_z^2}} \left(\frac{x^2 + y^2}{\sigma_{xy}^4} - \frac{2}{\sigma_{xy}^2} + \frac{z^2}{\sigma_z^4} - \frac{1}{\sigma_z^2} \right) e^{-\frac{x^2+y^2}{2\sigma_{xy}^2} - \frac{z^2}{2\sigma_z^2}} \tag{3.1}$$

Figure 3.2 shows a two-dimensional LoG filter for a Gaussian PSF with standard deviation of $\sigma_{xy} = 1.5$ pixels is shown. The kernel is aimed to enhance high frequency signals, so it is highly peaked, and isotropic with a null sum, which allows for slowly varying backgrounds to be attenuated.

The result of the application of this filter (although inverted) in a practical case (for enhancing
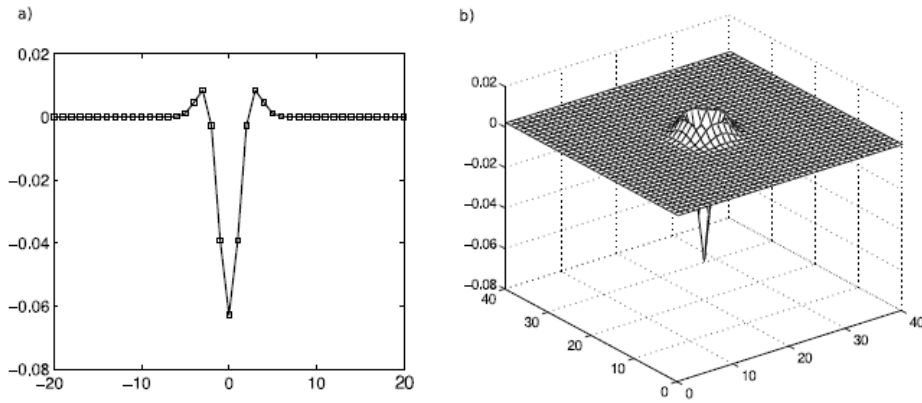
Figure 3.2: 2D Laplacian of a Gaussian filter with $\sigma_{xy} = 1.5$. In a), a section of the filter along the x-axis is represented, and in b) one can see the 3D view of the 2D LoG kernel function. Adapted from Chenouard (2010).

a particle in a fluorescence microscopy image), with and without addition of synthetic Gaussian noise, can be seen in Figure 3.3.
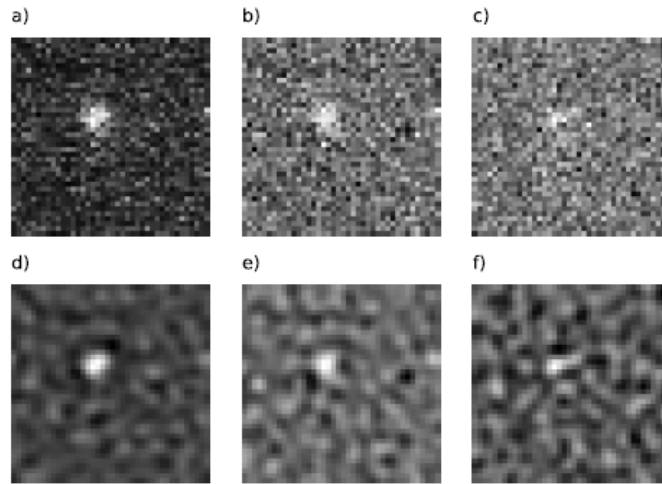
Figure 3.3: LoG filtering of a fluorescent confocal image of a bead. In a), the original image is presented, whereas in b), Gaussian noise with a standard deviation of 200 and, in c), Gaussian noise with a standard deviation of 300 are applied. d) Is the filtered result of applying the LoG filter to a), and e) and f) of filtering b) and c), respectively. Adapted from Chenouard (2010).

The authors of Godinez et al. (2009) also propose the use of LoG kernels as spot-enhancing filters, through the same methods that were detailed. After filtering, the authors apply an intensity threshold that is different for each image of the sequence. The threshold is computed as $k_{intens} = \mu_{intens} + c\sigma_{intens}$, where μ_{intens} is the mean intensity of the image, σ_{intens} is the standard deviation of the image intensities and c is a user-defined factor. Then, to identify the particles of interest, a connected components labeling algorithm is employed, assuming eight-connectivity. Finally, they reject false positive detections through a pixel number threshold. This approach can be seen

as a bottom-up localization scheme, since the authors start by enhancing spots and get to the final number of particle candidates step by step, eliminating false positives. An approach that tries to fit a 2D Gaussian function to candidate regions of interest determined by local intensity maxima, estimating both the position and appearance of a particle, can be considered a top-down scheme. This scheme starts by intensity clipping and noise reduction through Gaussian filtering, and moves to local maxima finding and 2D gaussian fitting via a least-squares estimator. This fitting is able to model each particle candidate, finding the best Gaussian profile to fit each region. One can proceed to Gaussian fitting either through the presented least-squares estimator or through maximum-likelihood estimation (MLE) (Small and Stahlheber (2014)). Least-squares fitting does not require knowledge on the camera's noise parameters, varying the model's parameters so as to find values that minimize a weighted sum of squared errors, *S*, present in equation 3.2 (Small and Stahlheber (2014)).

$$S = \Sigma_{pixels} \frac{(data - model\ prediction)^2}{expected\ variance\ of\ data} \tag{3.2}$$

MLE fitting is done through the process of finding the maximum likelihood of observing the particle distribution of intensities when the fitted model has certain parameters (e.g. the location of its center, standard deviation). Because photons are usually independent from each other in imaging techniques, the likelihood of the data can be calculated as the product of the likelihoods of the signals detected on each pixel.

The final step in this top-down approach is rejecting false positives through ellipticity, minimum total intensity, minimum contrast and maximum pixel count of the fitted region (Godinez et al. (2009)).

For separating overlapping spots, whose blurry profiles originate a single local maximum in the filtered image, (Thomann and Rines (2002)) proposed the iterative implementation of the best fitting candidate set of mixture models. The mixture model is based on the superposition of *n* shifted Gaussian functions with the same shape as the microscope's PSF. This mixture's intensity at position (x, y, z) is given by equation 3.3, in which *b* is a constant value that models the background. The number of Gaussian functions and the positions of their centers has to be calculated to comply with a trade-off between the fit of the model and the complexity of the mixture, to prevent the addition of models that do not fit the particles, but the noise. The approach to create the best fitting mixture is sequentially adding new candidate profiles until the improvement of the fit ceases to be significant.

$$M(x, y, z) = \sum_{i=1...n} P_i(x, y, z) + b \tag{3.3}$$

In Parthasarathy (2012), many disadvantages for using Gaussian fitting, either by MLE or least-squares algorithms are presented. This 2012 article states that the computation time is extreme for large data sets, and that the PSF may be wrongly estimated by the Gaussian approximations. Therefore, the fit may be optimized but the distribution to which it converges may not be the true one. More, because the fitted Gaussians have many parameters, asides from the particle center

information, such as amplitude and width of the function, a lot of computational cost is actually superfluous to the task of particle detection.

3.1.1.2   Multiscale particle detection

It is necessary to have a robust method for image cases in which there are particles with various sizes, but a similar shape. This can happen even in fluorescence microscopy images if particle representations are distorted, for example, by a non-uniform background in their vicinity (Chenouard (2010)).

To work around the need for a robust method that works in these cases, wavelet transform filtering can be used. This is a multiscale analysis method, in which the image is filtered by a kernel function that is dilated several times, to comprise with different-sized particles. The application of kernels with different degrees of dilation creates a wavelet decomposition, a dictionary of the image domain, which allows for a representation of the image in a mathematical space in which the inverse transform is possible. This way, the original image can be reconstructed from the wavelet coefficients. A wavelet representation can be considered as containing the whole information of the image, and a wavelet transform as a representation dictionary of the image domain (Chenouard (2010)). This wavelet representation is only possible when it is assumed that spots are image points of interest that can be modeled by a small number of coefficients which are large and correlated across wavelet levels (Olivo-Marin (2002)).

Because the wavelet transform can generate coefficients that are correlated, there are techniques that try to minimize the number of redundant coefficients, and, therefore, computation time. For example, in Olivo-Marin (2002), using the B3-spline as wavelet function, which is similar to the negative LoG function, the idea is to select multiple wavelet scales corresponding to the range of particle sizes, denoise them and compute inter scale product. Each wavelet application is particularly denoised because Gaussian white noise contained in the image should not propagate through scales, in opposite to the particle signal of interest. Inter scale product calculation results in high coefficients at particle locations (Olivo-Marin (2002)). The individual results and combination of the different scales of analysis is presented of Figure 3.4. There, one can see that, diminishing resolution, the filter support increases and significant coefficients in the image correspond to more significant features, of increasing spatial dimension.

3.1.1.3   Detection using Top-Hat filtering

Asides from LoG filtering and wavelet decomposition, other unsupervised techniques for spot detection are shortly detailed and compared in Smal et al. (2009). There are many methods that rely on the spot filtering capacities of Top-Hat filters (Bright and Steel (1987)). In pseudo-Top-Hat filtering, the spots are discriminated by comparing the mean intensity in a disk of radius r_{top} to the mean intensity of the circular region defined by the range of radii $]r_{top}, r_{brim}[$. The difference between the two means is used to create a threshold for binarization. This technique relies on the round shape of the particles (Chenouard (2010)). In Grayscale opening Top-Hat filtering, there
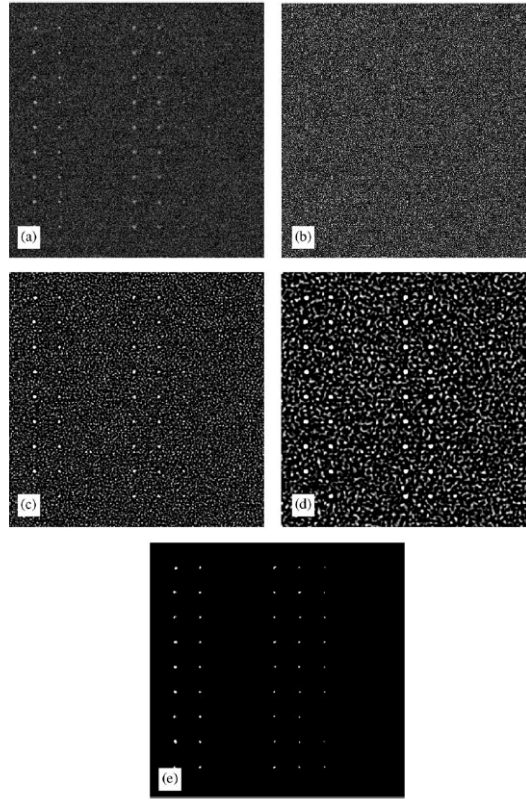
Figure 3.4: Spot detection in synthetic noisy images. **a** is the original image, with added Gaussian white noise (SNR=3.3). **b** to **d** are detail wavelets at scales 1,2, and 3. **e** shows the detected spots. Adapted from Olivo-Marin (2002).

is Gaussian smoothing followed by grayscale opening. A top-hat filtered image is the result of the subtraction between the smoothed image and the grayscale opened one. This aims to discard large background elements, keeping only the structures smaller than the grayscale opening disk (Chenouard (2010)).

These methods can be applied, not only to fluorescence microscopy images, but to all images with similar characteristics (presence of circular particles of higher intensity than the background). These methods have also in common a pipeline that begins by enhancing the signal of the spots, followed by thresholding the enhanced image.

3.1.1.4 Detection through machine learning techniques

There are other algorithm options, that do not fall in the unsupervised category. The Adaboost algorithm (Jiang et al. (2007)) is an example of such. It is based on the collection of a large number of features, named weak classifiers, which are iteratively selected or discarded from the set, so as to find the best fitting enhancement function and the optimal classifying function. In this approach, there are no *a priori* descriptors, such as knowing the intensity profile of the spots (Gaussian in previous approaches). Instead, the user has to label a training set.

The authors that implemented Adaboost machine learning algorithm (Jiang et al. (2007)) wanted to detect and separate accurately many hundreds of individual Clathrin-coated pits, to observe their transport behavior. This detection had to be made in live-cell microscopy movies, and they found that the noisy background and low contrast in fluorescence images impaired the use of single threshold, edge detection or morphological methods. The authors tried watershed segmentation, which failed to isolate attached particles, since this method is shape-based. Any method that was based on intensity failed to analyze these authors' data, which lead them to think about a combination of features.

The fully automated machine learning method they used was implemented with Haar features, which combine intensity, shape and scale information of objects, including weak and simple defined features. For further eliminating possible false positive spots, the authors study the SNR of the detected spots, eliminating the spots that show a low value of local SNR. For the application of a learning based method, the followed pipeline is described in the Figure 3.5. This pipeline can be extrapolated to the majority of machine learning problems, since they all comprise a training and test phase, after possible pre-processing. After classification is done, the performance is evaluated for adjusting parameters and feature selection. In this phase, one must be careful to avoid overfitting. Following performance evaluation, there may be a post-processing section, which may aim, for example, for the definition of the brim of the detected particles.
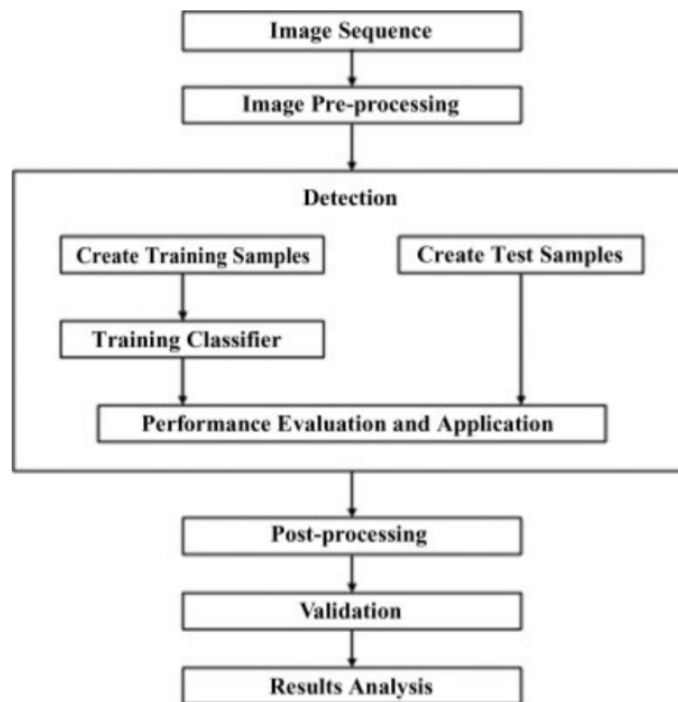
Figure 3.5: Pipeline of the learning-based detection system proposed in Jiang et al. (2007).

The machine learning method that was implemented by the authors was first developed by Viola and Jones (Viola and Jones (2001)) and perfected for human face detection. The method appeared efficient for detecting faces with different sizes, and, for being size-invariant, it is highly

useful for tracking Clathrin particles of different sizes. However, a particle representation class has a considerably smaller variability than the class of human faces, which needs thousands of instances of objects to describe the difference between face and non-face objects. It appears much simpler to detect a particle than a face: particles are circular spots that are slightly lighter than their background. However, their small size hinders the application of features such as textures and contours, and the particles can be easily mistaken by noise, and vice versa, which is aggravated because fluorescence microscopy images tend to exhibit a low SNR.

As said, this classifier uses Haar features. Each of these features is a single value obtained from an image region, defined by applying a binary filter analogous to those represented by the black and white rectangles of Figure 3.6
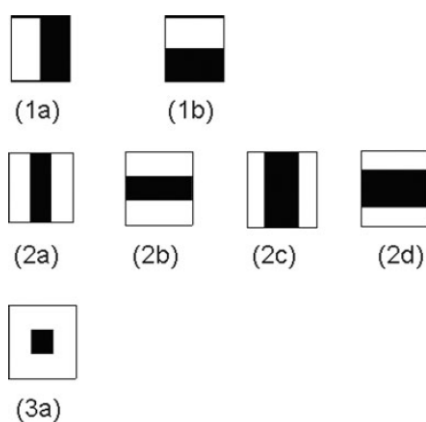
Figure 3.6: Feature prototypes of Haar-like and center-surround features. 1a) and 1b) are used to calculate edge points, 2a) to 2d) are line features and 3a) is a center-surround feature. Adapted from Jiang et al. (2007).

These kernels are used in many sizes and in all possible locations in the image, calculating a great amount of features, resulting in a high computational cost. Among all the calculated features, most of them are actually irrelevant, for example if we consider the edge features on flat background areas. The Adaboost algorithm helps the selection of a small number of critical visual features, making this classifier more cost-effective, by selecting the features that give rise to the minimum error rate in further classification. Even though the number of features is severely decreased in this step, the efficiency can still be improved by building a cascade of classifiers. The features are grouped into different classifiers, which are consecutively applied in different stages. The performance of these weak classifiers is evaluated so that a final strong classifier consisting of the better performing weak ones is constructed.

To improve the detection process, the authors use Canny edge detector to reject the image regions with an abnormally great or small density of edges.

For further accurate linking, post-processing of the detected regions is done, extracting appearance information of particles, such as boundary and area. In the whole image, it was seen that methods such as watershed segmentation were worthless, but since the areas in which this method

is applied can now be limited to the ones in which the classification routine found a particle, post-processing can made significantly simpler. The post-processing implemented by the authors was the extraction of intensity and texture features from each rectangular region with a detected particle, followed by multi-class classification of these regions. Three classes were identified: regions with high intensity and contrast, regions with high intensity and low contrast and regions with low intensity, which are not considered in the experiment. For these classes, Fuzzy c-means is used to partition the rectangle pixels into additional classes, being the object of interest present into one of these classes. The result of the application of this pipeline is presented in Figure 3.7.
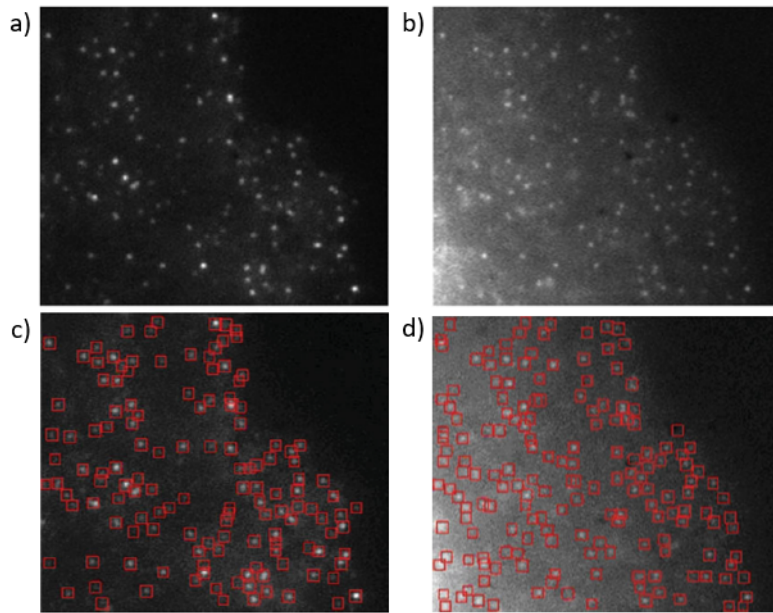
Figure 3.7: Examples of images analyzed in Jiang et al. (2007) (a and b) and the results of the applied detection and enhancement pipeline (c and d correspond, respectively, to the processing of a and b).

3.1.2 Cell detection in phase-contrast microscopy images

Phase-contrast microscopy is an optical microscopy technique that uses the phase shifts of the light that passes through a transparent specimen to model the brightness of an image. It is used to image living cells in many applications. The authors of Kang Li et al. (2006) proposed an online methodology for tracking migrating and proliferating cells that are imaged through this technique, which involves a detection phase. This method is based on the fact that cells appear as dark regions surrounded by brighter halo artifacts in phase-contrast microscopy, if they are not mitotic or apoptotic, in which cases they appear smaller, rounder and brighter.

In Kang Li et al. (2006), a classifier that is based on the maximum *a posteriori principle* is used. The classifier uses histogram properties of the cells (foreground) and background, knowing, for example, that histograms of non-mitotic non-apoptotic cells have more fluctuations across

different frames or dataset than living cells. Starting from histograms that are pre-trained with a small amount of data, which are h_C^0 and h_B^0, respectively for cells and background, the histograms for each frame, k, are updated using an auto-regression, present in equation 3.4, in which c stands for the cell or background class.

$$h_c^k = (1 - \alpha)h_c^{k-1} + \alpha\hat{h}_c^k, c \in \{C, B\}, 0 \leq \alpha \leq 1 \tag{3.4}$$

Histograms $\hat{h}_c^k$ are built through rough segmentation of the cells in each frame using Otsu thresholding and background subtraction. Then, assuming that the background is piece-wise linear, the background is estimated through a "rolling-ball" algorithm, that fills the holes that match the size of a ball that is "rolling" over the image.

The maximum *a posteriori* principle states that the cell map is such that maximizes the probability of a pixel belonging to the cell or background class, knowing the intensity of such pixel. Given the previously derived histogram, this principle, that underlines the classifier, can be implemented as stated in equation 3.5.

$$c_{MAP}(x) = \begin{cases} C, & \text{if } h_C(I(x)) \leq h_B(I(x)) \\ B, & \text{otherwise} \end{cases} \tag{3.5}$$

3.1.3 Particle detection in optical microscopy images - Centroid Technique

The pioneer works in the field of microrheology through particle tracking were done by John C. Crocker and David G. Grier, and are presented in Crocker and Grier (1996). Even though they were published in the year of 1996, they still concern the methods of current use, namely by researchers that work with the IDL software (Exelis Visual Information Solutions, Boulder, Colorado), for microrheology problems computation. A recent implementation of Crocker and Grier's algorithms, together with many improvements and updates is done in the Python (Python Software Foundation, https://www.python.org/) library TrackPy (Allan (2014), Allan et al. (2018)). These techniques have not only been used in the fields of colloid science and microrheology, but also biophysics, and, more recently, drug and gene delivery (Schuster et al. (2015)).

The researchers John Crocker and David Grier (Crocker and Grier (1996)) performed colloidal studies using a conventional light microscope with a 100 x N.A. 1.2 oil immersion objective. Back in the day, standard video cameras produced 30 images per second, with a typical usable portion of 480 horizontal lines of 640 pixels. Color mode was not used due to superior noise and great sensitivity to light variations in comparison to monochrome cameras. Moreover, the conversion of the frames to a digital format was confined to a 8 bit resolution.

The Crocker and Grier (1996) authors start the particle detection process by correcting imperfections in the individual images by image restoration. The imperfections they address are geometric distortion, nonuniform contrast and noise introduced by the microscope's optics and digitization stages. Long wavelength contrast variations due to uneven illumination are eliminated through a boxcar average over an extent $2w + 1$, where w is an integer larger than a sphere's

apparent radius in pixel, but smaller than the inter-sphere separation. Digitization noise can be suppressed by convolving the image with a Gaussian surface of revolution (the surface in Euclidean space created by rotating the Gaussian function around its mean). Both mentioned filters (boxcar and Gaussian) can be put together as spatial bandpass filter that removes features either with small-scale variation (camera noise) or large-scale variation (uneven lighting), both erasing objects much larger or much smaller than the particles of interest. In Figure 3.8, (Schuster et al. (2015)) one can see the result of applying this filtering step in diminishing background noise and autofluorescence in a sputum (mucus) Cystic Fibrosis respiratory culture, keeping only the brightly fluorescent nanoparticles. Even though this algorithm was developed to deal with optical microscopy images, it is proven that it does work for other types of imaging modalities (Schuster et al. (2015)).
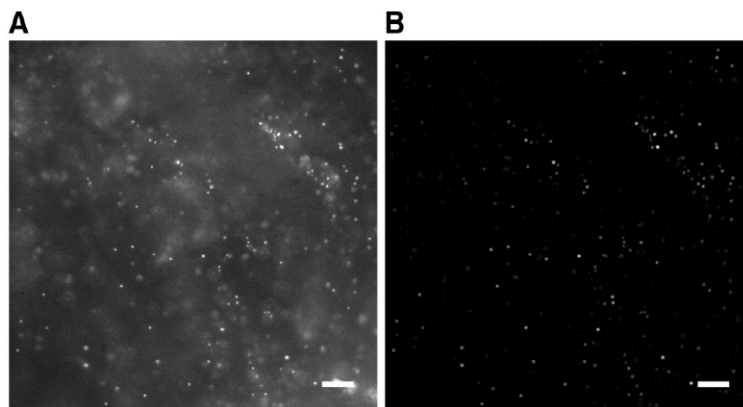
Figure 3.8: A shows the fluorescent microscopy image of 100 nm yellow-green fluorescent polystyrene particles in a Cystic Fibrosis sputum sample before processing with the bandpass filter proposed in Crocker and Grier's work. B shows the result of such pre-processing. Scale bars represent 10 μm. Adapted from Schuster et al. (2015).

After denoising, the authors identify the candidate particles through local brightness maxima. A pixel is adopted as particle candidate if no other pixel within a distance *w*, which is estimated as closest greater odd integer to the particle radius, is brighter. This means that, if a maximum is found within a distance smaller than particle diameter from another local maximum, only the brightest one is retained. Then, they require that a pixel stands in the upper 30th percentile of brightness of the entire image for it to actually correspond to a candidate particle location. The maximum selection criterion is implemented through gray-scale dilation. A pixel in the original image that has the same value in the dilated one is selected. It is possible to refine location estimates, reducing the standard deviation of the position measurement to less than 1/10 pixel, by weighting the actual centroid of a sphere through its brightness distribution, and not only its shape. This way, the centroid of a particle is given by the average position of the pixels in the spot, weighted by brightness. This method of centroid refinement is detailed in Equation 3.6, in which (E_x, E_y) is the offset to the brightest pixel (x, y) that creates the exact centroid position, and *w* the closest greater odd integer to the particle radius. *A* is the pixel intensity. In this Equation,

$m_0 = \sum\limits_{i^2+j^2 \leq \omega^2} A(x+i, y+j)$, is the integrated brightness around (x,y). These calculations are analogous to the computation of a center of mass.

$$(E_x, E_y) = \frac{1}{m_0} \sum_{i^2+j^2 \leq \omega^2} (i,j)A(x+i, y+j) \tag{3.6}$$

By calculating the moments of each sphere image's brightness distribution, the authors could separate the true particles of interest and the noise spots that resembled particles, passing through the previous detection stages unsuspected. Clustering the calculated moments and performing statistical cluster analysis over the two moments' plane, one can separate particles and noise. Another way to put this is that Crocker and Grier's algorithm characterizes each spot by total brightness, size and eccentricity, and, since true particles appear bright and circular, false positives can be discarded.

The authors of Sbalzarini and Koumoutsakos (2005) implement, as a starting point, Crocker and Grier's detection algorithm for a project that involved tracking viruses on the plasma membrane, through fluorescence microscopy. Small changes in the base method were done by these authors, such as having each particle candidate "carry" a two-dimensional Gaussian that is based on the moments that were calculated during point location refinement. A score for each particle can be given by the combination of particle *Gaussians*, and the user is invited to define a threshold for this score, which defines "true" particles.

3.1.4 Detection independent of imaging modality - Radial Symmetry Method

Raghuveer Parthasarathy introduces, in Parthasarathy (2012), a method for sub-pixel localization of imaged objects that is based on analytic, non-iterative calculation of the best-fit radial symmetry center. This algorithm aimed to respond to the inaccuracies introduced by Gaussian fitting methods, which are widely spread and used. The radial symmetry method was, then, developed to fill the gap for a particle detection method that is more accurate than Gaussian fitting (except for Gaussian fitting implemented through nonlinear least squares minimization, which was proven to perform equally well, in the Parthasarathy (2012) studies), that is fast (about 100 times faster than the Gaussian method), and does not assume any model of particle intensity distribution, which is the main problem of the Gaussian fitting method.

This technique assumes that the intensity of an imaged particle is radially symmetric about its center, and determines the point where this radial symmetry is maximum. In fact, for a radially symmetric intensity distribution inside a particle image, a line that goes through any point drawn parallel to the gradient at that point will intersect the particle's center (the distance between the center and any such line is 0). The center can, even in a noisy pixelated image, be estimated as the point that minimizes the total distance between all the drawn lines, for each particle pixel.

The author tried the technique and confirmed its applicability in several sets of experimental image data, either from fluorescence microscopy, confocal microscopy, of fluorescent proteins,

nanoparticles or micron-scale colloids, including super-resolution microscopy images. It was verified that the algorithm worked, not only for radially symmetric particles, but also for images consisting of concentric rings. As for asymmetric particles with a wide range of SNR values, this method performed with a similar accuracy to that of Gaussian fitting. An illustration of particle detection based on radial symmetry can be found in Figure 3.9.
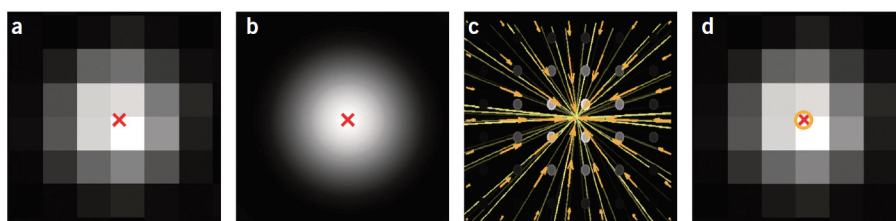
Figure 3.9: *a* is a simulated CCD image of a point source with shot noise generated from a noise-free simulated image, *b*. In these, *X* indicates the true center. In *c*, one can see the gradient of intensity, represented by orange arrows, that is calculated from the image *a*, at the midpoints between pixel centers, indicated by the circles. The yellow lines are drawn through each midpoint, parallel to the gradient. *d* shows, through an orange circle, the center estimation through the point of minimal distance to the yellow lines. Adapted from Parthasarathy (2012).

This method leaves a gap of research opened for the future, for considering other types of symmetries, such as bilateral symmetry of rod-like bacteria or ellipsoidal microparticles.

3.1.5   Discussion

In this section, many detection methods were presented. Some of them were developed to be application-specific, such as the ones that aimed for particle detection in fluorescent images. These rely on the Gaussian approximation to the Point Spread Function, which is, in these cases, specific for the fluorescence microscopy case, but can be adapted to other imaging types. The main disadvantage of these methods is their overfitting to a certain kind of particles, which impairs their application to robust, more global pipelines.

Non-fitting methods were also described, such as the simple Top-Hat filtering for particle detection, that, alone, does not allow for a very effective particle location. The truth is that most of the methods are combined with other image analysis techniques, such as thresholding, connected components labeling, and means of false positives rejection, such as analysis of ellipticity, total intensity, contrast, and pixel count of detections. It was seen that a way to increase robustness of detection methods is to implement a multiscale variant, such as wavelet representations, that can use several types of detection kernels. Also, for separating overlapping spots, one can consider approaches that include sets of shifted functions in mixture models.

More complex non-fitting methods are the detailed Centroid Technique and Radial Symmetry method. Even though the Centroid Technique is still in use by the great majority of works in the microrheology field, Radial Symmetry performance tests done in Parthasarathy (2012) create

some curiosity about the results of the latter in problems in which the Centroid Technique is usually applied.

Detection through a cascade learning algorithm was also detailed, but its application is dependent on the creation of a training dataset, and the diversity of this dataset will dictate the performance of the detection method. Simpler classification routines, such as the one outlined for cell detection in phase-contrast microscopy could also be easily adapted not to depend on the imaging method.

For objectively comparing the performance of the detection methods, Smal et al. (2009) presents a comparative study that uses synthetic data (using 2D Gaussian Intensity Profiles (GIPs) to model particles) with Poisson noise with SNR =2 (in real live-cell fluorescence image data, a SNR of 4 is the critical boundary). The simulated images were of size 512x512 pixels and contained 256 particles each. Examples of three image types are present in Figure 3.11. This comparative study reflects the performance of the following techniques: Wavelet Multiscale Products (WMP) (Olivo-Marin (2002)), Top-Hat filter (TH) (Chenouard (2010),Olivo-Marin (2002)), Spot-Enhancing Filter (SEF) (Godinez et al. (2009),Daniel Sage and Unser (2005)), Morphological grayscale opening Top-Hat filter (MTH) (Chenouard (2010)) and the supervised Adaboost algorithm (AB) (Jiang et al. (2007)). The results of the methods comparison are present in Figure 3.10. These results are given in terms of True Positive Rate (TPR*), the fraction between the number of true positives and the sum of true positives and false negatives. The false negatives are given by the subtraction between the total number of objects on the ground truth and the number of true positives. This comparison is done at the level of False Positive Rate, FPR*=0.01. The False Positive Rate is given by the fraction between the number of false positives and the sum of the true positives and false negatives. From this comparison study, one can conclude that the learning approach, Adaboost, outperforms all the other methods in every case, and that the Top-Hat filter's performance drops when the background ceases to be uniform. The wavelet approach is the one that provides the most limited results.

Moreover, for comparison between Gaussian fitting approaches, the Centroid Technique and the Radial Symmetry method, Parthasarathy (2012) subjects the three methods to a scenario with simulated particle images spanning a range of SNR from 3.5 (100 photons detected) to 150 (200,000 photons detected). This comparison is plotted in Figure 3.12. Through its analysis, one can concluded that, for the types of images being used for testing, the Radial Symmetry method outperforms the Centroid Technique and the Gaussian fitting approach through maximum likelihood estimation. Even though its sub-pixel accuracy is similar to that of Gaussian fitting, and the performances of this symmetry method and Gaussian fitting, through nonlinear least squares minimization, follow each other throughout the SNR spectrum, Parthasarathy (2012) states that the Radial Symmetry method's execution is roughly 100 times faster.
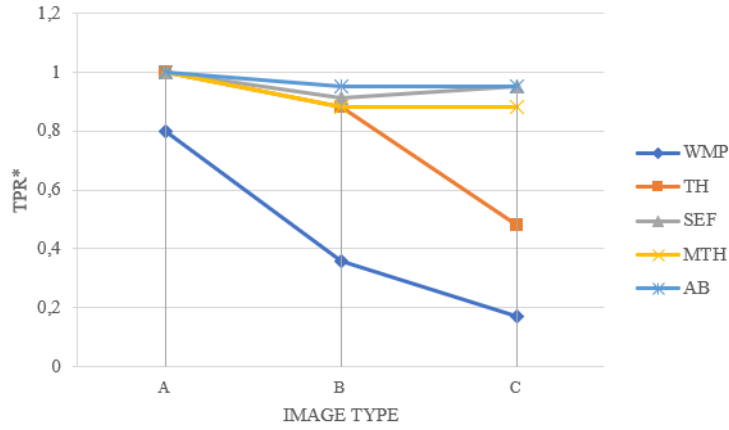
Figure 3.10: Results of the comparative study of Smal et al. (2009). On the x axis, the image types, exemplified in Figure 3.11, and, on the y axis, the True Positive Rate for some methods included in the study: wavelet multiscale products (WMP) (Olivo-Marin (2002)), Top-Hat filter (TH) (Chenouard (2010),Olivo-Marin (2002)), spot-enhancing filter (SEF) (Godinez et al. (2009),Daniel Sage and Unser (2005)), morphological grayscale opening top-hat filter (MTH) (Chenouard (2010)) and the supervised Adaboost algorithm (AB) (Jiang et al. (2007)).

3.2 Particle Linking

After particle detection, when following a two-step approach, comes the task of linking particles to form tracks, and even linking tracks to assure their completion. A track of particles can be seen as a succession of detections through time, being formed by one particle in each frame. Considering z_i^k the ith track, composed of a set of k detections from time 1 to time k, each individual track can be represented by Equation 3.7 (Chenouard (2010)).

$$z_i^k = \{z_i(1), z_i(2)...z_i(k)\} \tag{3.7}$$

Being $Z(k)$ the set of detections in frame k, Z^l is the set of particle detections in the whole frame sequence, represented by Equation 3.8 (Chenouard (2010)).

$$Z^l = \cup_{k=1...l} Z(k) \tag{3.8}$$

For the linking problem, simple Nearest Neighbor algorithms may be used, ideally followed by techniques for tackling the problems associated with particle tracking in microscopy images (Chenouard et al. (2014)). Probabilistic approaches can also be used for the completion of the linking task. These arose from the idea of exploring the statistical models of particle movement, such as Brownian movement, so as to track particles in a more "natural" way.

The application of the Bayesian framework, in which a track is modeled as a stochastic sequence of noisy measurements, can be made. Estimation techniques based on this framework can be used to extend tracks iteratively with the most probable detection, or to build a probability density function of target positions, to deduce tracks from (Chenouard (2010)). Examples of methods
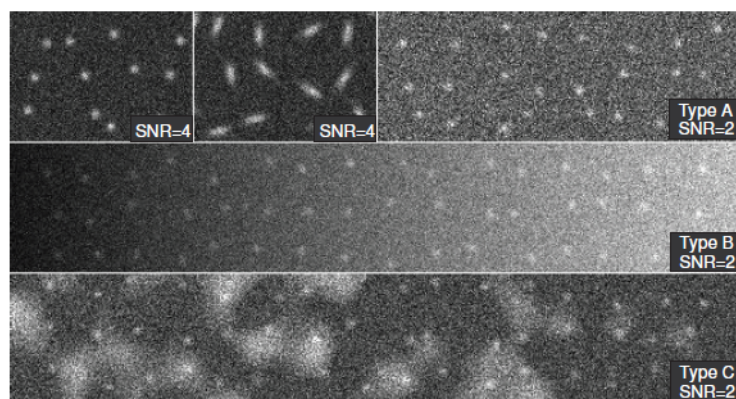
Figure 3.11: Examples of the synthetic images used in the comparative study of Smal et al. (2009). The symmetrical GIPs of Type A, B, and C, are embedded into, respectively, uniform, gradient, and non-uniform backgrounds.

based on Bayesian frameworks are Kalman filters or Particle filters, state-state approaches that require the identification of a model for the evolution of the state with time and a model for the measurements that are related to the state. In this case, the state of a particle can be composed of information related to its kinematic properties. As these methods would require the definition of many parameters associated to the motion model of the particles, and the unpredictability of their movement would not be correctly characterized, this work will focus on the previously mentioned Nearest Neighbor methods, instead.

3.2.1 Nearest Neighbor linking algorithms

When one can assume that the detection phase was performed perfectly and that the frame acquisition rate was high enough to capture small movements of particles, from one frame to another, it is likely that there will be a detected particle very close to one detected in the previous frame, for every frame. Therefore, each track can be extended by looking for the particle detected closest to the previous one, in the previous frame, or in an already formed track. This can be done with the minimal Euclidean distance between $z_{t_i}(k)$, the track that is being formed, and $Z(k+1)$, the set of particle detections in the next frame. This is the basis of Nearest Neighbor (NN) linking, a point correspondence method, by which linking is done finding correspondences between subsequent sets of detections (Chenouard (2010)). "Nearest", in this context, may refer, not only to spatial distance, but also to difference in intensity, volume, orientation, and other features that may be acquired (Meijering et al. (2012)).

There are many ways to perform Nearest Neighbor search in the feature space. The most straight forward one is K Nearest Neighbors (kNN). This calculates the distances between a certain point and every other point, in a way to sort the latter, returning the closest K items, being K user-defined. This method is simple, but too slow when the number of points increases from hundreds to millions (Agafonkin (2017)), since it has to repeat distance calculations for each considered
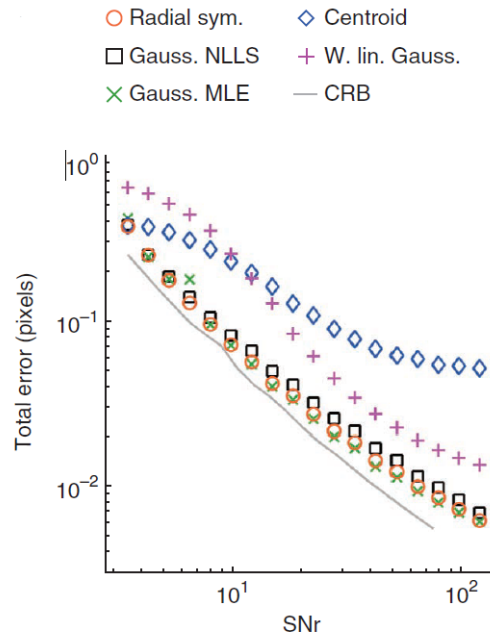
Figure 3.12: Localization error for detection in simulated particle images with a range of SNR from 3.5 to 150 (16-bit precision). Each point is given by 1000 tests at each SNR. Radial sym. is the Radial Symmetry method, Centroid is the Centroid Technique, Gauss. NLSS and Gauss. MLE are, respectively, Gaussian fitting performed with nonlinear least-squares minimization and maximum likelihood estimation. The solid line indicates the Cramér-Rao bound (CRB) on localization accuracy (the lower bound on the variance of unbiased estimators of localization). W. lin. Gauss is the weighted linearized Gaussian fitting. Adapted from Parthasarathy (2012).

feature point. To increase the speed of this process, pre-processing of the data can be done, such as organizing it in tree structures.

Trees are undirected, connected and acyclic graphs that define the relation between nodes, or leaves, through edges that connect them (Pfenning et al.). Through these, it is much easier to find the approximate neighborhood of any point than with the simple kNN case (Harnal (2015)). This method, however, has the drawback of needing tree reconstruction every time a new element is added, since this addition can change the median values (used to split tree nodes into children), which is not efficient (Lichtman (2018)). Despite this, trees were developed to optimize disk data storage and effectiveness of reading (Foster (2012)). Each node may have more than one key value, since one needs to make a *n-way* decision, where *n* is the total number of children the node has (Rajinikanth (2019)). Taking this into account, given a node to start from, a simple linear or binary search is used to find the node correspondence. This method is widely used for large datasets, since it minimizes the number of disk seeks by grouping data efficiently (Lichtman (2018)).

Many problems may arise when considering the implementation of NN linking approaches for the tracking of particles in the context of microrheology. For example, applying a model fitting or template matching in a single frame and using the found positions as an input for the NN

algorithm, initializing the detection in the next frame, can implicitly solve the linking problem (Meijering et al. (2012)), but lead to errors right away. These happen when one is working with a dataset in which the Nearest Neighbor of a particle, in the following frame, is a detection of a different particle. This is usually due to fast particle motion, compared to acquisition rate. Moreover, if there are false detections that one must account for, or missing ones, the number of targets is unknown, and the assignment of detections to tracks is greatly prone to error (Chenouard (2010)). Due to this and other factors, one must work around the problem of wrongly formed tracks, either by tackling the issue of a varying number of particles per frame, or their fast and directed motion, or their disappearance and reappearance, or even their merging and splitting. There are many techniques which enable NN algorithms to work around these problems.

Furthermore, not including intrinsic models regarding the particle motion can be an advantage on biology studies that aim to characterize this same motion model. This appears as a disadvantage when considering other applications, that could benefit from the inclusion of knowledge of the movement's underlying physical principles, such as the statistic of random walks, for particles undergoing Brownian motion. Because microrheology studies involve the tracking of particles which are ideally moving in a purely Brownian way, incorporating some knowledge about this motion type features could be useful for the linking methodologies. However, this awareness about the motion model should not highly constrain the linking procedure, since the particles can undergo other types of movement, such as collective drift, which can be unintentionally induced during microscopy imaging procedures, and should be correctly identified, in order to enable its successful removal.

3.2.1.1   Working around the varying number of targets

Local and global NN come to try to adapt NN linking to tracking a varying number of targets. While local NN builds all the possible associations between active tracks and the set of detections in the next frame, ending non-associated tracks and keeping only the feasible ones, global NN looks for the set of associations between tracks and detections, in the next frame, that compose the smallest sum of distances. The latter is a time consuming but better approach than local NN. The rule of association gating comes to reduce computation time, limiting linking to associations within a distance below a threshold. Moreover, tracks formed by a single detection are discarded (Chenouard (2010)).

Sbalzarini and Koumoutsakos (2005) introduces a linking technique that deals with missing particles and introduces pixel intensity features in the NN cost function, for greater linking accuracy. This method represents particle tracks as association matrices between detection sets. Each pair of frames (or set of frames between which tracks are defined) is, then, represented as a matrix that contains, as rows, the particles found in one of the frames, and as columns, the particles found in the other. For every pair of detection sets (Sbalzarini and Koumoutsakos (2005) uses Crocker and Grier's method as a feature point detection technique), the numbers 0 or 1 are added to the association matrix, respectively, if the detections are produced by the same physical particle or

not. Therefore, every row and every column must contain exactly one entry of value 1, and the remaining should be 0, so that the detections are not done between more than two particles between frames. The user can set the number of frames to be accounted for in the definition of this matrix, depending on how long the trajectories are supposed to be. "Virtual" particles, meaning, the missing detections that are noticed in the assignment process, are added as an extra row and column to this association matrix. The occlusion of a particle is reflected in the linking of a particle detection to a virtual detection, and a particle reappearance leads to linking a virtual detection to a particle detection (Chenouard (2010)).

Sbalzarini and Koumoutsakos (2005) uses a cost function (Equation 3.9) (cost of associating the detection $z_i(k)$ to the detection $z_j(k+r)$), that is a modification of the simple Euclidean distance. This accounts for previous associations and for the difference of intensity moments of order 0 (m_0) and of order 2 (m_2), between subsequent detections. In Equation 3.10, $r = 1, ..., R$, with R being the number of frames that are accounted for, and i, j the indexes of the association matrix (Chenouard (2010)). The connection of particles to "virtual" ones gets assigned a different cost, which is the maximum allowed cost. This cost is calculated with a user-specified rule of association gating, which represents the maximum distance a point is allowed to travel between subsequent frames, having its intensity moments remaining constant (Sbalzarini and Koumoutsakos (2005)).

$$\phi_{ij} = ||z_i(k) - z_j(k+r)||_2^2 + \\ (m_0(z_i(k)) - m_0(z_j(k+r)))^2 + (m_2(x_i(k)) - m_2(x_j(k+r)))^2 \tag{3.9}$$

The association matrix is initialized by assigning each point, in a certain frame, its nearest neighbor, in the frame $k+r$, using ϕ_{ij} as the distance measure one needs to minimize.

The score function defined for the whole problem, which needs to be minimized, is present in Equation 3.10. In this equation, m_k and m_{k+r} are the number of detections at time k and $k+r$, and g_{ij} is the association matrix entry for the respective indexes (Chenouard (2010)).

$$\Phi = \sum_{i=0}^{m_k} \sum_{j=0}^{m_{k+r}} \phi_{ij} g_{ij} \tag{3.10}$$

This method is, however, scale-dependent, since the terms of Φ are mixed in a scale-dependent way. Different intensity normalization processes and different acquisition device settings lead to different tracking scores, given that the scale of intensity values is altered (Chenouard (2010)).

Jaqaman et al. (2008) introduces another technique for overcoming a number of particles that varies from frame to frame, to be used in live-cell image sequences, named partial tracks linking. This method separates the linking process into two tasks. The first task is the linking of particles between frames, using an association matrix with a cost function defined as the squared Euclidean distance between detections. This step does not model target disappearance (associations are made only between subsequent frames). The second task is linking partial track segments, that were left disconnected due to particle disappearance, in the first step. This linking step aims to close gaps and to capture particle merge and split events. This task can be seen as a standard linear

assignment problem, since the score of a final set of tracks can be computed as the sum of each linking event cost, being globally easy to solve. However, linking errors propagate through steps, and the performance of the partial tracks linking method depends largely on the first task, whose output cannot be altered (Chenouard (2010)). In Figure 3.13, the pipeline of partial tracks linking can be analyzed, together with two examples of cost matrices, the first for controlling particle assignments between frames, and the second for controlling gap closing (Jaqaman et al. (2008)).
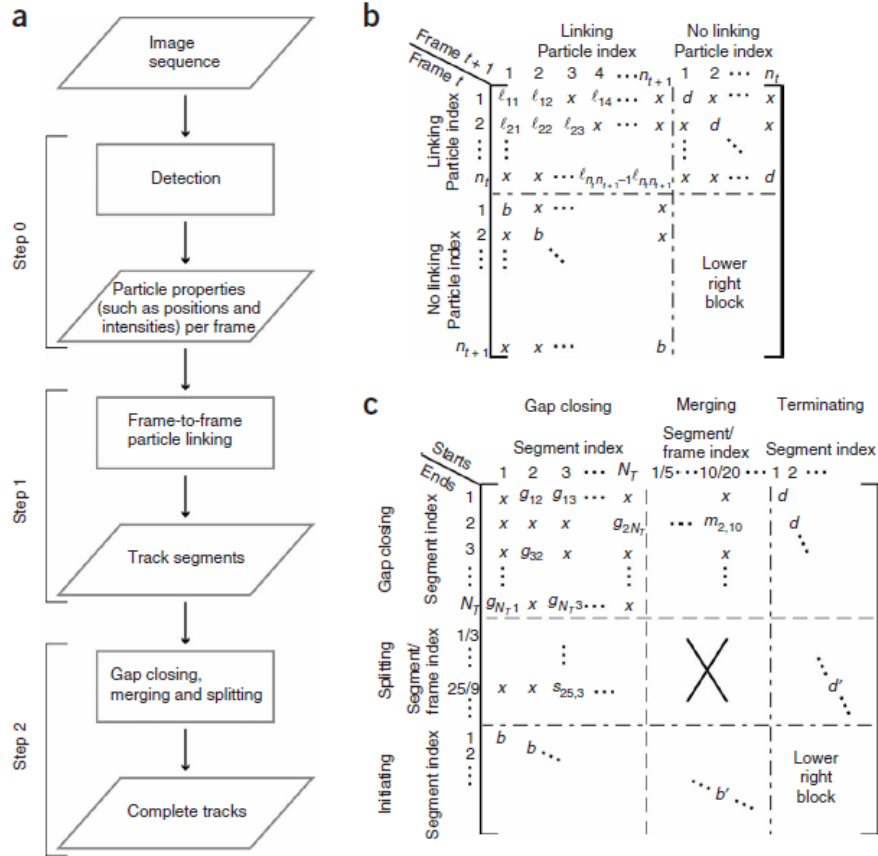
Figure 3.13: Cost matrices examples. **a** shows the pipeline of partial tracks linking algorithm. **b** displays an example of a cost matrix that controls particle assignments. In this matrix, l_{ij} corresponds to the cost of linking particle i, in frame t, to particle j, in frame $t+1$. X means that it is impossible to link the particles because the cost of it exceeds the cutoff. d is the cost of linking particles in frame t to nothing in frame $t+1$. b is the cost of allowing particles in frame $t+1$ to get linked by nothing in frame t. The lower right block is auxiliary. **c** is the cost matrix that controls gap closing, for merge and split events. In this matrix, g_{IJ} is the cost of closing a gap between the end of the segment I and the start of the segment J. s_{IJ} is the cost for splitting the track I, creating the track J from a middle point of I. Upper and middle right and lower and middle left blocks are the same as described for b. Adapted from Jaqaman et al. (2008).

Using this two-step method, false detections can be assigned without penalization, and wrong associations will easily result in incorrectly formed tracks. The costs for assigning a middle point of a track to the start of another one, in a splitting event, or linking the end of a track to the

middle of another one, in a merging event, are given arbitrary values. Some biological scenarios do not give rise to split and/or merge events, but this is not taken into account in this algorithm (Chenouard (2010)).

Crocker and Grier (1996) also try to address the varying number of targets in their linking method, which minimizes the total length of the links, using random walks statistics to optimize the trajectory formation. In this method, only the labels of particles that form paths that are shorter than a user-defined parameter (rule of association gating), L, are selected as candidates for particle assignment. This is equivalent to considering only the probability density for $\delta \leq L$, being δ the distance between two particles that are linked together. Analogously to the methods proposed by Sbalzarini and Koumoutsakos (2005), Crocker and Grier also add "missing" bonds, which are assigned the maximum length (which corresponds to the maximum cost in the considered cost function). It is relevant to highlight that particle linking is only possible through this method if the typical single particle displacement in a time step is sufficiently smaller than the typical inter-particle spacing, a, being $\delta < L < a/2$ an optimal cutoff. The algorithm provided by these investigators outputs data for an histogram of displacement at the shortest time scale. Analyzing it, one can conclude, if the histogram decays to zero as the displacement approaches the maximum, that the choice of maximum frame-to-frame particle displacement (L) was appropriate. The histogram for this behaviour can be seen in Figure 3.14 If many particles moved the established maximum displacement in the said time scale, this value should be increased. On the contrary, if few particles reach maximum displacement, this value should be decreased, increasing performance and accuracy (Schuster et al. (2015)).
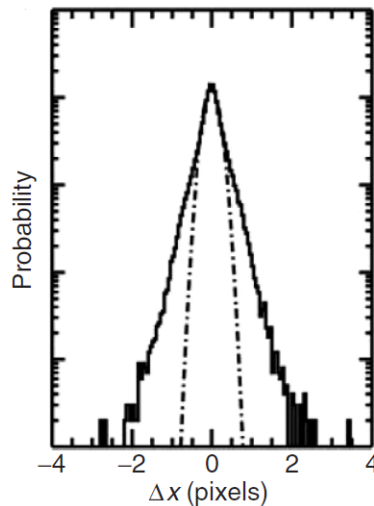

Figure 3.14: Histogram of tracer displacements between consecutive frames, which decays well before 4 pixels, the set maximum displacement. Adapted from Crocker and Hoffman (2007)

3.2.1.2 Working around fast particle motion

To deal with linking of particles with fast and directed motion, Sethi and Jain (1987) proposed a modification in the distance criterion of NN algorithms. Instead of using just the previous frame for a certain association, the two previous positions of a particle are taken into account, favoring smooth tracks. The cost function for each track, computed at time k, is presented in Equation 3.11, in which γ_1 and γ_2 correspond, respectively, to the tuning parameter for the first regularization term, which favors tracks with constant directions, and to the tuning parameter for the second term, which favors tracks with regular displacements (Chenouard (2010)).

$$
c_i(k) = \gamma_1 \left[1 - \frac{(z_{t_i}(k-1) - z_{t_i}(k-2))(z_{t_i}(k) - z_{t_i}(k-1))}{||z_{t_i}(k-1) - z_{t_i}(k-2)|| \times ||z_{t_i}(k-1) - z_{t_i}(k-2)||} \right] +
$$

$$
\gamma_2 \left[1 - 2 \frac{\sqrt{||z_{t_i}(k-1) - z_{t_i}(k-2)|| \times ||z_{t_i}(k-1) - z_{t_i}(k-2)||}}{||z_{t_i}(k-1) - z_{t_i}(k-2)|| \times ||z_{t_i}(k-1) - z_{t_i}(k-2)||} \right]
$$

(3.11)

3.2.1.3 Introducing intrinsic models regarding particle motion

Even though NN methods are usually seen as linking techniques that do not take into account the motion models of the particles, some modifications can be done in these methods which make them behave with awareness of the kinematic tendencies of the particles. For instance, in Sbalzarini and Koumoutsakos (2005), the cost function for trajectory linking (Equation 3.9) can easily be replaced by a function that suits a particle type's model of motion.

Another example of the introduction of particle motion models into linking procedures is the pioneer technique of Crocker and Grier (1996). Their linking method uses the statistic of random walks to assign particle labels form one image to the next. Detailing, one chooses the assignments that maximize the probability that the particles will diffuse a distance δ in the plane, in time τ, $P(\{\delta_i\}|\tau)$, or, equivalently, the assignments that minimize $\sum_{i=1}^{N} \delta_i^2$ (the total length of the links). Equation 3.12 describes this probability for a single Brownian particle and equation 3.13 represents the ensemble of N non-interacting identical particles, which corresponds to the product of single particle results (Crocker and Grier (1996)). The latter equation is also expressed in terms of the displacement probability from a set of positions $Z(k-1)$ to the positions $Z(k)$ (Chenouard (2010)). In both equations, D is the diffusion coefficient.

$$
P(\delta|\tau) = \frac{1}{4\pi D\tau} exp\left(-\frac{\delta^2}{4D\tau} \right)
$$

(3.12)

$$
P(\{\delta_i\}|\tau) = \left(\frac{1}{4\pi D\tau} \right)^N exp\left(-\sum_{i=1}^{N} \frac{\delta^2}{4D\tau} \right), or,
$$

$$
P(Z(k)|Z(k-1)) = \left(\frac{1}{4\pi D\tau} \right)^N exp\left(-\sum_{i=1..n} \frac{||z_i(k) - z_i(k-1)||_2^2}{4D\tau} \right)
$$

(3.13)

Taking particle detection and linking into account, Crocker and Grier's complete algorithm only requires, as parameters, the apparent particle size and the maximum frame-to-frame particle displacement (which can be estimated by the Stokes-Einstein equation). Additionally, the user can specify the number of frames in which "missing" particles are accounted as so. Simplifying the linking problem this much is only possible because this algorithm is based on the statistics of random walks, which state that a diffusing particle is most likely to be found near where it was last seen (Schuster et al. (2015)). Unlike NN methods, Crocker and Grier's linking approach, which is based on Brownian movement assumptions, uses the squared Euclidean distance, and not the simple Euclidean distance. This means that NN methods are not working with the same motion principles, and are under-penalizing unlikely movements (Chenouard (2010)).

3.2.2   Discussion

In this section, several linking algorithms of the Nearest Neighbor category were reviewed. This type of algorithm has a global scope, having room for being improved to fit the particle linking problem, for example, by addressing the linking of a varying number of particles per frame, but also for being adapted to the linking of particles with Brownian motion, since the cost function that dictates the "distance" that is minimized may be altered to comply with intrinsic models of motion. A comparative review of linking algorithms is provided in Chenouard et al. (2014), a report on the results of a 2014 particle racking competition. This document states that the key factor that distinguishes the best performing methods, in biological particle tracking, is their use of available or measured knowledge about the particle motion in each scenario. This may mean that algorithms do overfit the data they are designed for, but Chenouard et al. (2014) explains that this idea is not, as in other problems, bad. More, the use of prior knowledge, appropriate image analysis methods and parameter fine-tuning is encouraged in most biological applications.

3.3   Tracking as a global optimization problem

In opposition to methods that solve a point correspondence problem, another option is to solve the tracking problem by means of a global optimization scheme. This is not a frame-to-frame approach. On contrary, it simultaneously conducts the detection and tracking phases to exploit temporal information and trajectory smoothness (smooth curves in the spatio-temporal volume), compensating for the poor quality of the microscopy images. However, such methods are not favorable when there is a large quantity of particles that may be close or even overlap, since the presence of additional targets is not taken into account when a track is extracted. The previously defined two-step frame-to-frame approaches are introduced when multiple targets are the problem, since they impose strict competition for the detections (Chenouard (2010)).

An example of a one-step methods, dynamic programming, is now analyzed.

3.3.1 Dynamic programming

Dynamic programming analyzes the whole spatio-temporal dataset, extracting effectively a trajectory in an image sequence affected by noise. This technique works with all the frames of a sequence, both past and future ones. Therefore, this is an offline method (Daniel Sage and Unser (2005)). For fluorescence microscopy, it implements three stages. The first is sequence alignment, in which there is compensation for the sample movement, segmentation of the background structures and their further alignment. This step is introduced because the reference of position calculation in further steps does not necessarily stay still during the whole acquisition. The second stage is spot enhancing, in which filtering methods for particle enhancement and background reduction are applied. The third stage is the construction of the optimal space-time particle trajectory (x,y,z,t), from the first to the last frame. This trajectory is built through optimal path finding, and not by an explicit, frame-by-frame detection method and further linking (Chenouard (2010)).

The first step of this algorithm, for alignment of the image sequence, can be done selecting one image of the sequence and considering it as a reference frame. This image is, then, used to register the other ones. This approach is applied when the shape of the reference structure is conserved throughout the video. If this condition does not apply, but the shape of this structure can be described by a curve within a parametric family, the reference can be tracked and realigned through the application of a detector that can extract such curves, aligning also the whole image. The particle enhancing stage uses the previously described spot-enhancing filter. For finding the optimal time trajectory that describes the particle displacement, the user specifies parameters that constrain the maximum possible excursion from one frame to another. The optimal trajectories are, then, the ones that maximize a cost function, which is designed to incorporate as much problem-specific information as possible. The cost function is described in Equation 3.14. In this, M and λ, are, respectively, a normalization factor and a smoothness-controlling weight, adjusted by the user. Also, $f(x_t,t)$ is the intensity of particles in a pre-processed image. This cost function is maximized because high intensity positions (with high response to the spot-enhancing filter) and short excursions, $||x_t - x_{t-1}||$, are to be favored (large displacements from frame-to-frame are penalized) (Daniel Sage and Unser (2005)).

$$\xi(x_0, x_1, ..., x_{N-1}) = \sum_{t=1}^{N-1} (1 - \lambda) f(x_t, t) - \lambda \frac{||x_t - x_{t-1}||}{M} \qquad (3.14)$$

Dynamic programming comes, in this context, to compute efficiently the cost function, by applying an iterative update formula that reaches a maximal cost required to get to the current state. When this algorithm reaches the last frame, the state with the highest score is selected and the complete trajectory is built trough back-tracking (Daniel Sage and Unser (2005)).

This approach does not deal with appearance and disappearance of particles, which restricts highly the application field. Moreover, it can be used for tracking multiple particles, if one instance of the cost function is applied to each particle trajectory, but only if the particles are widely apart. Because handling multiple targets could result in ambiguity of the linking process, the implementation of this algorithm could produce a massive number of possible combinations of tracks, which

would increase the cost of the dynamic programming technique, removing the advantage it had over other, more computationally expensive methods. Also, because this method assumes small displacements, the Euclidean distance criterion can be adequate. In the situation of particles with fast movement compared to the acquisition rate, such criterion could not be applied (Daniel Sage and Unser (2005)). The algorithm proposed in Daniel Sage and Unser (2005) is already implemented as a plugin, SpotTracker, for ImageJ (Rueden et al. (2017)), a public-domain software package for image processing.

3.4 Summary

There are many options, either for particle detection and linking, or other tracking approaches, and this review served the purpose of acknowledging their existence, for further exploring if they can or not fit the microrheology problem. The final goal of this work is to create a set of efficient methods for particle tracking in microrheology, and to make their utilization straightforward for researchers. However, not every tracking method is suitable for microrheology studies. It is known that the particles being studied have Brownian motion, which can only be captured if the tracking method is highly precise in its detection phase, such that no particle is left undetected in any frame, and makes no assumptions about a type of movement other than the Brownian one. Moreover, if a slow oriented motion of the particles together with the background is observed, one must keep in mind that the most likely cause of this observation is the drift of the system, and not the Brownian motion of the particles. Therefore, drift correction should be applied in these cases, and one must proceed carefully if using a tracking method that incorporates intrinsic models of Brownian motion.

It is also known that, since microscopy videos are the raw data in particle tracking experiments, these should be collected with the highest possible quality, aiming to display highly contrasting particles against a very uniform background. Because conditions may differ from the ideal ones, such as through inhomogeneity of the fluid (and other optical properties of the specimen), the detection algorithms need to be adapted to these difficulties, that are beyond the researcher's control. Custom built instrumentation for particle tracking microscopy is not necessary, which is a great advantage for researchers interested in the technique, but it requires extra care when designing the tracking methodologies, since these need to adapt to the resolution and light conditions. Besides, the placement of the particles in the sample needs to be pondered, since a small inter-particle spacing leads to difficulties of construction of individual trajectories. Also, the concentration of particles in the sample should be kept low such that the interactions between particles are irrelevant compared to thermal forces. Detecting beforehand the occurrence of particle aggregates is a feature that should be implemented for improving overall results.

To conclude, it is important to highlight that most microrheology studies, and also studies in the area of colloid sciences, biophysics and drug and gene delivery, have been conducted using Crocker and Grier's algorithms (Crocker and Grier (1996)), since their procedure is grounded on the statistics of random walks, coherent with Brownian diffusion. However, the introduction of

new and complementary methods is advantageous for bridging its gaps and creating innovative approaches for microrheology studies.

Chapter 4

Particle Tracking

This chapter aims to detail the considered attempts for finding the particle detection scheme that better fits the needs of microrheology studies. The three methods addressing microrheology studies that were more frequently cited in the literature were tried out, and their performance and specifications finally led to the approach that is proposed in this dissertation - a combination of two of the proposed methods, as can be seen in Figure 4.1.
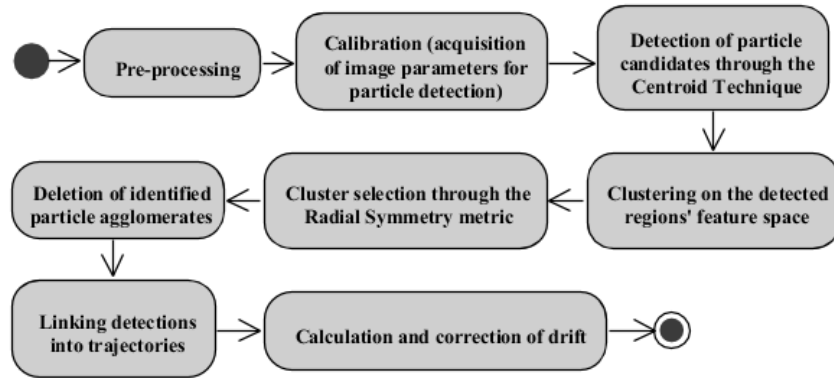
Figure 4.1: Simplified activity diagram of the particle tracking pipeline

4.1 Preliminary particle tracking attempts

The first particle tracking tests were done with images of real blood (Figure 4.2), in which sixty 2.8 μm Carboxylic Acid monodisperse beads move freely. The field of view corresponds to a particle volume fraction around $\phi \approx 10^{-3}$. A pre-processing routine was applied to each image, consisting of the Bilateral Filter (Bradski (2000)), for reducing background noise and smoothing the image, preserving the edges of the particles, and a Gamma correction, for enhancing the particles' contrast.

This pre-processing is highly computationally intensive, mainly due to the application of the Bilateral Filter, which adds up to 0.05 seconds of processing time, per image, to the gamma correction computation time, of 0.01 seconds (tests conducted in the images presented in Figure 4.2).

4.1.1 Bilateral Filter

The Bilateral Filter uses the weighed average of the neighborhood pixels to give a new value to each image pixel. The weight of the average function can be based on a Gaussian function. For this filter to preserve edges, it must not only weight the neighborhood pixels according to their Euclidean distance to the center, but also according to differences in color intensity. The parameters that need to be set on this filter's function are the controls of how distant in the color or coordinate space can the pixels that are going to be averaged together be. Averaging distant colors means creating larger regions of semi-equal color, and averaging distant pixels means that widely separated separated pixels will have influence on each others' values. Thus, to smooth the background as much as possible, it was considered, in this step, that distant pixels could have a significant influence on each other. The result of applying the Bilateral Filter to the detailed experimental image can be seen in Figure 4.2 (b).

4.1.2 Gamma Correction

On the other hand, the Gamma correction, known as the Power Law Transform, starts by taking the pixel values, I, (scaled from 0 to 1) and transforms them according to the following equation: $O = I^{1/G}$. In this equation, O is the output pixel and G is the gamma value. Gamma values smaller than 1 shift the image towards the darker end of the spectrum and gamma values superior to 1 enhance its lighter region (Rosebrock (2015)). In this case, a gamma value of 2 was used to shift the spectrum to brighter values, and the result of this correction is shown in Figure 4.2 (c). In this figure, one can see the particles being clearly highlighted from the background.
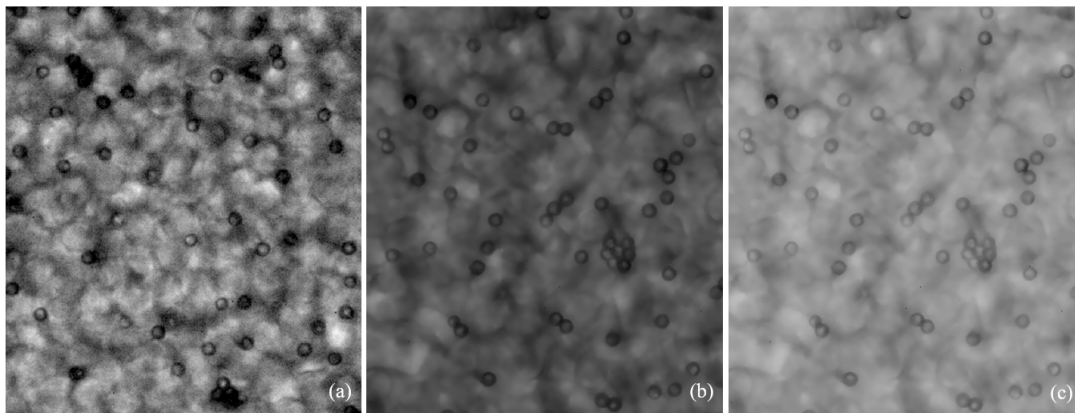

Figure 4.2: Example of application of a pre-processing routine composed of Bilateral filtering (b) and Gamma correction (c) to experimental data (a).

After the pre-processing routine, the bandpass filter used in the Centroid Technique (Crocker and Grier (1996), Crocker et al. (2000), Crocker and Hoffman (2007)) is applied. The output of this bandpass filter is highly improved by the pre-processing routine previously described, as can be seen in Figure 4.3. After bandpass filtering the image, morphological operators (opening and closing with kernels adapted to the size of the white regions and to the shape of the circular regions that should be kept, respectively) are applied, to connect big components and delete spurious white points.
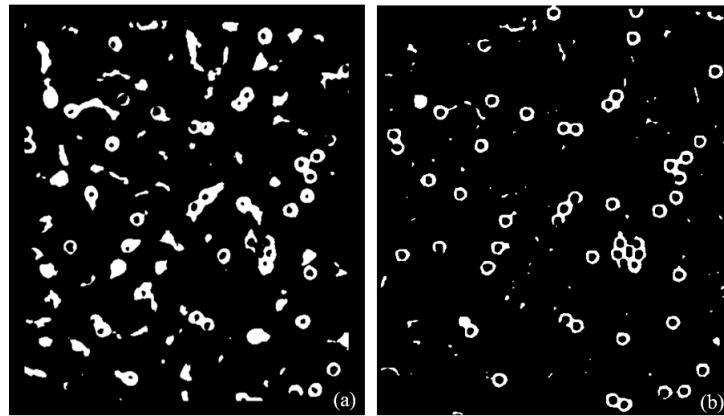

Figure 4.3: Comparison of the results of applying a bandpass filter (Crocker and Grier (1996)) to a raw image (a) and to the same image, after pre-processing through a Bilateral Filter and a Gamma correction, along with the application of morphological operators (b).

Taking these results and using the Hough Transform for circle detection (Rhody (2005)), the only components of the image that are preserved are the detected circular regions. The Circle Hough Transform considers a parameter space of circle radii and center 2D coordinates, proceeding to find parameter triplets to describe the circles one is looking for (the radii are user-defined). This is possible because a circle with radius R and center (a, b) can be described through the equations $x = a + R\cos(\theta)$ and $y = b + R\sin(\theta)$, and, when the angle θ sweeps through the 360º range, the points (x, y) trace the perimeter of a circle (Rhody (2005)). The result of detecting circles and masking the pre-processed image with the detection results can be seen in Figure 4.4.

After this, a simple analysis of connected components allows to discard the particles that are moving in group, since these are not useful for microrheology parameter calculation. This was done by using a connected component area threshold and keeping only the areas with the number of pixels of a single circle (Figure 4.5).

Using this filtered connected components image as a mask for the bilateral filtered image (Figure 4.2 (b)), it is possible to calculate the intensity-weighted centroid of each particle and observe small variations in its position, from frame to frame, with subpixel precision. If the position of the center of each component of the mask would be tracked, instead of that of the intensity-weighted centroid, small-scale variations would be lost and the MSD of the particle movement would be calculated with additional error.
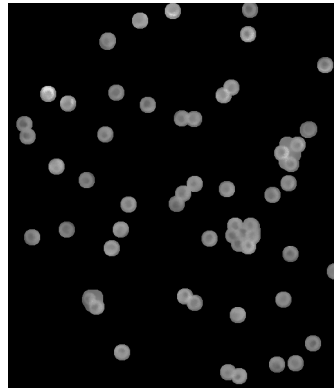
Figure 4.4: Example of the application of a mask created by Hough Circle Detection on the pre-processed image.

Then, Trackpy's (Allan et al. (2018)) linking function, which uses a Nearest-Neighbors approach that will be described later in this chapter, was used to link the particles into trajectories, assigning a label to each trajectory.

Taking the particle detection results that were used for the microrheology study on hemorheology of Campo-Deaño et al. (2013), which are the coordinates of the detected particles, frame to frame, and the IDL (Exelis Visual Information Solutions, Boulder, Colorado) scripts that were used to process these coordinates into viscoelasticity quantities, it was attempted to replicate the results through the tracking functions of Trackpy (Allan et al. (2018)), and MSD calculation and conversion between MSD and the complex modulus ($G'(\omega)$ and $G''(\omega)$) of the Python package Colloids (Leocmach (2015)). For these results to be replicated, the same parameters were used to build the trajectories with the acquired positions and to convert them into complex modulus curves.

However, comparable results using the proposed techniques were only obtained when the number of frames during which a particle can vanish, reappearing nearby, and being considered the same particle, was increased from 2 (the number used in the IDL script for particle position processing) to 4. This is due to the fact that the mask that was created to refine the search for particles is defined by the Hough Transform for circle detection, and when this detection fails, there is occlusion of a particle. Moreover, the search radius defined in the IDL script is of 0.5 pixels, which demonstrated being too small for the acquired data. Instead, a radius of 1.5 pixels was considered. This can be due to inaccuracies in sub-pixel precision, and is probably responsible for the deviation between the MSD curves obtained through the positions acquired by the researcher and the positions acquired through the proposed method, since the problems introduced by the designed algorithm lead to increased entropy in the detected centroid positions. These curves are presented in Figure 4.6. The complex modulus curves acquired through this procedure and using the particle detections done by the researcher are present in Figure 4.7.

The analysis of these results helped to conclude on what should and should not be done to achieve satisfactory results when designing a particle detection method for microrheology studies. First, the process should not rely as much on the pre-processing routine (Figure 4.2), since it
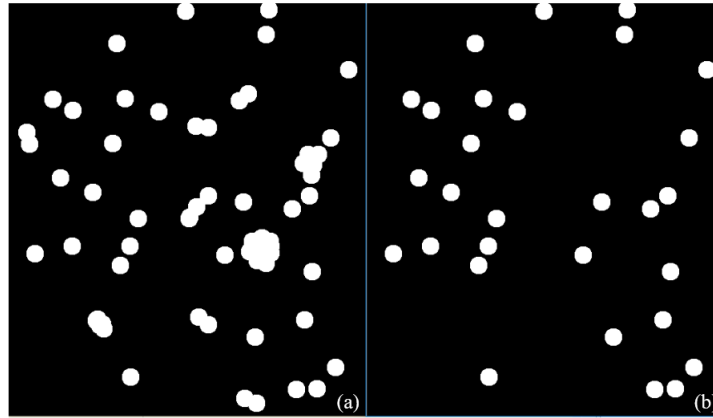
Figure 4.5: On the right, one can see the result of filtering the connected components of the image on the left by their area and keeping only the ones whose area corresponds to that of a single particle.

can increase the computation time prohibitively, when one is analyzing hundreds to thousands of images per study. Moreover, the Bilateral Filter requires the definition of parameters that are not straightforward for the end user to set. Also, using morphological operators for noise removal should be avoided, since it implies setting kernel sizes, which need to be tuned according to the results of bandpass filtering (Figure 4.3). As for the use of the Hough Circle transform for circle detection, it is seen that the inconsistency of its results is a source of error (Figures 4.4 and 4.5). It is, then, a major concern of the final methods that they should create results that are steady from frame to frame.

4.2 Detection methods under analysis

4.2.1 Baseline method - the Centroid Technique

The most common detection method on microrheology studies is, undoubtedly, the Centroid Technique, by C. Crocker and David G. Grier (Crocker and Grier (1996), Crocker et al. (2000), Crocker and Hoffman (2007)), detailed in Section 3.1.3. Its most recent and updated implementation, present on the Python library Trackpy (Allan et al. (2018)), is used in scientific works such as the complete study of the interfacial microrheology of biofilms and protein layers (Allan (2014)), or the study of the remodeling of fluid interfaces by *Pseudomonas aeruginosa*, which tests the bacterial response to physical and chemical stress that is induced by highly asymmetric environments (Denich et al. (2003)).

Even though this method is robust and its sub-pixel accuracy satisfactory, as will be proven in Chapter 5, it produces an overwhelming number of false positives, if one does not constrain its results by fine-tuning multiple hyper-parameters.
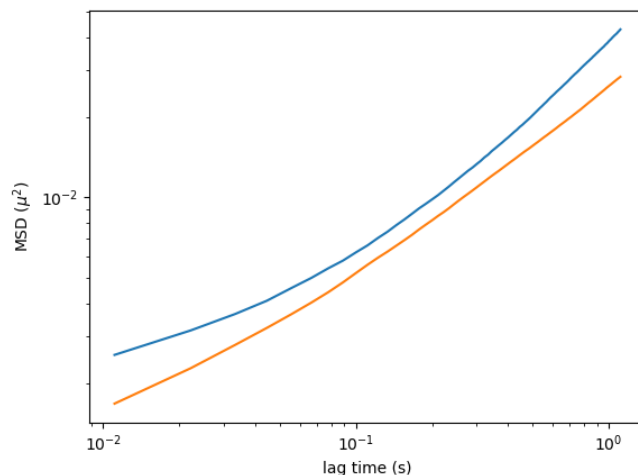
Figure 4.6: The orange line represents the MSD of the tracks obtained with the particle detection data acquired by the researcher, and used in Campo-Deaño et al. (2013), and the blue line represents the MSD of the tracks obtained through the particle detection and linking methods detailed here.

This technique relies on prior knowledge about the particle size, in pixels, or even its extent in both dimensions, if the resolution of the microscopy technique is not the same in the two dimensions (as in confocal microscopy). This is because the particle's apparent radius, in pixels, is used to set the extent of the boxcar average kernel, used to suppress long wavelength contrast variations, but also to identify candidate particles through local brightness maxima, since a pixel is considered a particle candidate if no other, within a distance correspondent to the particle diameter, is brighter. This parameter is, then, of mandatory definition, even though it is not straightforward for the user to define just by observation. A representation of the result of applying a bandpass filter (combination of a boxcar average filter, to remove large-scale variations, and a Gaussian blurring filter, with a kernel width of 1, to remove small-scale variations) that uses the particles' apparent radius as kernel extent for the boxcar filter, and whose result is subject of local maxima identification, is present in Figure 4.8.

Also, one needs to set whether the background is darker or lighter than the particle representations, in order for the detection to be correctly executed. This is because this algorithm considers that the particles are bright features over a dark background, and, if that is not true, the image's intensities must be inverted.

Sub-pixel accuracy is reached by approaching the intensity-weighted centroid, which is analogous to the center of mass of a particle, using the whole region of the particle to resolve the center position. Detailing, if a particle is represented by only one bright pixel, one can only tell that that particle is centered somewhere in that pixel, but no sub-pixel accuracy can be reached. However, if a particle's extent is greater than three pixels, ideally, one can average the pixels' position, weighted by intensity, and reach the precise location of the center. In Figure 4.9, one can see two examples of center detection, in which the addition of Poisson noise affects the offset between the
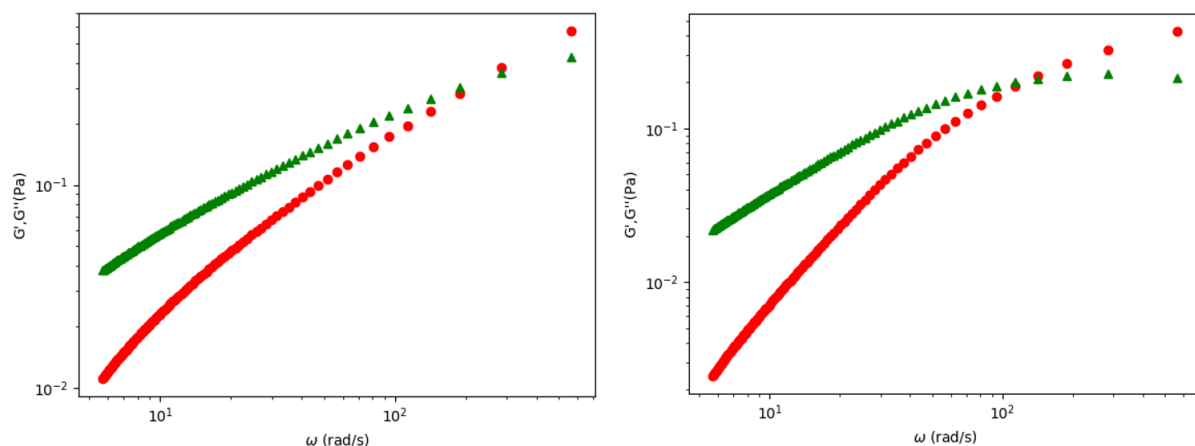
Figure 4.7: On the left, the complex modulus curves for the particle detection data acquired by the researcher, and used in Campo-Deaño et al. (2013). On the right, the same curves for particle detection data acquired through the algorithm proposed here. The green curve represents the loss modulus (G") and the red curve represents the storage modulus (G'). The mean absolute percentage error between the acquired loss moduli and storage moduli is, respectively, of $26 \pm 5\%$ and $54 \pm 8\%$. Adding to the explanation of the differences between these curves comes the fact that the method used in the study Campo-Deaño et al. (2013) was two-point microrheology, while the results in this work were acquired through one-point microrheology, since the two-point method was not readily available.

local maximum pixel center and the center of mass of the particle.

This and every detection method is affected by static error, random error created by fundamental and experimental limitations. Fundamental limitations are related to photon noise, since a particle emits photons stochastically, and its representation is always deviated from its true appearance. The size of this limitation is inversely proportional to the square root of the number of photons that are detected. On the other hand, the experimental limitations that generate error are related to the detector and specimen properties (Crocker and Hoffman (2007)).

Trackpy's implementation of the Centroid Technique (Allan et al. (2018)) outputs many features of the particle candidates, and of the regions in which they were found, such as total brightness, size and eccentricity. The users are, then, invited to discard false positives by manually setting thresholds on these features. Some examples of the use of this technique to detect particles and delete false positives are shown in Figure 4.10. It shows four different types of image included in the dataset used for experimentation in this work. In the first, (a), a synthetic image with 25 bright particle representations, which are modeled through the methods detailed in Chapter 5, is shown. Columns (b),(c) and (d) have images taken from real microrheology setups, (b) being a polyacrylamide blood analogue used in the study detailed in Campo-Deaño et al. (2013), (c) an image of the same fluid taken with a different imaging setup, and (d) an image of real blood used in the same study, Campo-Deaño et al. (2013). The second row of all the columns displays the detection results when only the particle radius is specified, and one can see that the number of false positives detected through this method is prohibitively large for the cases (a), (c) and (d). For these,
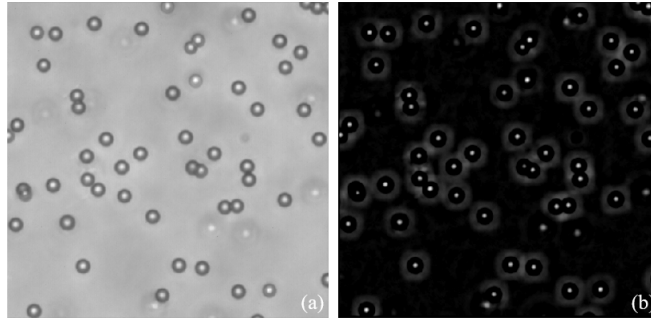
Figure 4.8: (b) is the result of the application of a bandpass filter on image (a), knowing beforehand the particle representation size, so as to set the kernel dimensions for the boxcar filter, used as the high-pass filter.

the properties of the detected particles had to be visually inspected, case by case, to keep only the particles whose features were below or above certain thresholds. The evaluated features are the integrated brightness of the region in which the particle is found, the squared radius of gyration of each region's profile, and the eccentricity of the found particle. One must note that this radius of gyration comes from the definition of moment of inertia of an object, $I = \sum A_p \times r_p^2 = m_0 \times Rg^2$, in which m_0 is the integrated brightness of the region, defined in the previous Chapter (Equation 3.6), A_p is the intensity of a certain pixel, r_p is its position, measured from the center of mass of the particle, and Rg is the radius of gyration. Rewriting, one gets that $Rg^2 = \frac{\sum A_p \times r_p^2}{m_0}$.

With these results in mind, this work's pathway moved towards creating ways to delete false positive detections through a more robust method, that would not require visual inspection, and that would not be as dataset-specific as the thresholding of feature values that are completely dependent on the characteristics of each image set. This means that, for the detection to be as automatic as possible, a measure of how much a detected region resembles a particle representation should be created. Moreover, the Centroid Technique is not capable of isolating all the true positive particle representations in cases such as the one shown in Figure 4.10 (d), even after careful examination of the feature space provided through this method. This would suggest that another method of particle search could be combined with the Centroid Technique to ensure that all the true positive cases are included in the set of particle candidates to be further analyzed. Also, the accuracy of the sub-pixel centroid estimation of each particle needs further examination, which will be done in Chapter 5.

4.2.2   Calibration

Before moving to the automation of particle detection, it is necessary to create a preliminary step, which may be called calibration, that estimates the radius of the particles and tells whether the background is lighter or darker than the particles, since these are the two mandatory input parameters for the Centroid Technique. However, the calibration method should be applied on a denoised, highly-contrasting image, reason why a simple pre-processing routine is applied beforehand.
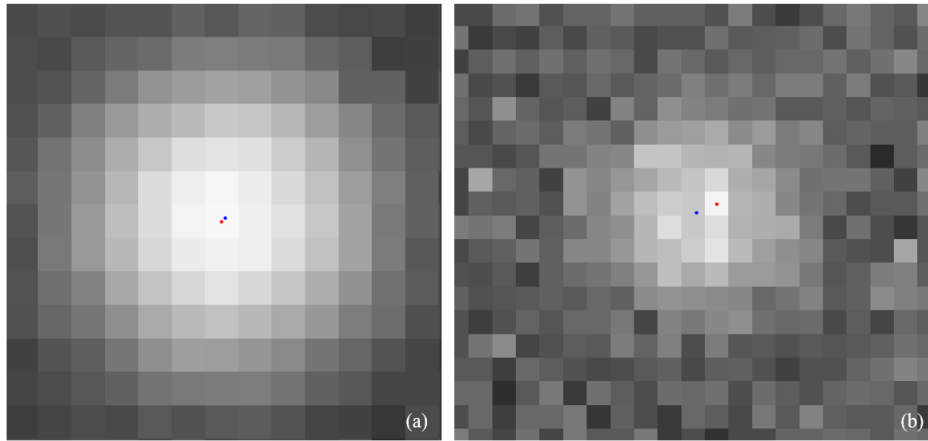
Figure 4.9: (a) is a synthetic representation of a particle, in an image with Poisson noise, resulting in a SNR of 14. (b) is a representation of a particle in an image with SNR of 6. The centers of the brightest pixels of the regions are marked in red and the centers of mass in blue. The offset between the pixel center and the center of mass is of about 0.146 pixels for image (a) and 0.943 pixels for image (b).

An illustration of this pre-processing and initial segmentation pipeline can be seen in Figure 4.11.

4.2.2.1   Pre-processing

The contrast of the images is enhanced via gamma adjustment (Reinhard et al. (2010)), technique that corrects the image's luminance. This correction was previously described, in Section 4.1. However, a change was made in this technique: the gamma coefficient can be manually set, or inferred by a combination of Adaptive Gamma Correction with Weighting Distribution (AGCWD) (Mariyam and Philip (2014)) with regular gamma correction, done by adjusting a power law to the transformation function of the AGCWD correction and using the exponent of this power law as the coefficient for regular gamma correction. This way, the user can perform an adaptive gamma adjustment and use the resultant coefficient as an intelligible reference.

This is followed by an estimation of the image noise variance (Immerkaer (1996)), assuming that the noise is modeled by an additive zero mean Gaussian. A Gaussian filter (Reinhard et al. (2010)) having the estimated variance is then applied to reduce noise. To revert the enlarging effect that this filter has on foreground objects, the erosion morphological operation is applied (Serra (1983)), having as kernel a circle with the calculated noise variance as radius.

4.2.2.2   Calibration method

Following pre-processing, we start by computing the local image gradient with a rank filter (Gonzalez et al. (2002)), meaning that the local histogram is used for its calculation. The gradient image is denoised through a rolling-ball background subtraction (Sternberg (1983)). Also, the pre-processed original image undergoes the same background subtraction to create two separated
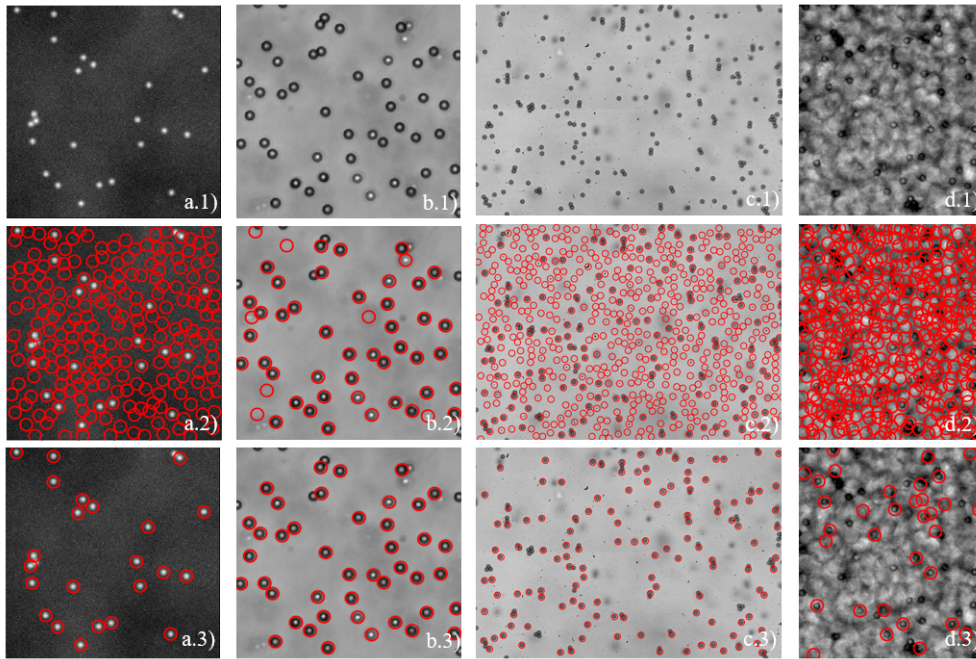
Figure 4.10: Examples of particle detection through the techniques detailed in Crocker and Grier (1996), Crocker et al. (2000), Crocker and Hoffman (2007), and further attempt of false positive deletion by thresholding region parameters. Column (a) presents results for a synthetic dataset image, and (a.2) shows the particles that are found by the cited methods, if only the particle radius is specified. (a.3) shows the results of search refinement, by analysis of the integrated brightness and eccentricity of the particle candidates, and radius of gyration of each region's profile, and definition of thresholds on these features. Columns (b) and (c) present the same results for polyacrylamide fluid images, and (d) shows that particle detection through these methods is a hampered task for the case of real blood images.

images, containing, respectively, the background and foreground of this image, which can be compared to find out whether the background is brighter or darker than the particles. Using Otsu's method (Otsu (1979)) to establish a gradient threshold, one can separate the image gradient values into two classes, where the class encompassing the higher gradient values is the most likely to represent the particles and their steep intensity transitions. This method is invariant to the foreground being lighter or darker than the background, but is highly sensitive to high frequency noise, reason why previous and further denoising are required. Therefore, applying the morphological opening and closing to the thresholded (binary) gradient image, with a kernel that takes the 4-neighborhood of each pixel, one can remove salt and pepper noise. Then, the particles' contours are filled in, creating solid particle regions.

Through the analysis of an histogram created for the region area values, the most common area value is defined as representative of true particles, if the eccentricities of the regions associated with these areas are characteristic of circular regions. Regions are considered far from being circular, and therefore rejected, if their eccentricities surpass the value of 0.6 (in a scale from 0 to 1, being 0 the eccentricity of a perfect circle). An illustration of this pipeline detail is provided in
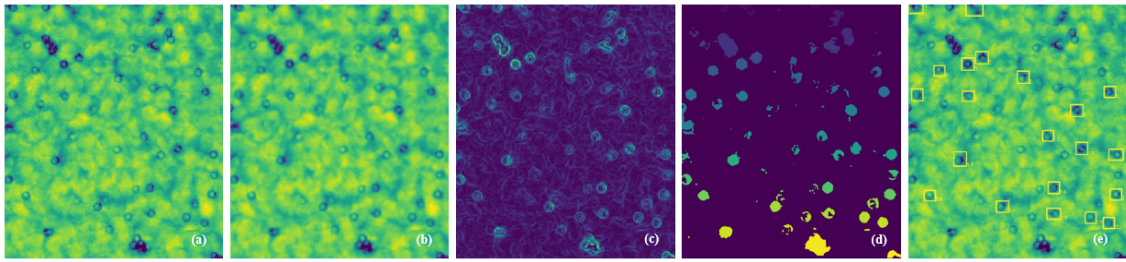
Figure 4.11: Illustration of the pre-processing and initial segmentation pipeline. (a) Example image from blood sample video used in Campo-Deaño et al. (2013). (b) Smoothed image according to the estimated noise variance. (c) Local image gradients. (d) Clustering through histogram analysis. (e) Identified particles.

Figure 4.12, and an example of the iterative process is given in Figure 4.13. Through this figure, one can follow the selection of the regions that are most likely to represent particles: from left to right, the first histogram is plotted, and, ignoring the areas contained in the first bin, it can be seen that the second bin has the highest occurrence value. The particles whose areas fit the second bin are highlighted in the image below the histogram, in red. Because these particles have an average eccentricity above 0.6, their regions are excluded from further evaluation, and the histogram in the middle column is plotted. In this, the process is repeated, and it is seen that the average eccentricity of the kept regions is still above 0.6. Finally, taking only area values from 0 to 600 (pixels), one can cluster the set of particles whose eccentricity is, in average, below 0.6

Because Brownian motion is defined as having low amplitude, one can infer that the particles will not move too far away from their initial positions. As stated previously, the Centroid Technique is, sometimes, unable to detect all the particles in one image, either because of the disparity of their properties, or their momentary occlusion. With this in mind, it is set that the particle regions found in this initial calibration are fixed as particle candidates throughout the whole video, preventing that certain regions are overlooked and some particles missed.

The activity diagram for pre-processing and calibration is presented in Figure 4.14.

4.2.3 Refining particle detection

Two ideas were explored with the goal of creating a metric of resemblance to a particle representation that would not be dataset-specific, but also aiming to determine what method is the most accurate for centroid detection, to the sub-pixel level. The first is the fitting of each region created by the Centroid Technique, when only the particle radius is specified (and the image is inverted if the particles are darker than the background), to a two-dimensional Gaussian profile. The second is a Radial Symmetry-based approach, as described in Parthasarathy (2012), which tries to identify spherical particles and accurately compute their centers by assuming that the intensity of a particle representation is radially symmetric in relation to the particle center. Both techniques are detailed in Chapter 3.
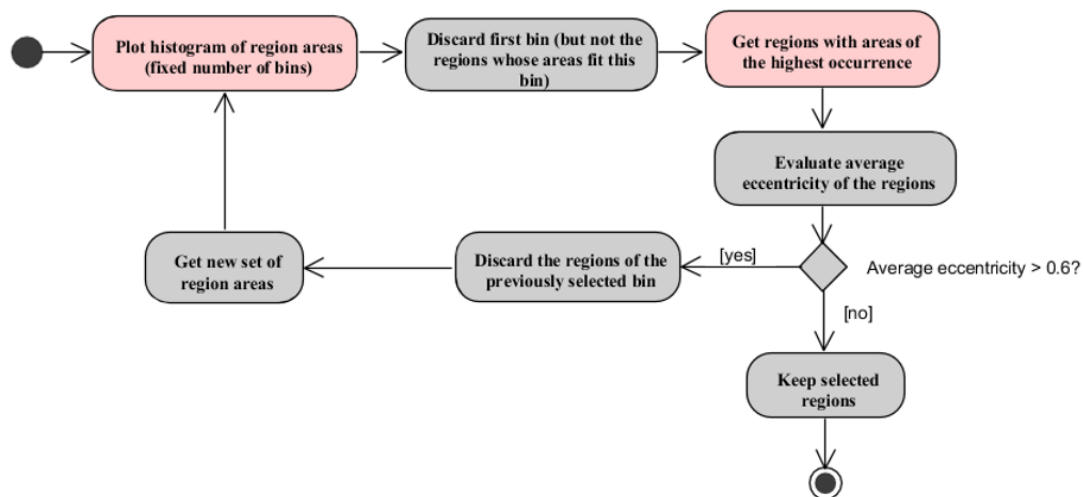
Figure 4.12: Illustration of a detail of the calibration pipeline that concerns the choice of region areas that may correspond to particles, iteratively by the analysis of area histograms and region eccentricity values. The activities in pink have their outputs shown in Figure 4.13
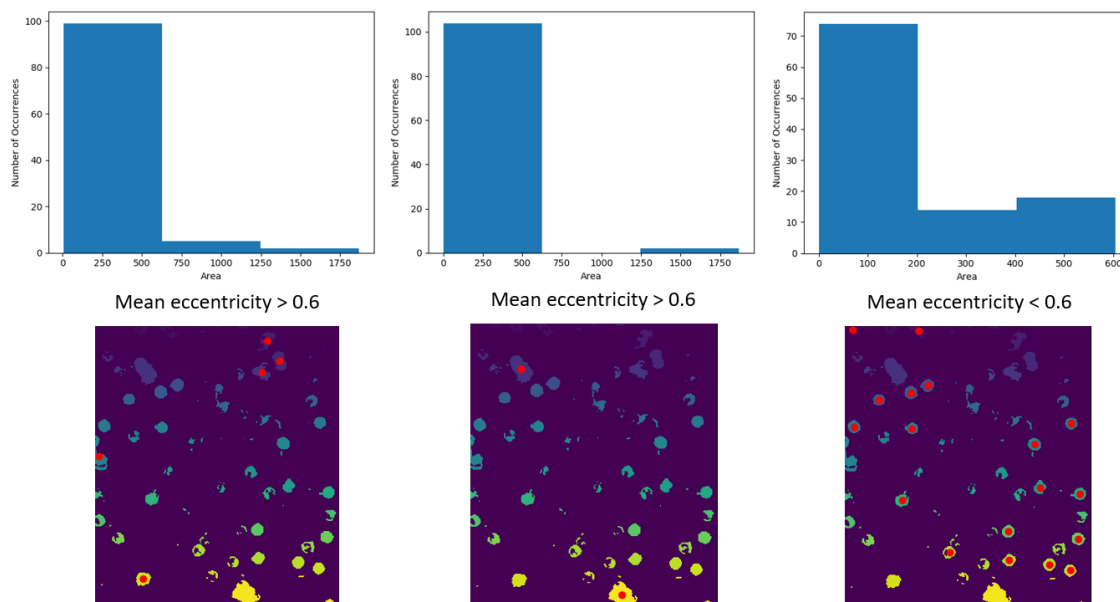

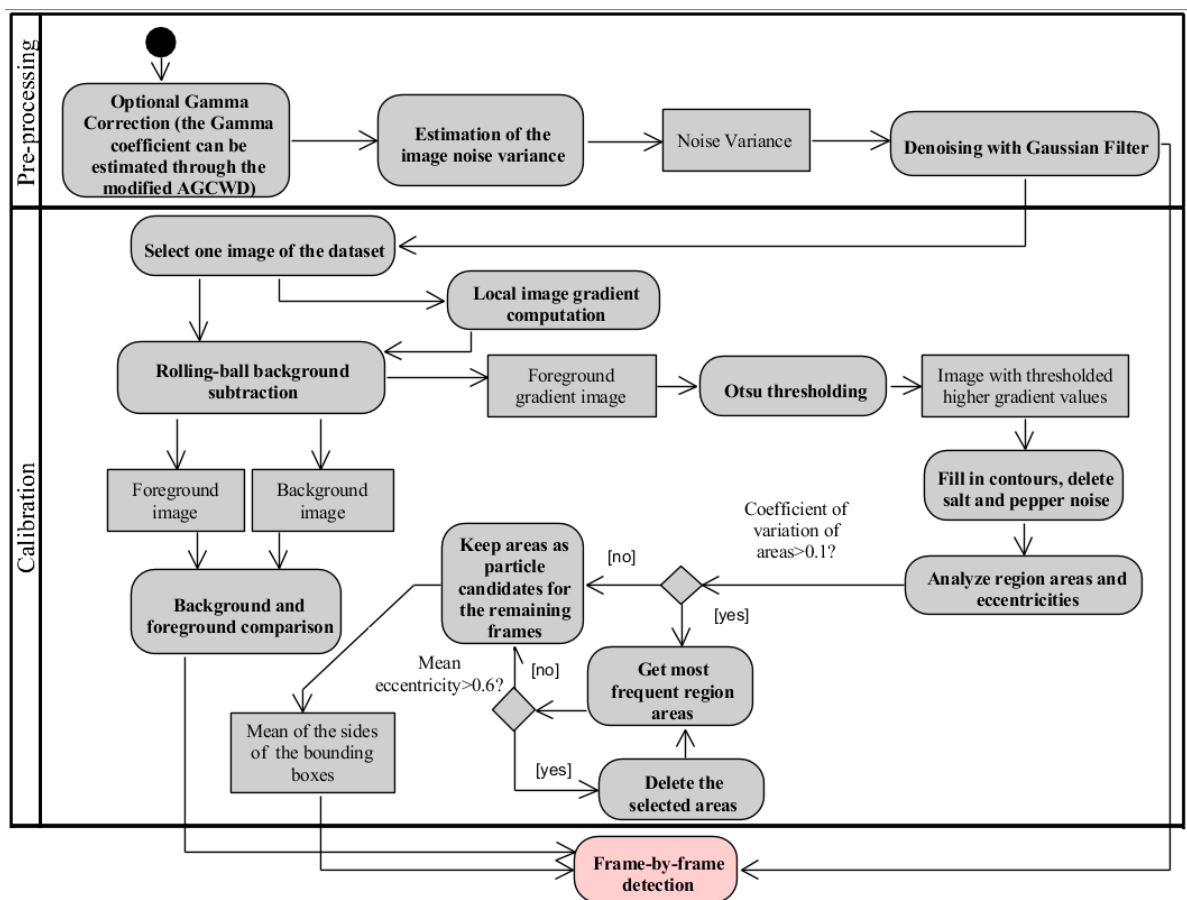Figure 4.13: Illustration of the iterative process of selecting particle regions.

Figure 4.14: Activity diagram of the pre-processing and calibration routines.

4.2.3.1   Gaussian fitting through least-squares estimation

As discussed, this type of fitting method is optimal when the Point Spread Function of a particle representation is known to be Gaussian, but its accuracy can drop if the particles are shown as dark rim structures, brighter on the inside, as the examples seen in Figure 4.10 (b), (c) and (d).

Gaussian fitting is done through least-squares estimation, which minimizes the sum of squares of an error function defined for the fitting of Gaussian parameters to a given search region. This error function is the subtraction between a Gaussian with a set of parameters and the image region it is fitted to. The initial parameter estimates of the Gaussian that is fitted are given by the region's moments, namely the mean in each dimension (first moment) and the variance (second moment). The center of each particle is given by the center of the fitted Gaussian.

After fitting a Gaussian profile to each region, one can select the regions with higher *goodness of fit* by considering only the Gaussian profiles that converged before the 100th iteration. However, that is not enough to do a full deletion of the false positive detections, reason why a feature clustering approach, combining the region features that were previously detailed and the fitted Gaussian's features, was tried. The fitted Gaussians are clustered through Fuzzy C-means (Ross et al. (2004)), using as features their standard deviation and region features: the integrated brightness, squared radius of gyration and eccentricity of the circular region to which the Gaussian is being fitted. A membership degree is assigned to each feature point, being higher for points that are closer to the center of the cluster. The *fuzzifier* coefficient, which defines how fuzzy the clusters will be (how small can the membership values become) is set to 2, a common value when there is little information about the features (Klawonn and Höppner (2003)), and the stopping criteria are an error of 0.005 or a maximum number of iterations of 1000. Two data clusters are defined with this method. Then, cluster analysis is conducted in a simple manner: the values of the integrated brightness that are placed in each cluster are compared and, if it was previously seen that the background is darker than the foreground/particle candidates, the cluster that is kept is the one with the higher integrated brightness values, and vice-versa. It must be highlighted that data clustering is only done if the number of points detected is larger than two times the number of points in the calibration phase. or if the coefficient of variance of the features (given by the mean of the quotients between standard deviations and means of each feature) exceeds 0.5. An illustration of the Gaussian fitting method as a particle center estimation layer is presented in Figure 4.15.

4.2.3.2   Radial Symmetry method

This algorithm estimates the particle center as the point with the maximum value of radial symmetry, working for differently shaped particles, such as concentric rings and Gaussian intensity distributions. To do so, it assumes that the lines parallel to the intensity gradient of an image region that has perfect radial symmetry will be pointing, in any point, towards the origin, which is the center one wants to find. Therefore, the origin that minimizes the weighted sum of the squared distances between the lines parallel to the intensity gradient is the center of the particle representation. The mean squared distance between the lines parallel to the gradient and the center,

weighted by intensity, are a measure of *goodness of fit*. If the coefficient of variation of the set of mean distance squared values of the detected particles is larger than 0.2, clustering is done through the method presented in the last subsection, but adding the mean squared distance to the feature space, instead of the Gaussian's standard deviation, which is not evaluated in this case. The cluster that is kept is the one that contains the lower mean distance squared values, denoting greater radial symmetry of the regions.

An illustration of the Radial Symmetry method as a particle center estimation layer is presented in Figure 4.15.
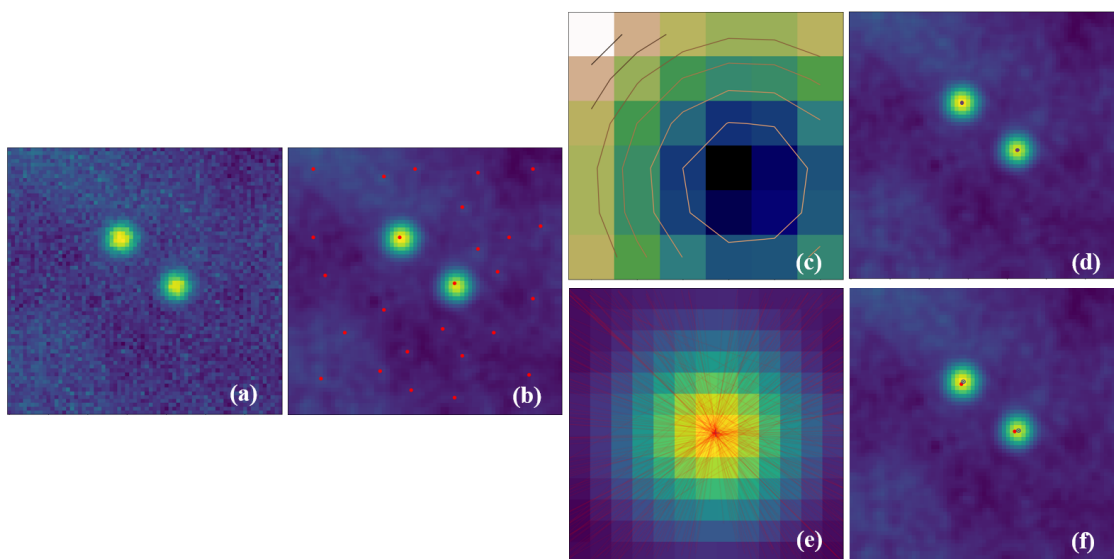

Figure 4.15: Illustration of the particle center detection through both approaches.(a) Synthetic 2-particle image generated with Poisson noise of SNR=10 and fractal noise merged with a weight of 0.1. Image generation method is detailed in Chapter 5. (b) Centers of all the defined search areas. (c) Detail of the XY-plane projection of the Gaussian that is fitted to the particle on the left. (e) Detail of a search region in which some of the lines parallel to the image gradient are drawn and their maximum convergence point identified. (d),(f) Refined positions of the centers through the Radial Symmetry method and Gaussian fitting, respectively, with the true centers in blue.

4.3 Linking particle positions into trajectories

The chosen linking approach was the adaptation of Crocker and Grier's (Crocker and Hoffman (2007)) methods by the authors of the Trackpy library (Allan et al. (2018)), described in (Allan (2014)). This method is based on Feature Point Tracking, described in the third Chapter, and the cost function it minimizes is the total length of links, from frame to frame. This cost function is based on the statistics of Random Walks, which show that a particle with Brownian motion is most likely found near its last position. This algorithm is rigorously correct for non-interacting particles which undergo Brownian motion (Allan (2014)).

A Nearest Neighbor approach was chosen because the microrheology setup videos analyzed complied with all the requisites for this type of algorithm to have good performance: a frame rate

superior to the one reported in the first microrheology studies (60 frames per second) (Crocker and Grier (1996)), through which small and fast movements of the particles could be correctly captured, and a purely Brownian motion (with few exceptions) being displayed by all the particles in the video. Moreover, in microrheology studies, particles should be placed distant from each other to avoid particle-particle interactions, and particle aggregates cannot be considered in this type of studies. Because of this, a linking method that requires that the particles are not too close to each other can be easily adapted to this type of procedure. The linking methodology in use is able to deal with the temporary disappearance of a particle from the field of view, as long as it reappears nearby after as many frames as the user allows. This is because it contemplates "virtual" particles in the association matrices between detection sets, as explained in Chapter 3.

Unlike other Nearest Neighbor approaches, this one only deals with the Euclidean distance feature to link particles into tracks, since the appearance of all the particles embedded in the fluid that is being studied should be, in theory, the same, and their differences only due to artifacts that can vary from frame to frame. This way, particle features related to particle appearance should not be included in the linking method.

Assigning particle detections, in each frame, to every track, would imply having to test every track-particle combination to find out what solution is the one that minimizes the previously described cost function. This would be highly inefficient. A simple solution for this problem is the definition of a search range, around which particles are looked for, limiting the number of calculations involved in resolving a sub-network. A great accuracy in the linking process would, obviously, be achieved with the definition of a large search range, but that would contradict the purpose of defining this search range. A trade-off between search range amplitude and computation efficiency should be defined, and one can easily tell whether a certain search range is adequate for a dataset as the number of linked tracks drops to an almost null value when the search range limit is approached (Figure 3.14). It is left for the end user to define this range by observing the particle motion during a few frames: they should set a value greater than the biggest displacement that can be seen from one frame to another, but smaller than the smallest separation between two particles.

Summing up the basic principles of this linking method, it defines a Brownian predictor in which the search range is centered, for a certain frame t_1, $P(t_1, t_0, \vec{x}(t_0)) = \vec{x}(t_0)$, in which $\vec{x}(t_0)$ is the current position of a certain particle.

The method for resolving sub-networks is a k-d tree (with only one feature, being analog to a binary tree), which is a space-partitioning data structure that organizes points in the Euclidean distance feature space, for Nearest Neighbor search (Naylor (1998)). It works by successively splitting the feature set (composed by Euclidean distances) by its median, node by node, until the leaves have one point, each, avoiding that all the particles in a given search range are evaluated regarding their distance to the newly formed track. The tree is analyzed from root to leaves to find the particle with the shortest distance to the track. The time complexity (in big O notation) falls from $O(n^2)$ to $O(log(n))$ by using this method instead of individually testing each combination, for a tree with n points.
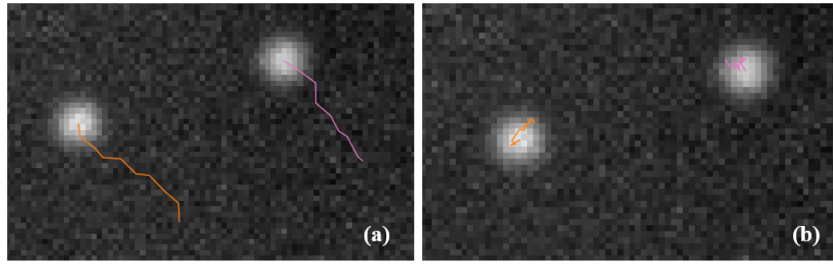
Figure 4.16: Illustration of drifting particles with Brownian motion, following a [2,2] pixel drift vector (pointing down and right from the upper left corner) for 7 frames (a), and their trajectories after drift correction (b).

Particles can drift together in a directed movement, getting carried away from their initial positions. Calculating and correcting the drift is possible through a simple post-processing routine, in which one averages the particle velocities per frame and subtracts the displacement, caused by this average speed, to the final tracks. A simulation of drifting particles through the synthetic database (detailed in Chapter 5) and further drift correction is presented in Figure 4.16.

4.4 Final Particle Tracking pipeline

As will be detailed in Chapter 5, the methods that were tried, in order to build a pipeline for particle tracking, have both strengths and weaknesses. The Radial Symmetry method, while advantageous for the definition of a metric of resemblance to a particle representation, which can be used for clustering and false positive deletion, has the drawback of detecting the particle centroids with low accuracy, inducing error in the trajectories that are, then, formed. Gaussian fitting for particle detection revealed to be computationally expensive, and its accuracy lower than that of the Centroid Technique, for particle center definition. Moreover, the metrics it creates for false positive deletion are intrinsically related to the Gaussian profile of each detected particle, which may not be well defined, even for true positive cases. With these results in mind, a final particle tracking pipeline was delineated. This contains all the previously defined pre-processing and calibration steps, but the method chosen for false positive deletion is clustering of the feature space together with the Radial Symmetry feature, which is the mean squared distance between lines parallel to the intensity gradient, and the method chosen for sub-pixel refinement is the Centroid Technique.

An activity diagram for the particle tracking pipeline, following the calibration routine, is presented in Figure 4.17.
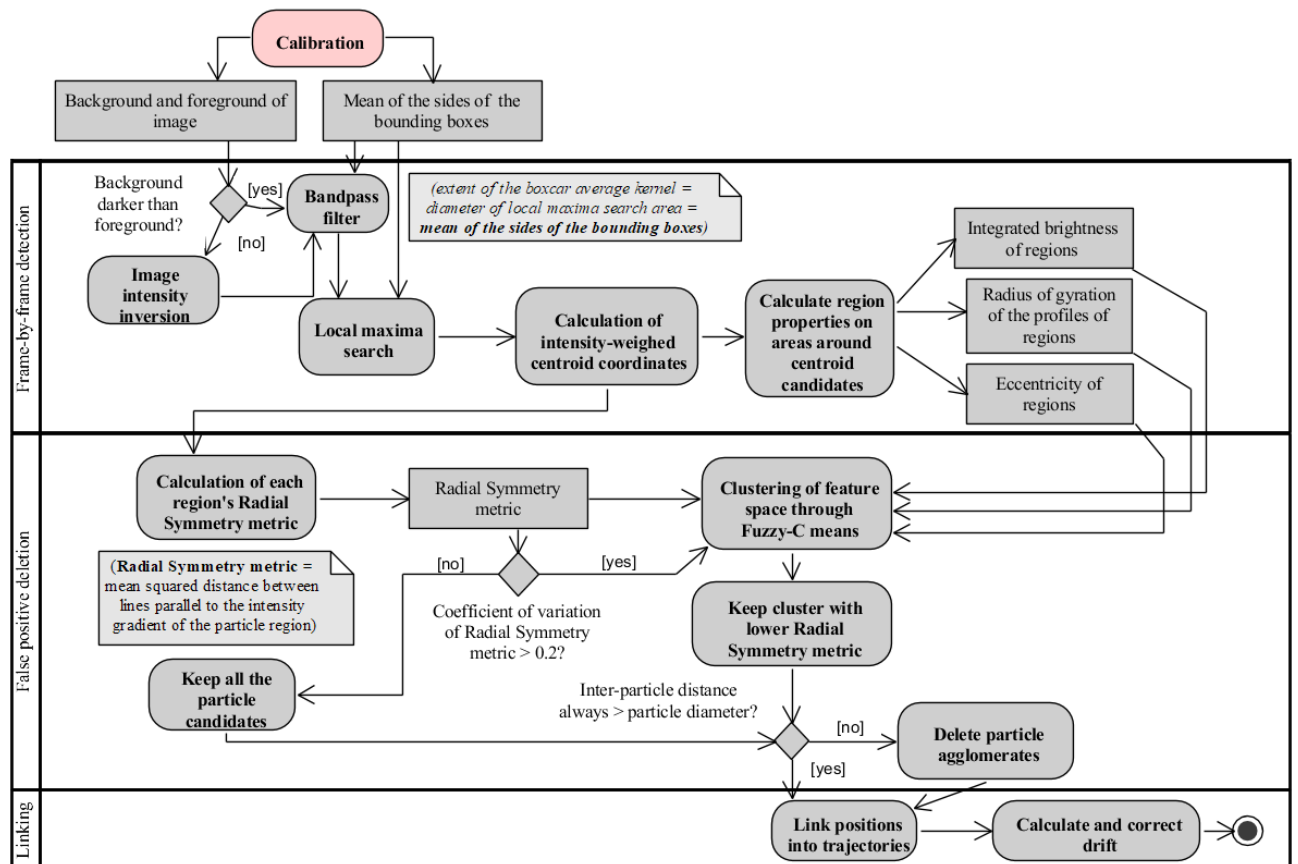
Figure 4.17: Activity diagram of particle detection, false positive deletion and linking.

Chapter 5

Experiments and Results

In this chapter, both the used databases and the results acquired through them, are detailed and analyzed.

For a complete study on the performance of the designed algorithms' pipeline, a synthetic database had to be created. This is mandatory because the utilized real microrheology videos were not annotated, and the true positions of each particle's centroid, throughout the duration of the videos, was not known beforehand.

However, this study would not be completed if the algorithms were not tested in real microrheology scenarios. Through these, sub-pixel accuracy could not be evaluated, but the number of detected particles could be assessed, to quantify the precision and sensitivity of the methods.

This chapter also presents the comparison between microrheology results calculated through the proposed tools and macrorheology values acquired for the same fluids, and even previously published complex moduli obtained through the analysis of the same videos.

5.1 Experiments in synthetic microrheology database

5.1.1 Synthetic video particle-tracking microrheology database

The simulated multi-particle images used to test the developed particle tracking algorithms are generated from an extension of the algorithms described in Parthasarathy (2012) [1], which model single fluorescent particles as point sources in random positions of the image, convolved with a point-spread-function (PSF):

$$PSF(r) = \left(\frac{2J_1(v)}{v} \right)^2 \tag{5.1}$$

that is characteristic of the representation of a particle in fluorescence microscopy, where J_1 is the Bessel function of the first kind, of order 1, $v = (2\pi NAr)/(\lambda n_w)$, λ is the wavelength of light, NA is the numerical aperture of the objective lens, n_w is the index of refraction of water and r is the radial coordinate (Parthasarathy (2012)). The simulated particles were created by applying this function with λ=550 nm and NA=0.55 (numerical aperture of the lens of the microscope

---

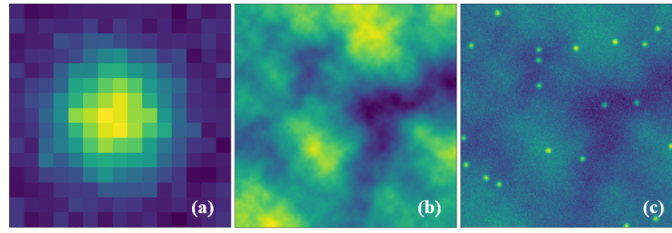[1]Matlab code available in https://pages.uoregon.edu /raghu/particle_tracking.html

Figure 5.1: Illustration of the image sequence generation pipeline.(a) Detail of particle generated with a PSF characteristic of the representation of a particle in fluorescence microscopy, and applied Poisson noise (SNR=8). (b) Cloud-like structure to be merged with a weight of 0.2, forming the final image, (c).

used in Campo-Deaño et al. (2013)). A λ of 550 nm is used because, in most of the cases, microscopists use white light generated by a tungsten-halogen bulb to illuminate the specimen, and the visible light spectrum is centered at about 550 nanometers, the dominant wavelength for green light, to which our eyes are the most sensitive. These parameters would result in an hypothetical microscopic image with a resolution of $0.61 \mu m/pixel$, assuming that the microscope would be in perfect alignment, having the objectives appropriately matched with the condenser (Davidson (2019)).

The multi-particle images are complemented with Poisson-distributed noise. For this type of noise, the signal-to-noise ratio is the square root of the number of photons detected at the brightest pixel. Therefore, the pixel intensities are scaled such that the peak intensity is equal to the square of the signal-to-noise ratio, and a constant background is replaced by pixels with a random intensity, drawn from a Poisson distribution whose mean is the expected background intensity (Parthasarathy (2012)). Because this image transformation only creates short wavelength noise, an additional source of large wavelength noise was added, to simulate the background effects that exist in inhomogeneous fluids, such as blood (see Figure 4.10 (d)). This noise layer has a cloud-like 2D texture generated by the superposition of increasingly upsampled portions of a white noise image, which creates a fractal noise pattern (Gardner (1985)). Asides from adding noise to the images, an optional gamma correction (Reinhard et al. (2010)) is made.

Besides mimicking Brownian motion, the proposed image generation algorithms also allow the existence of a drifting motion that is equally applied to all the particles, through the definition of a motion vector that is added to the previously defined random positions of the particles. The pipeline for image generation is visually detailed in Figure 5.1.

5.1.2 Performance evaluation on synthetic data

The detection capabilities of the methodology to be tested were evaluated in this synthetic database, whose PSF for particle generation is Gaussian-shaped. The dataset created for evaluating particle detection is composed of 12 sets of frames with both width and height of 300 pixels, with 10 particles each, creating a particle density slightly lower than that of regular microrheology videos,
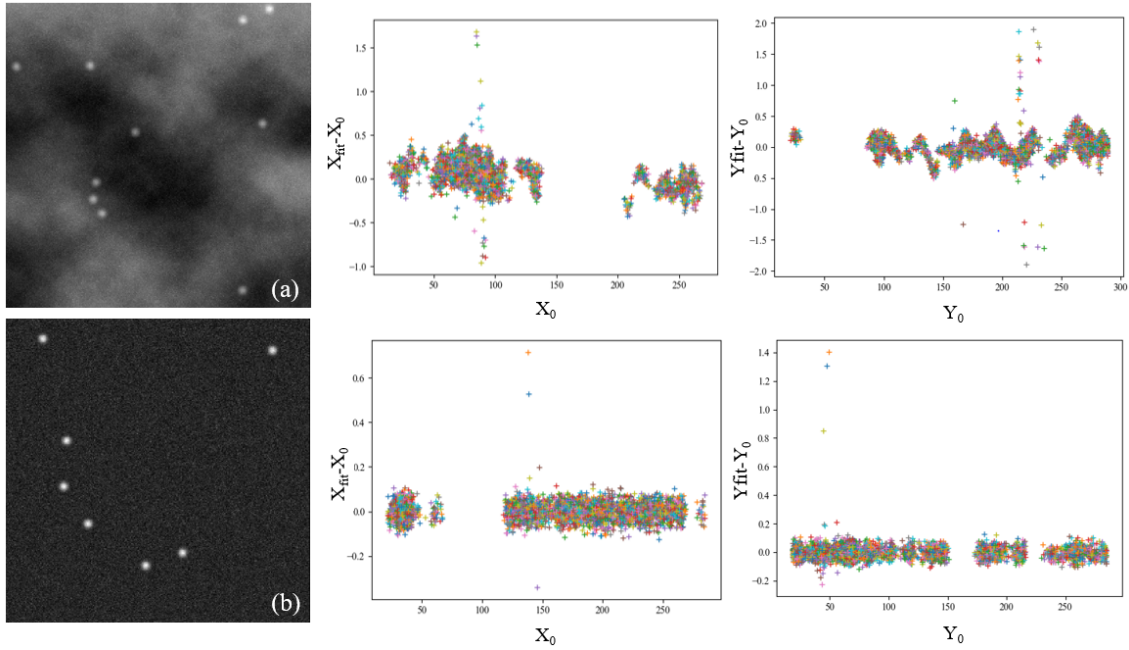
Figure 5.2: Effect of long-wavelength noise on particle center estimation. (a) and (b) are example frames of the sequences for which the accuracy of particle detection in *x* position and *y* position is detailed in the plots on the right. The frame sequence represented by (a) is affected by Poisson-distributed noise with an SNR of 10 and a long-wavelength noise superposition weight of 0.5, while the frame sequence represented by (b) is only affected by Poisson noise, having an SNR of 10. In the plots, x_{fit} and y_{fit} represent the calculated coordinates of each particle that is detected, and x_0 and y_0 their true coordinate values. The method used for detecting the centroids is the Centroid Technique.

but of easier visual inspection. The particles of this dataset move without drift and a maximum of 1 pixel per frame, in any direction. The accuracy of centroid detection is computed for a variety of Signal-to-Noise Ratio (SNR) values and weights of long wavelength cloud-like noise, when estimating the centroid position through the Centroid Technique, the Radial Symmetry method and Gaussian fitting. The regions in which the centroids are refined are the same for every method, and are specified by feature clustering via Fuzzy-C means, as described in section 4.2.3.2, using Radial Symmetry features and region appearance features. It is expected that increasing the SNR of the image set leads to an overall increase in detection accuracy, but adding and increasing the weight of the long-wavelength noise should not only have a similar effect to the SNR decrease, but also create regions with different particle detection accuracy. Therefore, as shown in Figure 5.2, a background having long-wavelength noise introduces heterogeneous noise magnitude across the image, leading to varying accuracy regarding the detection of each particle.

One can examine the accuracy of the three methods (offset between the detected centroid location and its true position) through the analysis of the Mean Total Error, defined by Equation 5.2, the squared root of the average of the squared errors in the calculated *x* and *y* positions of each

of the n particles, respectively.

$$\frac{< e_x^2 + e_y^2 >^{1/2}}{n} \tag{5.2}$$

Similar studies were conducted in Parthasarathy (2012), but one must stress that the simulated images in this case contain several particles, which can assume different positions from frame to frame, being found in areas with little or much noise, or even being possibly agglomerated or occluded by other particles. These conditions are more similar to those of real environments that occur in microrheology studies than just considering the detection accuracy of a single particle as it moves in a confined space towards and away from the image borders, while affected by different SNR values, which are the conditions simulated in Parthasarathy (2012).

Not all the image sets could be pre-processed equally, since the performance of the calibration pipeline depends on the contrast between the particles and the foreground, and this must be enhanced in some of the cases in study. The final algorithm pipeline gives the user a choice of which gamma coefficient to use on gamma correction (Rosebrock (2015)) or whether or not to use the adapted version of adaptive gamma correction to establish this coefficient (Mariyam and Philip (2014)). For most cases, the image sets could be used for particle detection without gamma correction, but manually shifting the images' luminance to darker values was needed for the calibration method to provide reliable particle dimensions and image properties, to allow a successful detection in cases such as the images with a weight of overlapping of long-wavelength noise above 0.3.

The conclusions of this study can be inferred through the analysis of the plots in Figure 5.3, in which one can see that the same particles were detected with larger accuracy by the Centroid Technique, in every case, followed by the Gaussian Fitting method, and lastly the Radial Symmetry method for centroid detection. One must also note that the execution time of the whole pipeline (after calibration), per image, using as centroid detection refinement either the Radial Symmetry method or the Centroid Technique is the same, since the false positive deletion methodology involves knowledge acquired from Radial Symmetry features and region features. This execution time is of about 0.25 seconds for each image, with little variation (in the order of milliseconds) for noisier images. As for the Gaussian Fitting method, the computation time gets prohibitively large, with values around 1.2 seconds per image. This is mainly due to the optimization scheme used for Gaussian Fitting (least-squares estimation) involving iterative search for optimal parameters. For these reasons, the output of the particle detection pipeline, in terms of accurately detected particle centroids, is given by the Centroid Technique. The Radial Symmetry method is kept for the false positive deletion to be possible, and the Gaussian Fitting method is discarded from the pipeline.

Method accuracy results are detailed for the image set with SNR=10 and weight of long-wavelength noise overlapping of 0.1 in Figure 5.4. It shows that the mean total error has dispersed and globally higher values for the Radial Symmetry method. For the Centroid Technique or the Gaussian Fitting approach, the mean total error is more prominent for certain frames. This is the case, for example, of frames around 250, 310 or 430. Taking one of these cases, it was
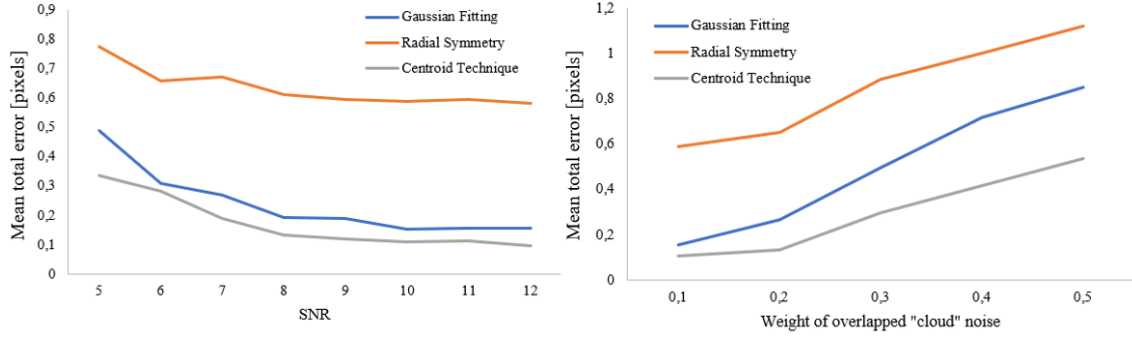
Figure 5.3: On the left, the mean total localization error for particles in simulated images over a range of Signal-to-Noise Ratios from 5 to 12 (the simulated images have intensity values in the range of 8-bit unsigned integers, from 0 to 255), and on the right, the localization error for an image set affected by long-wavelength, cloud-like noise, overlapped with a range of weights over images with an SNR of 10. 500 images of each SNR and of each overlapping weight were used for each test, each with 30 particles, accounting for 4000 images for the SNR tests and 2500 images for the long-wavelength noise tests.

possible to understand the main cause of the localized inaccuracy: the presence of aggregated particles, whose occurrence regions overlap, and are considered as being only one. This leads the detection algorithms to try to make just one particle detection and centroid refinement in that area, in which two particles should be defined, as can be seen in Figure 5.5, showing a detail of frame 446 of the sequence represented in Figure 5.4. Even though this situation looks problematic, due to the possible presence of particle aggregates in real images of microrheology studies, it is mandatory (for ensuring the correctness of results) that the detections which are included in aggregates are deleted, since the movement of agglomerated particles is not purely Brownian. This being said, as long as the accuracy of detection of isolated particles is not compromised, these punctual inaccuracies do not pose a threat to the overall results, as agglomerates are removed in a posterior step.

As for the number of particles that are detected per image, the dataset of 4500 images with SNR values from 5 to 13 was analyzed, and it was concluded that the average sensitivity is of 0.926 ± 0.033. Sensitivity (or recall) is the proportion of particles that are correctly identified as such, being defined as can be seen in Equation 5.3.

$$Sensitivity = \frac{TP}{FN + TP} \tag{5.3}$$

TP is the number of true positives and FN is the number of false negatives. Moreover, the average precision of the Centroid Technique detections for this dataset is of 0.990 ± 0.011. Precision is the fraction of true particles among all the detections. It is defined as can be seen in Equation 5.4.

$$Precision = \frac{TP}{TP + FP} \tag{5.4}$$
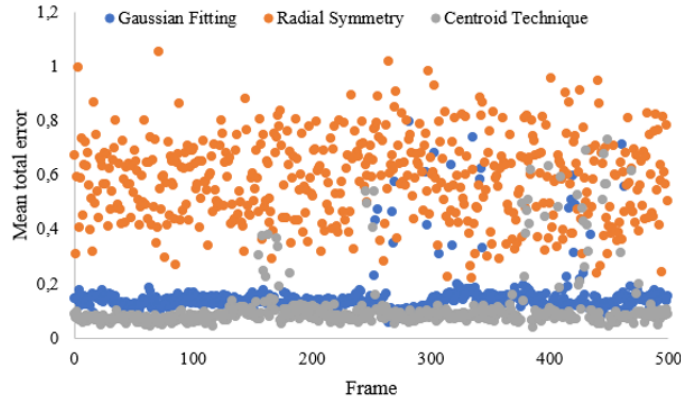
Figure 5.4: Characterization of the three tested methods for particle detection according to their Mean Total Error, for an image sequence with SNR=10 and weight of long-wavelength noise overlapping of 0.1. This sequence has 500 frames and 30 particles per frame, which can form agglomerates, since their movement is random, limited to a maximum of 1 pixel per frame, in any direction, and not confined.

Figure 5.5: Detail of frame 446 of the sequence detailed in 5.4, one of the problematic frames in terms of accuracy of the Gaussian Fitting method and Centroid Technique for particle detection. Near the top edge of the image (a), one can see a particle agglomerate, incorrectly identified as just one particle (b), decreasing the mean accuracy of particle location for this specific frame.

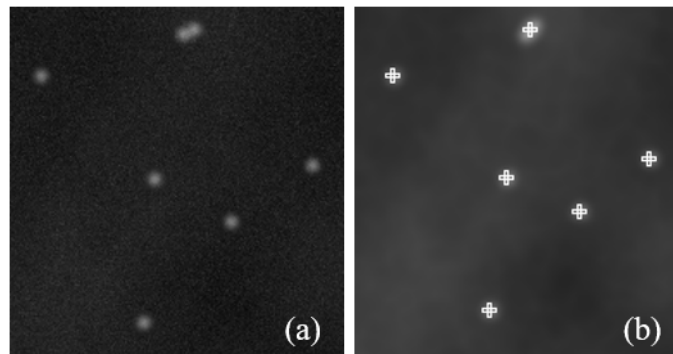FP is the number of false positives. As for the dataset of 2500 images with a constant SNR for Poisson noise of 10 and a varying weight of long-wavelength noise, from 0.1 to 0.5, the mean sensitivity is of 0.911±0.050 and the mean precision is of 0.986±0.013.

5.2 Experiments in real microrheology videos

5.2.1 Dataset description

The microrheology videos used for the acquisition of results in the context of this type of study have three distinct types: four videos used in the study of blood analogues (Campo-Deaño et al. (2013)), which can be represented by the example frame in Figure 5.6 (a), a real blood video, represented in Figure 5.6 (b) and seven other blood analogue videos acquired through a different camera, of which Figure 5.6 (c) is an example. Even though there are two types of blood analogues in study, the appearance of their videos is similar. These amount to the total of twelve videos with thousands of frames (5000 to 7000), each. For simplicity, videos that are represented by Figure 5.6 (a) will be referred as *type A* videos, and the remaining two as *type B* and *type C* videos, respectively.

Regarding the properties of each video type, type A videos are image acquisitions of four non-Newtonian solutions, respectively composed by either polyacrylamide (PAA), hyaluronic acid (HA) and dimethylsulfoxide (DMSO), or xanthan gum (XG) and DMSO, or PAA, HA and sucrose, or XG and sucrose. These videos were acquired at a frame rate of 100 frames per second, resolution of 0.17 $\mu m/pixel$ and a temperature of 20°C. Their background displays overall homogeneity, showing only some shading artifacts around the particles. They contain some out-of-focus particles, which are brighter but not surrounded by a dark halo, contrarily to the focused particles.

Type B videos, which capture whole blood, are characterized by a noisy, inhomogeneous, dark background, with intensities very similar to those of the particles one wants to detect, hindering the location task. These are taken at a frame rate of 90 frames per second, resolution of 0.17 $\mu m/pixel$ and a temperature of 27°C. The appearance of the particles is highly varying, since they can appear as completely dark or bright with a dark halo. It is difficult to distinguish out-of-focus particles in these images.

Type C videos capture samples of aqueous solutions of PAA. They have a greater quantity of particles than the previous two, together with many out-of focus particles, which are not easy to distinguish, shading artifacts and non-circular objects. The particles are bright circles with dark halos. These videos are taken at a frame rate of 125 frames per second, resolution of 0.2 $\mu m/pixel$ and a temperature of 22°C. What varies between the seven videos is the concentration of the PAA solution (50 ppm, 100 ppm and 200 ppm), and insertion or not of the solutions in an ultrasonic bath, with the objective of separating the particles and avoiding agglomerates, which did not affect the samples' properties.

The tracer type and radius is common to every video type: monodisperse 2.8 μm diameter beads (Dynabeads ®M-270 Carboxylic Acid). Moreover, all video types display many particle agglomerates.
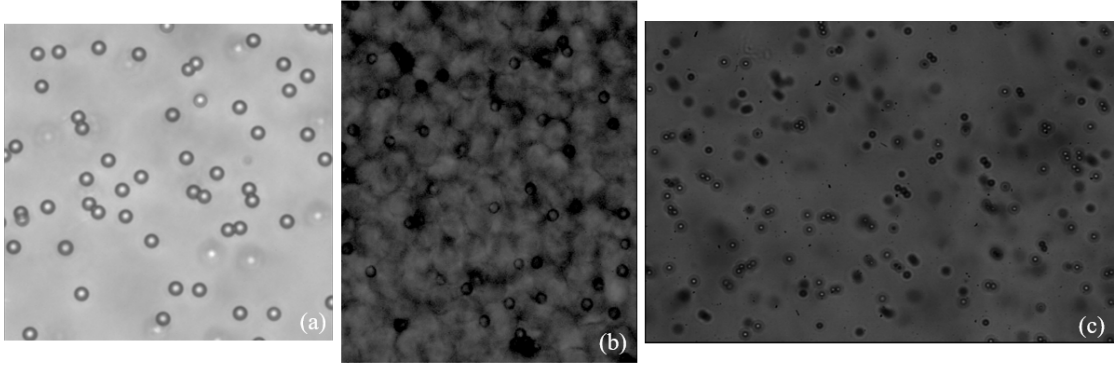

Figure 5.6: Example images of the dataset of real microrheology videos used in this work. (a) is an example of a video of 1.4 μm tracers embedded in a blood analogue fluid (polyacrilamide solution described in Campo-Deaño et al. (2013)), (b) is a frame of a real blood video for microrheology, and (c) is a blood analogue video, acquired through a different camera setup than (a).

For the type A videos, the complex modulus results could be compared with the published values in Campo-Deaño et al. (2013), which used the same videos to study the behavior of blood analogues with microrheology techniques. Also, the MSDs of the tracks used to acquire the said complex moduli were provided, and could also be compared to the acquired ones. For videos of the type C, the results of microrheology could be compared with those of macrorheology, so as to correlate the tendency of the viscoelastic moduli curves. For all the video types, an analysis of the number of particles that could be correctly detected was done, having as reference the manual annotation of a set of frames per video.

5.2.2   Result acquisition and comparison to references

A technique for one-point video particle tracking microrheology result acquisition was implemented, allowing to convert the mean squared displacements of the particles in the videos into viscoelastic moduli curves, so as to analyze the viscous and elastic behavior of each sample.

After manually discarding some tracks which show irregularities (which may be due to image artifacts or to detection inaccuracies), the ensemble mean squared displacement for the remaining particles, whose tracks can be formed throughout all the frames in each video, without adding "virtual" particles to cover for occasional disappearances, was calculated. The maximum lag time allowed for this calculation is the one corresponding to 300 frames. For example, if the frame rate of a certain video is of 100 frames per second, 3 seconds of video is the maximum lag time out to which the MSD is computed, and 2.09 rad/s is the minimum angular frequency to which the complex moduli can be calculated. The maximum angular frequency that can be used to compute the complex moduli depends on the frame rate, and, in this specific case, could go up to 628.319

rad/s. In practice, the results are usually clipped at lower frequencies, when the noise effects become notorious.

The function which correlates the particles' MSD to the complex modulus of the fluid is adapted both from Leocmach (2015) and Crocker and Hoffman (2007), combining the approaches of the original implementation, in IDL with *Pythonic* operations. The theoretical foundations of this method can be found in Mason (2000). This algorithm computes the outputs of the Generalized Stokes-Einstein equation (GSER), presented in Chapter 2, through an algebraic approach. For that, it creates a power-law approximation of the MSD data, and then finds the first and second logarithmic derivatives of this expanded, smoother version of the data. This is done because data for MSD is known at discrete times, over a limited time range, which induces errors in the moduli when one proceeds to computing Fourier or Laplace transforms, in the frequency domain. These first and second logarithmic derivatives are, then, input into the Mason (2000) method for numerical calculation of the Laplace transform and computation of the complex modulus through GSER. A problem that is common to numerical Laplace transforms is that, even though the data is extended through the power-law approximation, the extrema of the MSD are used to extrapolate to zero and to infinity, leading to a high influence of the curvature near the extrema on erroneous results. This curvature may be due to vibration of diffusion of the particles to out of the two-dimensional imaging plane, reason why several data points from the edges of the MSD should not be used in the conversion. It is recommended, in the studies of Crocker and Hoffman (2007) that the user determines how many points from the extrema are maintained or deleted, on a case by case basis, by iteratively transforming MSD curves into complex modulus results and observing the rheological curves fluctuating up and down, as points are added or removed. Nevertheless, it is set that G'(ω) and G"(ω) are clipped at $0.03 \times G(\omega)$, as they are most certainly meaningless below that point (Leocmach (2015)).

For videos of the type A, the acquired MSD curves and G'(ω) and G"(ω) curves are compared with the ones acquired and published in Campo-Deaño et al. (2013). An example of the overlapping curves is presented in Figure 5.7. The percentage relative deviation for the four videos of the type A is of 28.33±6.64% for the storage modulus, $G'(\omega)$,and of 4.97±2.21% for the loss modulus, $G''(\omega)$. As for the MSD, the percentage relative deviation between the curves for the four videos is of 10.53±5.04%.

One must note that the method used for particle detection, which produced the reference results, is a version of the Centroid Technique, which is also used in this study. However, it is not known which particles were used to create the tracks on the reference results, or what tracks were kept in the calculation of the average MSD. Moreover, the method for transforming the MSD calculations into complex moduli is similar to the one implemented in this work, but the intermediate steps of both implementations use functions that are analogous, but not equivalent. An example is the fitting function used to fit the MSD data to a power-law: the IDL outuputs are inconsistent with the *Python* ones, but the source code of the IDL function is not of open-access.

A type A video was analyzed in order to corroborate the effect of using the Gaussian Fitting method, the Radial Symmetry method or the Centroid Technique to detect the centroids accurately.
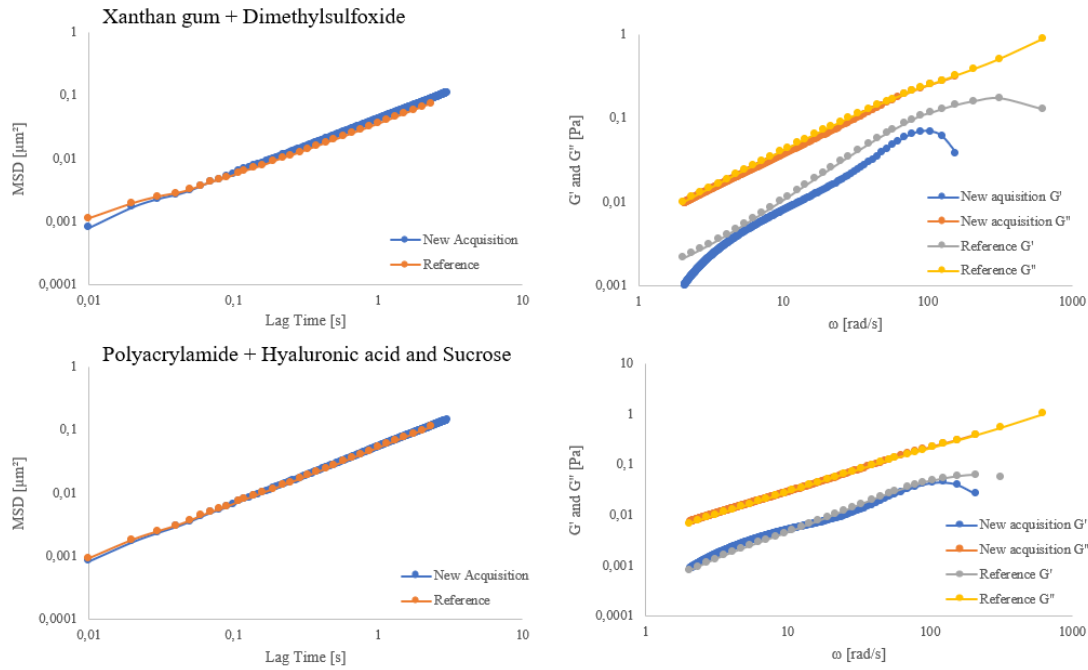
Figure 5.7: Comparison between reference results for the complex modulus and MSD curves and acquisitions through the proposed methodologies, for the same videos, of the same fluids. These are taken for videos of the type A. For the first row of results, the relative deviation for the storage modulus (G') is of 34.30±10.95%, of 8.29±4.66% for the loss modulus (G"), and of 12.00±6.02% for the MSD. For the second row of results, the relative deviation for G' is of 17.51±12.11%, of 2.47±1.38% for G", and of 3.98±4.03% for the MSD. The microrheology videos were kindly provided by Rui Mendes, Mechanical Engineering student in FEUP.

Even though no ground truth is available for this data, it can be seen that the error introduced in the detection by the Gaussian Fitting and Radial Symmetry methods leads to an overestimation of the particles' movement, and, therefore, of their MSD (Figure 5.8), which would affect the final results of microrheology. If combined with the results of section 5.1.2, visually detailed in Figures 5.3 and 5.4, the disparity between the MSD values for the tested methods corroborates that the Centroid Technique is the most accurate method of the three, for particle detection.

Two videos of the type C were analyzed with the objective of comparing the complex modulus obtained through macrorheology and the microrheology techniques detailed in this work. It is worthy to point out that the viscoelastic moduli obtained by the rheometer does not provide reliable data for G' due to the low elasticity of the sample, which is out of the sensitivity of the device. Moreover, the oscillatory experiments conducted through commercial rheometers have the limitation of inertia of the rotating tool, which can dominate the shear response of the sample at high frequencies. These experiments also have the problem of slip, since the sample can loose mechanical contact with the rotating surface (Allan (2014)).

The complex moduli acquired through micro and macrorheology for a PAA aqueous solution with a concentration of 100 ppm are plotted in Figure 5.9. Despite the deviation between the
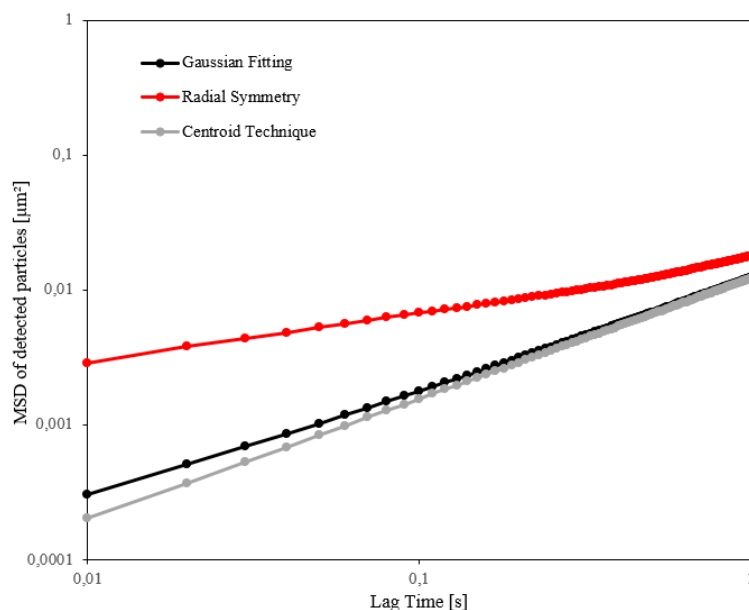
Figure 5.8: Mean squared displacement in function of lag time for a blood analogue type A video, in which the particle centroids are detected with the Radial Symmetry method, through Gaussian fitting and through the Centroid Technique.

curves for micro and macrorheology results, mainly for the elastic modulus, which are substantial at high frequencies, the initial tendency of the microrheology curves shows agreement with that of the microrheology curves. Moreover, G'' obtained through macrorheology is comparable to the present data, showing excellent agreement. Therefore, as G'' is matching the results of macrorheology data, one can trust that data for G' was successfully obtained, in a reliable way, by microrheology.

The results for both the elastic and the viscous component that are plotted in Figure 5.9 have contributions from a sample that is placed inside an ultrasonic bath, so that the particles do not form agglomerates, whose movement statistics cannot be considered in the microrheology calculations. If can be seen that this technique has positive outcomes, since the loss and storage modulus curves obtained from videos of solutions that were subjected to the ultrasonic bath are closer to the macrorheology results.

Testing the number of particles that are detected for every video type, five equally-spaced frames of each video were selected for this analysis to be done. For videos of the type A, the average sensitivity, or recall, is of 0.928 ± 0.022 and the precision is of 0.936 ± 0.024. For videos of type B, in which the particle appearance varies substantially in each frame, the sensitivity drops to 0.580 ± 0.040 due to the increasing number of false negative detections, particles that are missed by the detection algorithm. The precision is, however, of 0.821 ± 0.054. Testing the images of type C, the sensitivity is of 0.938 ± 0.020, but the precision drops to 0.508 ± 0.027, as the false discovery rate rises to 0.492 ± 0.027. This is mainly due to the presence of many circular structures, corresponding to shadows and particles that are out-of-focus, that are fairly similar to
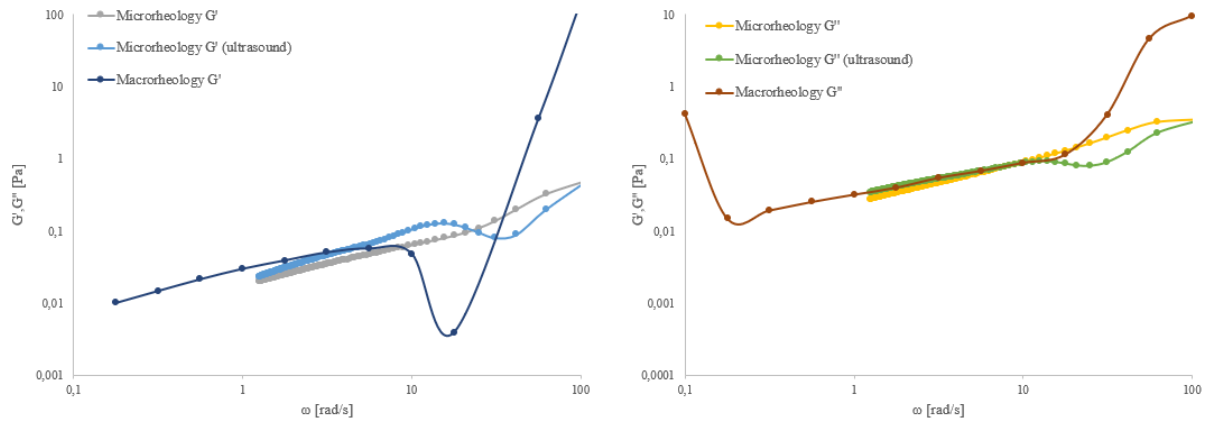
Figure 5.9: Results of macrorheology and microrheology tests for the same PAA aqueous solution. The results with the "ultrasound" tag are those produced through a microrheology setup in which the samples were placed in an ultrasonic bath, with the objective of separating the particles and avoiding agglomerates.

the particles that should be detected. Unlike the deterioration in sensitivity that is seen for type B images, a decrease in precision is not problematic, since the user interface that is developed in the context of this work is prepared to allow the user to delete false positives manually. Also, a decrease in sensitivity does not prevent the composition of adequate MSD curves, if it is not critical. However, the statistical relevance of the results acquired through a small set of trajectories is obviously lower than that for a large set of tracks.

Chapter 6

Guided User Interface

When a solid combination of techniques with validated results is put together, the implementation of a framework that can be used by researchers in the area is highly desirable. This framework needs to be thought as an intuitive interface, developed taking into consideration an iterative process of needs screening, through which researchers that conduct microrheology studies were inquired on which functionalities should be implemented to create an easy, effective and pleasing user experience. Some of the collected requisites for the framework were: it should be able to track as many particles as possible; the user should be aware of what particle choices, frame modifications or track formations are being done; the user should be able to delete trajectories that he or she does not want to include in the final calculations; the user should be able to check what changes are made in the final results if he or she performs any action that influences them.

The code for the particle tracking microrheology methods was written in Python3 and the interface was created with the module PyQt5. PyQt5 was used to build the Guided User Interface (GUI) because it inherits many features from the same libraries used for algorithm development, such as visualization capabilities from the plotting library matplotlib. Moreover, the Qt Designer tool for designing and building GUIs with Qt widgets could be used to compose the interface windows, in a what-you-see-is-what-you-get manner.

The interface contains two windows: one for the detection phase and another for the linking phase and for further acquisition of microrheology data. The window suited for detection (Figure 6.1) allows the user to choose a file, opening a dialog to access the computer storage (Figure 6.2), for file selection. The user can either choose a video, an image sequence or a *.pckl* file that contains previously done detections. For the user to choose an image sequence, which should contain every frame from a video, the images must be named sequentially, with numbers going from 0 to the last frame number. That way, the user can select the first frame, and the remaining ones are opened following their numeric order. If the user chooses a file that contains detections created by previous uses of the interface, he or she is invited to proceed directly to the linking window, avoiding the need to re-detect all the particles, in every frame.

If the users choose to open a video or an image sequence, they can travel through the frames of the selected sequence using a slider, that goes through every frame sequentially. Then, one
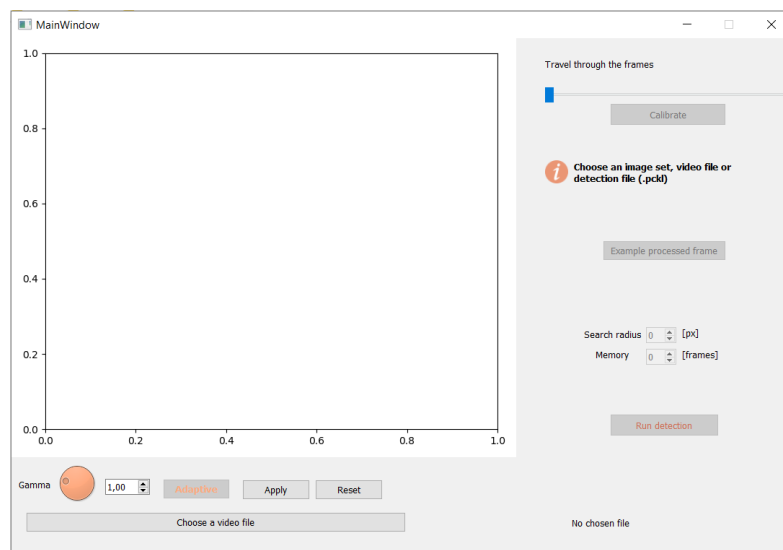
Figure 6.1: Illustration of the particle detection window, in its initial state.

can proceed to pre-processing the frames by selecting a gamma coefficient, either through the available dial or spin box (Figure 6.3). These differ in the resolution they offer: spinning the dial, one can quickly visualize the effects of different gamma correction types (with a resolution of 0.1), since the processed image is continuously updated. By setting a coefficient in the spin box, one can achieve a resolution of 0.01, and slowly modify this parameter. The interface also offers the option of adaptive gamma correction, and, when the correspondent button is pressed, the modified adaptive gamma correction algorithm analyzes the image and outputs a gamma coefficient, that is set on the spin box for the user to see and modify. The options for setting a gamma coefficient are synchronized, which means that, when the dial is used to set the value, the spin box will display the updated coefficient, and vice versa. Through the buttons "Apply" and "Reset", the user can either apply the gamma correction that is set through the chosen coefficient, or reset it back to a coefficient of 1, which does not impose any modifications on the image.

After pre-processing is done, the user needs to move on to the calibration routine, by clicking the "Calibrate" button. This will trigger the process that creates parameters that are necessary for particle detection. The user is informed whether calibration was successful or not, since an image with some of the particles surrounded by a bounding box is presented shortly after the button press (Figure 6.4). If the calibration algorithm is not able to detect any particles, or the detected features have a diameter of less than three pixels, the user is invited to try different gamma correction settings.

To test whether the detection algorithm will produce correct results or not, the user may press the "Example processed frame" button, which will run the detection methodology for one of the frames of the sequence and display the result in the figure on the left, showing small white crosses over the detected particles (Figure 6.5). If the user is happy with the detection results that are shown, he or she can run the detection algorithm for the remaining frames by clicking "Run detection". First, however, he or she should set the search radius, maximum distance the particles can
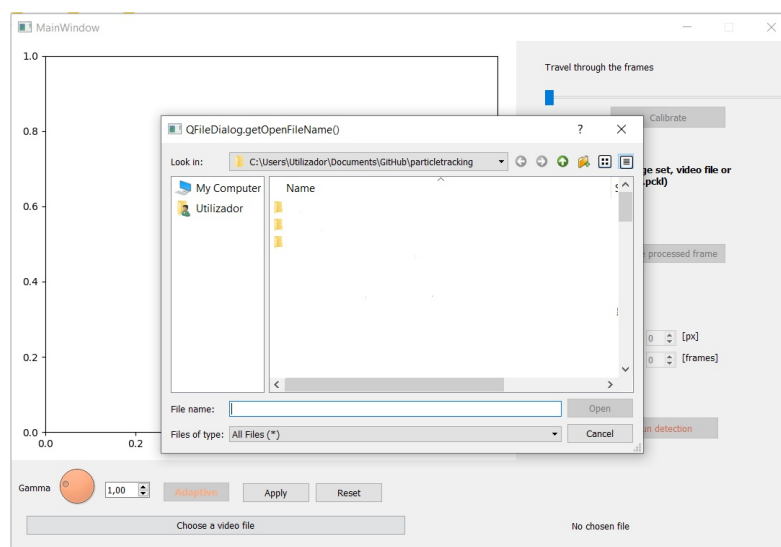
Figure 6.2: Illustration of the dialog for file opening.

move between frames, in pixels, and the memory parameter, the maximum number of frames during which a feature can vanish, then reappear nearby, and be considered the same particle. These parameters will be used in the linking phase. At this point, a *.pckl* file is stored in the video or image sequence folder, with all the detections made in all the frames.

After the particle detection is done in all the frames of a sequence, the window suited for the linking phase opens, automatically, displaying another view of the images (Figure 6.6). Now, the images that are displayed, and which can be sequentially shown by moving the horizontal slider, have detection markers overlapped on the detected particles, as a way for the user to tell whether detection was done correctly or not. The user must input, in the spin boxes under the image view, some parameters for the MSD calculation and for the conversion of the MSD results into complex moduli. After checking the correctness of the detection results, the user may proceed to linking the detections into trajectories by clicking the "Simple linking" button. Selecting, in the spin box below, a minimum number of points that need to be linked, per track, for that track to be valid, will force the linking routine to run again and re-select the tracks to be formed. After linking, the image that is shown has the overlapped tracks drawn over it, and it is possible to see if the particles have drifting motion, other than the characteristic Brownian one. If the user notes that the particles have drifting motion, he or she can compute this drift and remove it, by pressing, respectively, the "Compute drift" and "Correct drift" buttons. After drift is corrected, the adjusted trajectories are drawn over the image, replacing the ones that shown drift.

Two plots are shown in the linking window when linking is done: one for displaying each particle's track (x and y coordinates) and one for the MSD of both the particle whose track is being displayed (MSD versus lag time plot), and the average movement of all the particles that are being considered for the calculations (Figure 6.6). The user can choose not to consider some of the tracks for the global MSD computation, by pressing the button "Discard" by the track plot (Figure 6.6). Contrarily, if a certain track was already discarded from the global MSD calculation,
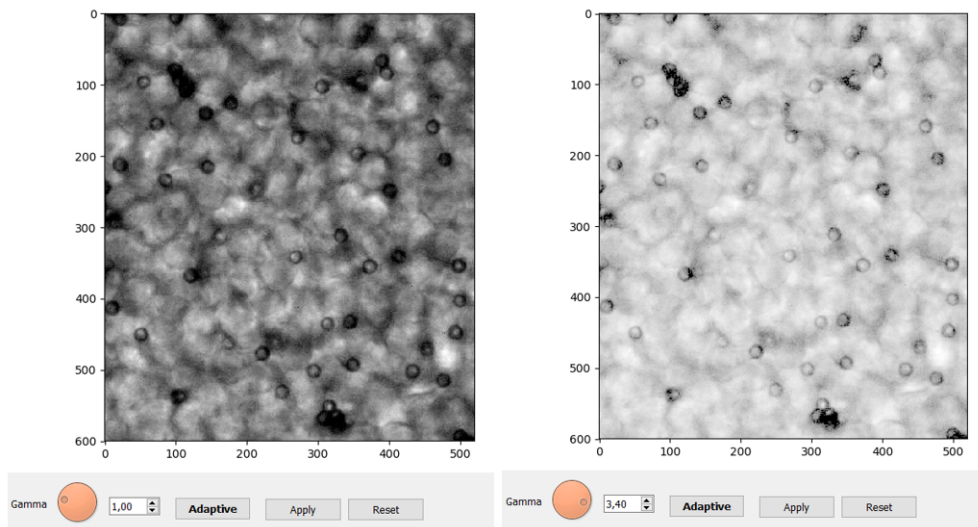
Figure 6.3: Illustration of the gamma correction in the visual interface.

the button will display the word "Keep", and, if pressed, the track will be re-added to the set. Observing all the tracks and all the contributions of each particle to the global MSD is possible by pressing the blue arrow, on the right side of the plots, which iterates through the particle tracks. A blue circle is drawn around each particle whose track is being displayed, so that the user knows if the detection is valid or not, or even if the particle is positioned in an aggregate. Having arrived to the intended set of tracks, the user can now calculate the complex modulus of the fluid, by pressing "Get G' and Get G''", under the image view (Figure 6.7). Pressing this button will create a *.xls* file with the MSD of the particles whose trajectories are kept and the complex modulus values that are calculated. The image view will, then, be replaced by the plot of the storage and loss moduli over angular frequency. If the user is not happy with the results, he or she can press the same button, which will now display the words "Show tracks" to re-select the tracks that the user wants to keep for global MSD calculation.
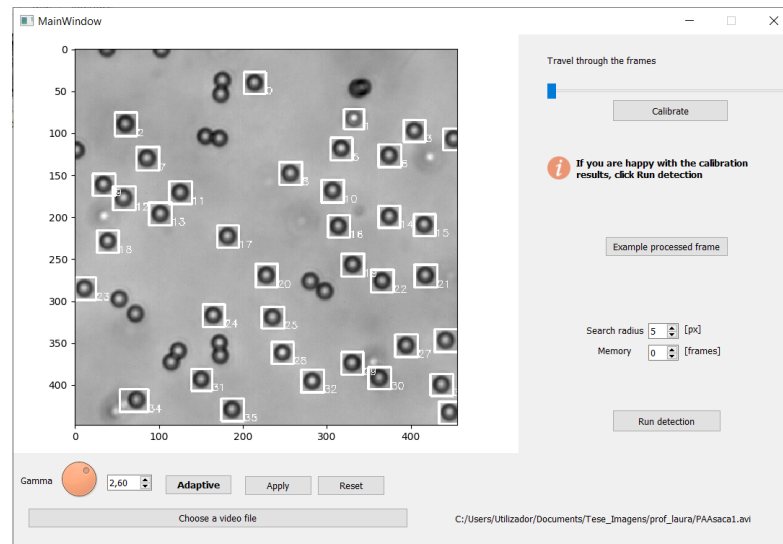
Figure 6.4: Illustration of the calibration outputs displayed in the visual interface.
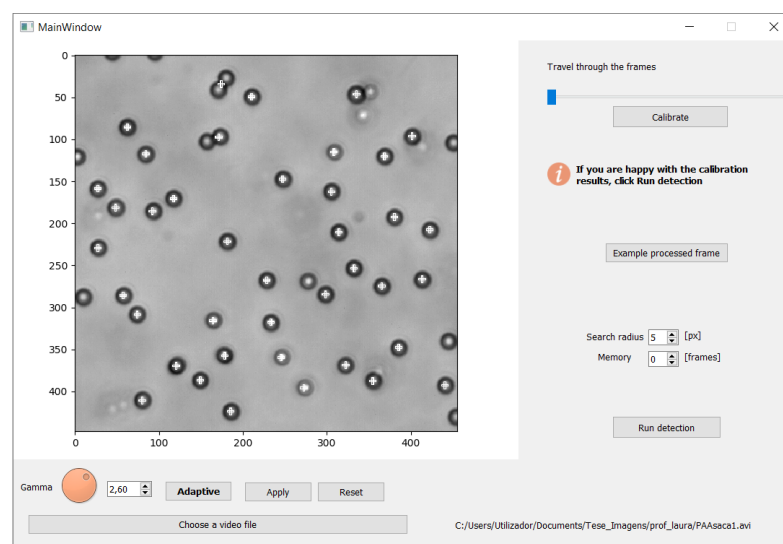

Figure 6.5: Illustration of the detection example in one of the video frames.
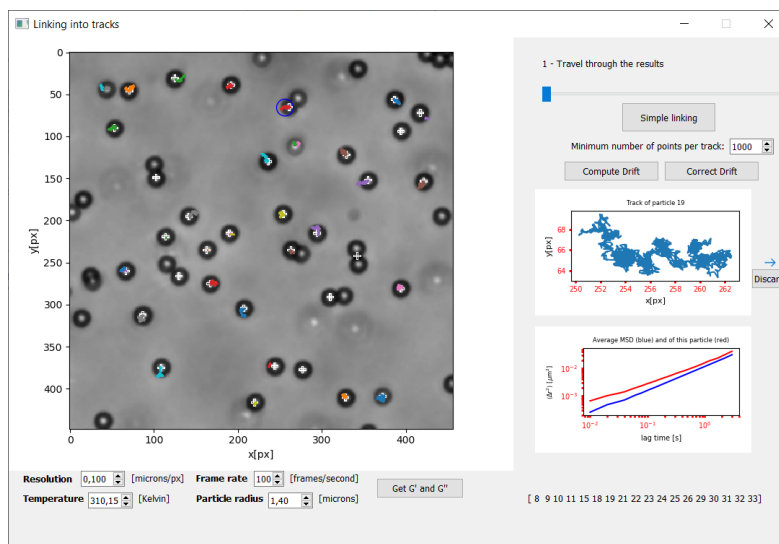
Figure 6.6: Illustration of the linking window, in the process of deleting a selected track.
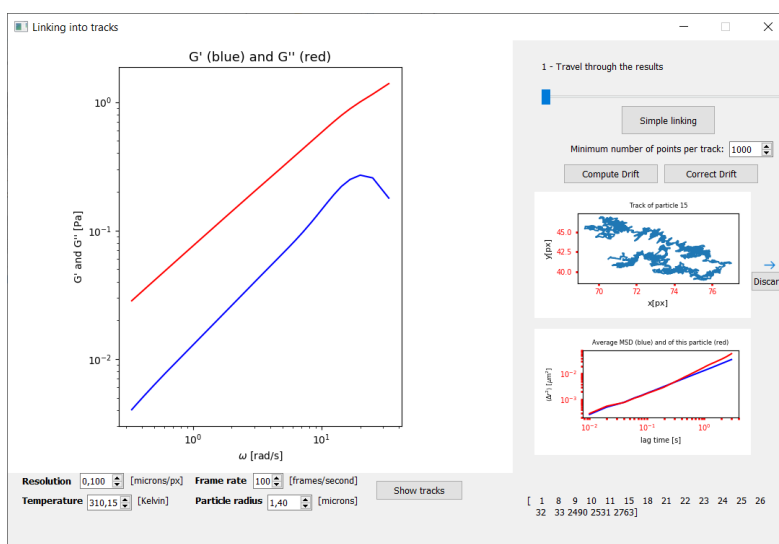

Figure 6.7: Illustration of the complex modulus plot that is shown in the user interface.

Chapter 7

Conclusion

The main goal of this dissertation was to create a framework for particle tracking in microrheology studies, exploring particle tracking techniques that would be robust enough to cover a variety of video types, being as automatic as possible. The developed methodologies allowed for a high level of automation in the particle tracking pipeline, requiring only the user input for the coefficient of a gamma correction. This non-automated step was implemented to be as intuitive as possible, and the developed user interface offers the necessary guidelines for it to be done easily.

Results obtained with a synthetic database showed that the explored methods could detect the particle centers with little offset, having a maximum mean total error of 0.53 pixels, for an image set case whose SNR for Poisson-noise is 10 and the weight of long-wavelength noise is 0.5. Tests with real microrheology videos showed agreement between the results for macrorheology and microrheology, and between published microrheology studies' results and results acquired through the proposed methodologies. However, by testing the number of particles that are detected in the microrheology videos and in the synthetic database, one can infer that the number of false positive detections is highly variant with image type. While precision and sensitivity are high (above 90%) for videos in which particle detection is trivial and no artifacts are present, precision drops to around 50% when there are many out-of-focus particles and circular shadow artifacts, and sensitivity drops to 58% when the background is highly inhomogeneous and the particles' appearance is variable. These results enhance the difficulty of generalizing a particle detection pipeline that is invariant to the image type, and show that there is room for improvement, either of pre-processing techniques, detection methodologies or false positive deletion methods. Nonetheless, a metric of resemblance to a particle representation that is not dataset-specific, the Radial Symmetry metric, was explored in the context of false positive deletion and provided good results.

While the results acquired through the available dataset seem promising, yet created through a pipeline that can be improved, the introduction of more microrheology setups in the database would largely benefit this work, since many cases in which these techniques can be applied are not contemplated in this dissertation. Namely microrheology applied to fluorescence microscopy, to study the rheology of subcellular structures, for example, would introduce the color variable in the equation, since the fluorophores that stain the specimens allow for the creation of color images.

Although the set of features that the GUI offers is enough to conduct a microrheology study, from particle detection to complex modulus curve plotting, there is room for the addition of useful functionalities, such as a tool for manually clipping the extrema of the MSD plots, removing noise from the complex modulus computation. Moreover, the process of false positive deletion could be made easier if the interface for deleting or keeping tracks could allow for the user to click the undesired tracks, instead of having to travel through all the tracks and observe them, one by one.

There is also room for improvement in what concerns the conversion of the MSDs of the trajectory sets into complex moduli, namely the introduction of the Two-Point Microrheology technique, in which the movement of correlated pairs of particles is analyzed, removing the influence of the interaction between the tracer and the matrix from the complex modulus calculations.

References

Matthew D. Wehrman, Seth Lindberg, and Kelly M. Schultz. Quantifying the dynamic transition of hydrogenated castor oil gels measured via multiple particle tracking microrheology. *Soft Matter*, 12(30):6463–6472, 2016. ISSN 1744-683X, 1744-6848. doi: 10.1039/C6SM00978F. URL http://xlink.rsc.org/?DOI=C6SM00978F.

Roseanna N. Zia. Active and Passive Microrheology: Theory and Simulation. page 37, 2017.

Tommy Garting and Anna Stradner. Optical Microrheology of Protein Solutions Using Tailored Nanoparticles. *Small*, 14(46):1801548, November 2018. ISSN 16136810. doi: 10.1002/smll. 201801548. URL http://doi.wiley.com/10.1002/smll.201801548.

John C. Crocker, M. T. Valentine, Eric R. Weeks, T. Gisler, P. D. Kaplan, A. G. Yodh, and D. A. Weitz. Two-Point Microrheology of Inhomogeneous Soft Materials. *Physical Review Letters*, 85(4):888–891, July 2000. ISSN 0031-9007, 1079-7114. doi: 10.1103/PhysRevLett.85.888. URL https://link.aps.org/doi/10.1103/PhysRevLett.85.888.

John C. Crocker and David G. Grier. Methods of Digital Video Microscopy for Colloidal Studies. *Journal of Colloid and Interface Science*, 179(1):298–310, April 1996. ISSN 00219797. doi: 10.1006/jcis.1996.0217. URL http://linkinghub.elsevier.com/retrieve/pii/S0021979796902179.

Raghuveer Parthasarathy. Rapid, accurate particle tracking by calculation of radial symmetry centers. *Nature Methods*, 9(7):724–726, July 2012. ISSN 1548-7091, 1548-7105. doi: 10. 1038/nmeth.2071. URL http://www.nature.com/articles/nmeth.2071.

Leslie Howard Sperling. Polymer Viscoelasticity and Rheology. In *Introduction to Physical Polymer Science*, pages 507–556. John Wiley & Sons, Inc., Hoboken, NJ, USA, November 2005. ISBN 978-0-471-75712-2 978-0-471-70606-9. doi: 10.1002/0471757128.ch10. URL http://doi.wiley.com/10.1002/0471757128.ch10.

Thomas G. Mezger. *Applied rheology: with Joe flow on rheology road.* Anton Paar, 2015.

Gebhard Schramm. A Practical Approach to Rheology and Rheometry. page 291, 2009.

Denis Wirtz. Particle-Tracking Microrheology of Living Cells: Principles and Applications. *Annual Review of Biophysics*, 38(1):301–326, June 2009. ISSN 1936-122X, 1936-1238. doi: 10.1146/annurev.biophys.050708.133724. URL http://www.annualreviews.org/doi/10.1146/annurev.biophys.050708.133724.

Pietro Cicuta and Athene M. Donald. Microrheology: a review of the method and applications. *Soft Matter*, 3(12):1449, 2007. ISSN 1744-683X, 1744-6848. doi: 10.1039/b706004c. URL http://xlink.rsc.org/?DOI=b706004c.

Laura Campo-Deaño. Fluid-flow characterization in microfluidics. In *Complex Fluid-Flows in Microfluidics*, pages 53–71. Springer, 2018.

Thomas G. Mason, Kavita Ganesan, J. Harry van Zanten, Denis Wirtz, and Scott C. Kuo. Particle Tracking Microrheology of Complex Fluids. *Physical Review Letters*, 79(17):3282–3285, October 1997. ISSN 0031-9007, 1079-7114. doi: 10.1103/PhysRevLett.79.3282. URL https://link.aps.org/doi/10.1103/PhysRevLett.79.3282.

S.S. Rogers, C. Van Der Walle, and T.A. Waigh. Microrheology of bacterial biofilms in vitro: Staphylococcus aureus and pseudomonas aeruginosa. *Langmuir*, 24(23):13549–13555, 2008.

Tianhui Maria Ma, J. Scott VanEpps, and Michael J. Solomon. Structure, mechanics, and instability of fibrin clot infected with staphylococcus epidermidis. *Biophysical journal*, 113(9):2100–2109, 2017.

Laura Campo-Deaño. Assessing the Dynamic Performance of Microbots in Complex Fluid Flows. *Applied Sciences*, 6(12):410, December 2016. ISSN 2076-3417. doi: 10.3390/app6120410. URL http://www.mdpi.com/2076-3417/6/12/410.

John C. Crocker and Brenton D. Hoffman. Multiple-particle tracking and two-point microrheology in cells. *Methods in cell biology*, 83:141–178, 2007.

Daniel TN Chen. Microrheology of soft matter. 2010.

Patrícia C. Sousa, Rafael Vaz, António Cerejo, Mónica S. N. Oliveira, Manuel A. Alves, and Fernando T. Pinho. Rheological behavior of human blood in uniaxial extensional flow. *Journal of Rheology*, 62(2):447–456, March 2018. ISSN 0148-6055, 1520-8516. doi: 10.1122/1.4998704. URL http://sor.scitation.org/doi/10.1122/1.4998704.

Laura Campo-Deaño, Roel P. A. Dullens, Dirk G. A. L. Aarts, Fernando T. Pinho, and Mónica S. N. Oliveira. Viscoelasticity of blood and viscoelastic blood analogues for use in polydymethylsiloxane *in vitro* models of the circulatory system. *Biomicrofluidics*, 7(3):034102, May 2013. ISSN 1932-1058. doi: 10.1063/1.4804649. URL http://aip.scitation.org/doi/10.1063/1.4804649.

SP Sutera and MH Mehrjardi. Deformation and fragmentation of human red blood cells in turbulent shear flow. *Biophysical journal*, 15(1):1–10, 1975.

CR Huang, WD Pan, HQ Chen, and AL Copley. Thixotropic properties of whole blood from healthy human subjects. *Biorheology*, 24(6):795–801, 1987.

Laura Campo-Deaño, Mónica S.N. Oliveira, and Fernando T. Pinho. A review of computational hemodynamics in middle cerebral aneurysms and rheological models for blood flow. *Applied Mechanics Reviews*, 67(3):030801, 2015.

Patrícia C. Sousa, J. Carneiro, Rafael Vaz, António Cerejo, Fernando T. Pinho, Manuel A. Alves, and Mónica S.N. Oliveira. Shear viscosity and nonlinear behavior of whole blood under large amplitude oscillatory shear. *Biorheology*, 50(5-6):269–282, 2013.

Andreja Zupančič Valant, Lovro Žiberna, Yannis Papaharilaou, Andreas Anayiotos, and Georgios C. Georgiou. The influence of temperature on rheological properties of blood mixtures with different volume expanders—implications in numerical arterial hemodynamics

simulations. *Rheologica Acta*, 50(4):389–402, April 2011. ISSN 0035-4511, 1435-1528. doi: 10.1007/s00397-010-0518-x. URL http://link.springer.com/10.1007/s00397-010-0518-x.

Ivo F. Sbalzarini and Petros Koumoutsakos. Feature point tracking and trajectory analysis for video imaging in cell biology. *Journal of Structural Biology*, 151(2):182–195, August 2005. ISSN 10478477. doi: 10.1016/j.jsb.2005.06.002. URL http://linkinghub.elsevier.com/retrieve/pii/S1047847705001267.

Nicolas Chenouard, Ihor Smal, Fabrice de Chaumont, Martin Maška, Ivo F. Sbalzarini, Yuanhao Gong, Janick Cardinale, Craig Carthel, Stefano Coraluppi, Mark Winter, Andrew R. Cohen, William J. Godinez, Karl Rohr, Yannis Kalaidzidis, Liang Liang, James Duncan, Hongying Shen, Yingke Xu, Klas E. G. Magnusson, Joakim Jaldén, Helen M. Blau, Perrine Paul-Gilloteaux, Philippe Roudot, Charles Kervrann, François Waharte, Jean-Yves Tinevez, Spencer L. Shorte, Joost Willemse, Katherine Celler, Gilles P. van Wezel, Han-Wei Dan, Yuh-Show Tsai, Carlos Ortiz de Solórzano, Jean-Christophe Olivo-Marin, and Erik Meijering. Objective comparison of particle tracking methods. *Nature Methods*, 11(3):281–289, March 2014. ISSN 1548-7091, 1548-7105. doi: 10.1038/nmeth.2808. URL http://www.nature.com/articles/nmeth.2808.

William J. Godinez, Marko Lampe, R. Eils, B. Muller, and K. Rohr. Tracking multiple particles in fluorescence microscopy images via probabilistic data association. In *2011 IEEE International Symposium on Biomedical Imaging: From Nano to Macro*, pages 1925–1928, Chicago, IL, USA, March 2011. IEEE. ISBN 978-1-4244-4127-3. doi: 10.1109/ISBI.2011.5872786. URL http://ieeexplore.ieee.org/document/5872786/.

Nicolas Chenouard. *Advances in probabilistic particle tracking for biological imaging*. PhD thesis, Institut Pasteur Paris, TELECOM ParisTech, January 2010.

Ishwar K. Sethi and Ramesh Jain. Finding Trajectores of Feature Points in a Monocular. *IEEE TRANSACTIONS ON PATTERN ANALYSIS AND MACHINE INTELLIGENCE*, (1):18, 1987.

William J. Godinez, Marko Lampe, Stefan Wörz, Barbara Müller, Roland Eils, and Karl Rohr. Deterministic and probabilistic approaches for tracking virus particles in time-lapse fluorescence microscopy image sequences. *Medical Image Analysis*, 13(2):325–342, April 2009. ISSN 13618415. doi: 10.1016/j.media.2008.12.004. URL https://linkinghub.elsevier.com/retrieve/pii/S1361841508001412.

M. Sanjeev Arulampalam, Simon Maskell, Neil Gordon, and Tim Clapp. A Tutorial on Particle Filters for Online Nonlinear/Non-Gaussian Bayesian Tracking. *IEEE TRANSACTIONS ON SIGNAL PROCESSING*, 50(2):15, 2002.

Alex Small and Shane Stahlheber. Fluorophore localization algorithms for super-resolution microscopy. *Nature Methods*, 11(3):267–279, March 2014. ISSN 1548-7091, 1548-7105. doi: 10.1038/nmeth.2844. URL http://www.nature.com/articles/nmeth.2844.

Florence Hediger Susan M. Gasser Daniel Sage, Franck R. Neumann and Michael Unser. Automatic tracking of individual fluorescence particles: application to the study of chromosome dynamics. *IEEE Transactions on Image Processing*, 14(9):1372–1383, September 2005. ISSN 1057-7149. doi: 10.1109/TIP.2005.852787. URL http://ieeexplore.ieee.org/document/1495509/.

D. Thomann and D.R. Rines. Automatic fluorescent tag detection in 3d with super-resolution: application to the analysis of chromosome movement. *Journal of Microscopy*, Vol. 208, Pt 1, October 2002.

Jean-Christophe Olivo-Marin. Extraction of spots in biological images using multiscale products. *Pattern Recognition*, 35(9):1989–1996, September 2002. ISSN 00313203. doi: 10.1016/ S0031-3203(01)00127-3. URL http://linkinghub.elsevier.com/retrieve/pii/ S0031320301001273.

Ihor Smal, Marco Loog, Wiro Niessen, and Erik Meijering. Quantitative comparison of spot detection methods in live-cell fluorescence microscopy imaging. In *2009 IEEE International Symposium on Biomedical Imaging: From Nano to Macro*, pages 1178–1181, Boston, MA, USA, June 2009. IEEE. ISBN 978-1-4244-3931-7. doi: 10.1109/ISBI.2009.5193268. URL http://ieeexplore.ieee.org/document/5193268/.

David S. Bright and Eric B. Steel. Two-dimensional top hat filter for extracting spots and spheres from digital images. *Journal of Microscopy*, 146(2):191–200, May 1987. ISSN 00222720. doi: 10.1111/j.1365-2818.1987.tb01340.x. URL http://doi.wiley.com/10.1111/j. 1365-2818.1987.tb01340.x.

Shan Jiang, Xiaobo Zhou, Tom Kirchhausen, and Stephen T. C. Wong. Detection of molecular particles in live cells via machine learning. *Cytometry Part A*, 71A(8):563–575, August 2007. ISSN 15524922, 15524930. doi: 10.1002/cyto.a.20404. URL http://doi.wiley.com/ 10.1002/cyto.a.20404.

Paul Viola and Michael Jones. Rapid object detection using a boosted cascade of simple features. In *Proceedings of the 2001 IEEE Computer Society Conference on Computer Vision and Pattern Recognition. CVPR 2001*, volume 1, pages I–511–I–518, Kauai, HI, USA, 2001. IEEE Comput. Soc. ISBN 978-0-7695-1272-3. doi: 10.1109/CVPR.2001.990517. URL http://ieeexplore.ieee.org/document/990517/.

Kang Li, Eric D. Miller, Leland E. Weiss, Phil G. Campbell, and Takeo Kanade. Online Tracking of Migrating and Proliferating Cells Imaged with Phase-Contrast Microscopy. In *2006 Conference on Computer Vision and Pattern Recognition Workshop (CVPRW'06)*, pages 65–65, New York, NY, USA, 2006. IEEE. ISBN 978-0-7695-2646-1. doi: 10.1109/CVPRW.2006.150. URL http://ieeexplore.ieee.org/document/1640506/.

Daniel Brinton Allan. *Interfacial Microrheology of Biological Films*. PhD thesis, Johns Hopkins University, 2014.

Daniel B. Allan, Thomas Caswell, Nathan C. Keim, and Casper M. van der Wel. trackpy: Trackpy v0.4.1, April 2018. URL https://doi.org/10.5281/zenodo.1226458.

Benjamin S. Schuster, Laura M. Ensign, Daniel B. Allan, Jung Soo Suk, and Justin Hanes. Particle tracking in drug and gene delivery research: State-of-the-art applications and methods. *Advanced Drug Delivery Reviews*, 91:70–91, August 2015. ISSN 0169409X. doi: 10.1016/j.addr.2015.03.017. URL https://linkinghub.elsevier.com/retrieve/ pii/S0169409X15000563.

Erik Meijering, Oleh Dzyubachyk, and Ihor Smal. Methods for Cell and Particle Tracking. In *Methods in Enzymology*, volume 504, pages 183–200. Elsevier, 2012. ISBN 978-0-12-391857-4. doi: 10.1016/B978-0-12-391857-4.00009-4. URL https://linkinghub.elsevier. com/retrieve/pii/B9780123918574000094.

Vladimir Agafonkin. A dive into spatial search algorithms, April 2017. URL https://blog.mapbox.com/a-dive-into-spatial-search-algorithms-ebd0c5e39d2a.

Frank Pfenning, André Platzer, Rob Simmons, and Iliano Cervesato. Lecture 15 - binary search trees. URL https://www.cs.cmu.edu/~15122/handouts/15-bst.pdf.

Ashok Harnal. A working example of K-d tree formation and K-Nearest Neighbor algorithms, January 2015. URL https://ashokharnal.wordpress.com/2015/01/20/.

Aaron Lichtman. Teaching data structures in C++. Great resource for students.: alichtman/data-structures-cpp, December 2018. URL https://github.com/alichtman/data-structures-cpp. original-date: 2018-04-01T12:03:16Z.

Nate Foster. B-trees, 2012. URL https://www.cs.cornell.edu/courses/cs3110/2012sp/recitations/rec25-B-trees/rec25.html.

Rajinikanth. B - Trees - Data Structures, 2019. URL http://btechsmartclass.com/data_structures/b-trees.html.

Khuloud Jaqaman, Dinah Loerke, Marcel Mettlen, Hirotaka Kuwata, Sergio Grinstein, Sandra L. Schmid, and Gaudenz Danuser. Robust single-particle tracking in live-cell time-lapse sequences. *Nature Methods*, 5(8):695–702, August 2008. ISSN 1548-7091, 1548-7105. doi: 10.1038/nmeth.1237. URL http://www.nature.com/articles/nmeth.1237.

Curtis T. Rueden, Johannes Schindelin, Mark C. Hiner, Barry E. DeZonia, Alison E. Walter, Ellen T. Arena, and Kevin W. Eliceiri. Imagej2: Imagej for the next generation of scientific image data. *BMC bioinformatics*, 18(1):529, 2017.

Gary Bradski. The OpenCV Library. *Dr. Dobb's Journal of Software Tools*, 2000.

Adrian Rosebrock. OpenCV Gamma Correction, October 2015. URL https://www.pyimagesearch.com/2015/10/05/opencv-gamma-correction/.

Harvey Rhody. Lecture 10: Hough Circle Transform. page 22, 2005.

Mathieu Leocmach. The colloid toolkit, 2015. URL http://dx.doi.org/10.5281/zenodo.31286.

T.J. Denich, L.A. Beaudette, H Lee, and J.T. Trevors. Effect of selected environmental and physico-chemical factors on bacterial cytoplasmic membranes. *Journal of microbiological methods*, 52(2):149–182, 2003.

Erik Reinhard, Wolfgang Heidrich, Paul Debevec, Sumanta Pattanaik, Greg Ward, and Karol Myszkowski. *High dynamic range imaging: acquisition, display, and image-based lighting*. Morgan Kaufmann, 2010.

Banu Fathima Mariyam and Annes Philip. Adaptive quality enhancement for videos using agcwd. 2014.

John Immerkaer. Fast noise variance estimation. *Computer vision and image understanding*, 64 (2):300–302, 1996.

Jean Serra. *Image analysis and mathematical morphology*. Academic Press, Inc., 1983.

Rafael C. Gonzalez, Richard E. Woods, et al. Digital image processing [m]. *Publishing house of electronics industry*, 141(7), 2002.

Stanley R Sternberg. Biomedical image processing. *Computer*, (1):22–34, 1983.

Nobuyuki Otsu. A threshold selection method from gray-level histograms. *IEEE transactions on systems, man, and cybernetics*, 9(1):62–66, 1979.

Timothy J. Ross et al. *Fuzzy logic with engineering applications*, volume 2. Wiley Online Library, 2004.

Frank Klawonn and Frank Höppner. What is fuzzy about fuzzy clustering? understanding and improving the concept of the fuzzifier. In *International symposium on intelligent data analysis*, pages 254–264. Springer, 2003.

Bruce F. Naylor. A tutorial on binary space partitioning trees. In *Computer Games Developer Conference Proceedings*, pages 433–457, 1998.

Michael W. Davidson. Microscopy basics - resolution, 2019. URL https://www.microscopyu.com/microscopy-basics/resolution.

Geoffrey Y. Gardner. Visual simulation of clouds. In *ACM Siggraph Computer Graphics*, volume 19, pages 297–304. ACM, 1985.

Thomas G. Mason. Estimating the viscoelastic moduli of complex fluids using the generalized stokes–einstein equation. *Rheologica acta*, 39(4):371–378, 2000.